TECHNISCHE UNIVERSITÄT DRESDEN

Faculty of Mechanical Science and Engineering

Chair of Materials Science and Nanotechnology

Dissertation

Magnetosensitive composites and sensors in flexible and mechanically active platforms

Eduardo Sergio Oliveros Mata

to achieve the academic degree

Doktor-Ingenieur (Dr.-Ing.)

Supervisor

Prof. Dr. Gianaurelio Cuniberti

Chair

Prof. Dr. Stefan Odenbach

Reviewers

Prof. Dr. Gianaurelio Cuniberti

Prof. Dr. Martin Kaltenbrunner

Examiner

Prof. Dr. Christoph Leyens

Comitee member

Prof. Dr. Niels Modler

23rd May 2023

Acknowledgements

I am grateful for the continuous support of those around me, which made this thesis possible. This journey can be, at the same time, challenging and joyful, and can only be successfully accomplished through the continuous support of the people around me.

I am thankful to my supervisors that guided me and kept it challenging, allowing me to expand the impact of my work. Their expertise and encouragement challenged me to investigate deeper into my research, extending the impact of my work beyond my initial expectations. I am also thankful for the collaboration with my colleagues, who generously shared their expertise and time to tackle both simple and demanding tasks. In this matter, I would like to express special mention to all the members of the FWID department, your contributions have enriched my research and broadened my perspective in different areas.

I would also like to express my gratitude and appreciation to the individuals and groups that sustain the framework of our activities. I am indebted to society as a whole, as I believe that knowledge belongs to and is only made possible by all of us. I hope that this research contributes positively to our society, providing some hints to solve relevant challenges. I am grateful to the scientific, technical, administrative, and maintenance staff of the ERC, DFG, HZDR, and TU Dresden that keep running the essential infrastructure and budget for the accomplishment of our scientific activities.

To the fellow doctoral candidate researchers that share this path with me, thanks for keeping it enjoyable and rewarding. Through our discussions, I understood that *keeping it fun*, means believing in the relevance of our work for ourselves and others. I encourage us all to keep the spirit of exploration and continue making our research activities fun. I am especially thankful to the previous, current, and future DocReps that go beyond their research responsibilities and dedicate their efforts to the improvement of our doctoral experience and working conditions.

I dedicate this thesis to my family, I am truly fortunate to have a network of love and patience that I know I can rely on in even the most challenging moments. Gracias por apoyarme y creer en mí. Ustedes son mi motivación para seguir adelante. To my dear friends that stay by my side, offering words of encouragement despite my delayed responses to your messages, I am sincerely grateful. Finally, to Diana, that can easily take most of the roles mentioned before; thanks again for all and each of them. You are the most talented person to untangle the most intricate mental knots while always keeping sight of what truly matters. Thank you for being my partner in life, work, dance, and growth.

Statement of authorship

I hereby certify that I have authored this document entitled *Magnetosensitive composites and sensors in flexible and mechanically active platforms* independently and without undue assistance from third parties. No other than the resources and references indicated in this document have been used. I have marked both literal and accordingly adopted quotations as such. There were no additional persons involved in the intellectual preparation of the present document. I am aware that violations of this declaration may lead to subsequent withdrawal of the academic degree.

Dresden, 23rd May 2023

Eduardo Sergio Oliveros Mata

Abstract

This thesis presents novel solutions for the fabrication of functional magnetoresponsive systems, with a focus on the development of magnetic composites as sensors and actuators. Currently, there is a need for multifunctional mechanically flexible materials that can be easily processed into functional devices that respond to a wide range of physical stimuli, including magnetic fields. These characteristics aim for lightweight, and imperceptible systems that help us to interact with technology and with each other without the need for a bulky gadget. Typically, magnetically responsive devices are constructed using materials that do not necessarily possess flexible properties; so magnetosensitive composites with tailored magnetic, conductive, and flexible properties arising from the combination of their constituents were implemented. Here, it is described the use of these composites as printable sensors for magnetic field detection, with a focus on interactivity, safety, and holographic-like applications. A dedicated selection of materials and fabrication methods allowed to obtain stretchable, transparent, or self-healing properties, as well as explore their possibilities for printing them over large-area or even 3D printing. Additionally, it is shown the use of these magnetoresponsive composites as actuators, demonstrating their potential use in magnetic soft robotics by laminating magnetically sensitive devices that give them a sense of motion. Such applications become more technically accessible after the proposition of measurement strategies that remove artifacts in the magnetic signal coming from mechanical deformations. This thesis addressed several of the challenges related to cost, fabrication, and integration in magnetoresponsive composites, and is expected that related research might develop through multifunctional composites that sense more than magnetic fields.

Zusammenfassung

Diese Dissertation präsentiert neuartige Lösungen für die Herstellung funktionaler magnetoresponsiver Systeme mit dem Schwerpunkt auf der Entwicklung von magnetischen Kompositen als Sensoren und Aktuatoren. Derzeit besteht Bedarf an multifunktionalen mechanisch flexiblen Materialien, die einfach zu funktionalen Geräten verarbeitet werden können, die auf eine Vielzahl von physikalischen Reizen reagieren können, einschließlich magnetischer Felder. Diese Eigenschaften zielen auf die Entwicklung von leichten und unmerklichen Systemen ab, die uns helfen, mit Technologie und miteinander zu interagieren, ohne dass ein sperriges Gerät erforderlich ist. Typischerweise werden magnetisch ansprechende Geräte aus Materialien hergestellt, die nicht unbedingt über flexible Eigenschaften verfügen. Daher wurden magnetosensitive Komposite mit maßgeschneiderten magnetischen, leitenden und flexiblen Eigenschaften durch die Kombination ihrer Bestandteile implementiert. Hier wird die Verwendung dieser Komposite als druckbare Sensoren zur magnetischen Felderkennung beschrieben, mit einem Fokus auf Interaktivität, Sicherheit und holographischen Anwendungen. Eine dedizierte Auswahl von Materialien und Herstellungsmethoden ermöglichte die Erzielung von dehnbaren, transparenten oder selbstheilenden Eigenschaften sowie die Erkundung ihrer Möglichkeiten für den Druck über große Flächen oder sogar 3D-Druck. Darüber hinaus wird die Verwendung dieser magnetoresponsiven Komposite als Aktuatoren gezeigt, die ihr Potenzial in der magnetischen Softrobotik durch Laminierung magnetisch empfindlicher Geräte, die ihnen ein Gefühl von Bewegung geben, demonstrieren. Solche Anwendungen werden technisch zugänglicher, nachdem Messstrategien vorgeschlagen wurden, die Artefakte im magnetischen Signal, die aus mechanischen Verformungen resultieren, entfernen. Diese Dissertation befasste sich mit mehreren Herausforderungen in Bezug auf Kosten, Herstellung und Integration in magnetoreaktive Verbundwerkstoffe, und es wird erwartet, dass damit verbundene Forschung durch multifunktionale Verbundwerkstoffe weiterentwickelt wird, die mehr als magnetische Felder erfassen.

Contents

Acknowledgements ii

Abstract iv

Zusammenfassung v

Acronyms x

1 Introduction 1
- 1.1 Motivation and scope 1
- 1.2 Objectives 4
  - 1.2.1 Accomplishments 5
- 1.3 Structure of the Thesis 7

2 Background 8
- 2.1 Flexible and stretchable electronics 8
  - 2.1.1 Conductive composites 9
  - 2.1.2 Percolation theory 10
- 2.2 Flexible and stretchable magnetic field sensors 11
  - 2.2.1 Magnetotransport effects 11
  - 2.2.2 Printed Magnetic field sensors 13
  - 2.2.3 Thin film magnetic field sensors 15
- 2.3 Magnetic soft actuators 17
  - 2.3.1 Potential of soft actuators 17

3 Materials and methods . . . 21
3.1 Printing sensors and interconnects . . . 21
3.1.1 Printed interconnects . . . 21
3.1.2 Preparation of magnetoresistive flakes . . . 21
3.1.3 Formulation and printing of stretchable MR pastes . . . 22
3.1.4 Formulation and dispenser printing of LMR sensors . . . 22
3.1.5 Laser sintering of LMR sensors . . . 23
3.1.6 Encapsulation of printed LMR sensors . . . 23
3.1.7 Reforming of printed LMR sensors . . . 24
3.1.8 Printing and self-healing of MR sensors . . . 24
3.1.9 Printing of transparent MR sensors . . . 25
3.1.10 3D printing of MI sensors using L-PBF . . . 26
3.2 Thin film sensors and interconnects . . . 26
3.2.1 Flexible substrate preparation in PDMS coated carrier suibstrate . . . 26
3.2.2 Thin film interconnects . . . 27
3.2.3 AHE sensors fabrication . . . 27
3.3 Electrical characterization . . . 28
3.3.1 Magnetoresistance characterization . . . 28
3.3.2 Hall characterization . . . 29
3.3.3 SOT characterization . . . 29
3.3.4 Noise characterization for resolution determination . . . 30
3.3.5 Magnetoresistance during static bending . . . 30
3.3.6 Magnetoresistance during cyclic bending . . . 30
3.3.7 Magnetoresistance during static stretching . . . 31
3.3.8 Hall effect measurements during static bending . . . 31
3.3.9 Hall effect measurements during cyclic bending . . . 31
3.3.10 Hall effect measurements during non-deterministic bending . . . 32
3.4 Magnetic soft actuators . . . 32
3.4.1 Magnetic soft actuators based on PDMS-NdFeB particles . . . 32
3.4.2 Magnetic soft actuators based on DiaPLEX-NdFeB particles . . . 33
3.4.3 Magnetic soft actuators based on Irogran-Fe(chained) particles . . . 34
3.5 Materials characterization . . . 35
3.5.1 SEM . . . 35
3.5.2 Optical miscrocopy . . . 35

3.5.3 Contact angle . . . 35
3.5.4 Magnetic fields characterization . . . 36
3.6 Demonstrators . . . 36
3.6.1 Lamination of flexible sensors into target surfaces . . . 36
3.6.2 Human-Machine Interfaces . . . 37

4 Printing magnetic field sensors . . . 38
4.1 Overview . . . 38
4.2 Printed stretchable magnetic field sensors . . . 39
4.2.1 Flakes from thin films . . . 39
4.2.2 styrene-butadiene-styrene (SBS) block-copolymer as a suitable matrix for stretchable magnetic field sensors . . . 40
4.2.3 Sensing performance of printed magnetic field sensors based on flakes showing anisotropic magnetoresistance (AMR) effect . . . 42
4.2.4 Sensing performance of printed magnetic field sensors based on flakes showing giant magnetoresistance (GMR) effect . . . 44
4.2.5 Bending of printed magnetic field sensors . . . 46
4.2.6 Stretching of printed magnetic field sensors . . . 47
4.2.7 Printed magnetic field sensors for on-skin touchless HMIs . . . 49
4.3 Printing non-saturating large magnetoresistance (LMR) sensors towards large area and large volume applications . . . 51
4.3.1 Fabrication of printed sensors showing large non-saturating magnetoresistance . . . 51
4.3.2 Sensing performance of printed magnetic field sensors based on Bi powders showing LMR effect . . . 52
4.3.3 Bending performance . . . 53
4.3.4 Temperature stability . . . 56
4.3.5 Larger area interactivity . . . 58

5 Bringing magnetic field sensors to mechanically active surfaces . . . 64
5.1 Highly sensitive out-of-plane flexible magnetic field AHE sensors . . . 65
5.2 Cleaning the signal of strained magnetic field sensors . . . 66
5.3 Lamination of flexible AHE sensors in magnetic membranes for soft actuators 72
5.3.1 Tetherless folding of magnetic origami foils . . . 73
5.3.2 Assesing the folding of magnetic origami foils using flexible AHE sensors 76

5.3.3 Tuning the dynamic range of AHE sensors for feedback control of chained-Fe soft actuators . . . 77
5.4 Non-linear dynamics of magnetic soft actuators . . . 79
5.4.1 Dynamic actuation regimes of fast-moving magnetic soft actuators . 80

6 Unconventional formats for magnetic field sensors . . . 86
6.1 Printed magnetic field sensors with self-healing properties . . . 86
6.2 Transparent magnetic field sensors . . . 88
6.3 3D printed magnetic field sensors . . . 89

7 Conclusion and Further Work . . . 93
7.1 Outlook . . . 94

A Publication list . . . 115

B Scientific conferences . . . 117

C Patent applications . . . 119

Acronyms

0D	zero dimensional
"n"D	"n" dimensional
AAO	anodic aluminum oxide
AC	alternating current
AHE	anomalous Hall effect
AMF	alternating magnetic field
AMR	anisotropic magnetoresistance
Bi	bismuth
DAQ	data acquisition systems
DC	direct current
DMI	Dzyaloshinskii–Moriya interaction
DOF	degrees of freedom
FFT	fast Fourier transform
FM	ferromagnet
GMR	giant magnetoresistance
HMI	human-machine interface
IR	infrared
IP	in-plane
LMR	non-saturating large magnetoresistance
L-PBF	laser powder bed fusion
MI	magnetoimpedance
MR	magnetoresistance
NdFeB	neodymium-iron-boron
NPs	nanoparticles
OOP	out-of-plane
PCH	polyepichlorohydrin
PDMS	polydimethylsiloxane
PET	polyethylene terephthalate

PMA	perpendicular magnetic anisotropy
PBS	polyborosiloxane
PCB	printed circuit board
PVA	polyvinyl alcohol
Py	permalloy
SEM	scanning electron microscopy
Si	silicon
SD	standard deviation
SMD	surface mounting devices
SMP	shape memory polymer
SOC	spin-orbit coupling
SOT	spin-orbit torque
SOT	spin-orbit torque
SBS	styrene-butadiene-styrene
TMR	tunnel magnetoresistance
VHB	very high bonding tape
ZOH	zero-offset Hall

1 Introduction

1.1 Motivation and scope

If we travel back in time we would be able to attest that we have a long tradition of preparing mixtures. Already 100 000 years ago, our *H. Sapiens* ancestors had developed the know-how for preparing pigmented compounds. Evidence of conscious planning, mixture formulation, and painting applications by our ancestors have been found in relevant archeological sites like those found in the Blombos Cave in South Africa [1]. Inside this cave, vivid reddish pigments were obtained through the grinding of ochre clays mixed in a shell with some water and the fat coming from animal bones (Figure 1.1).

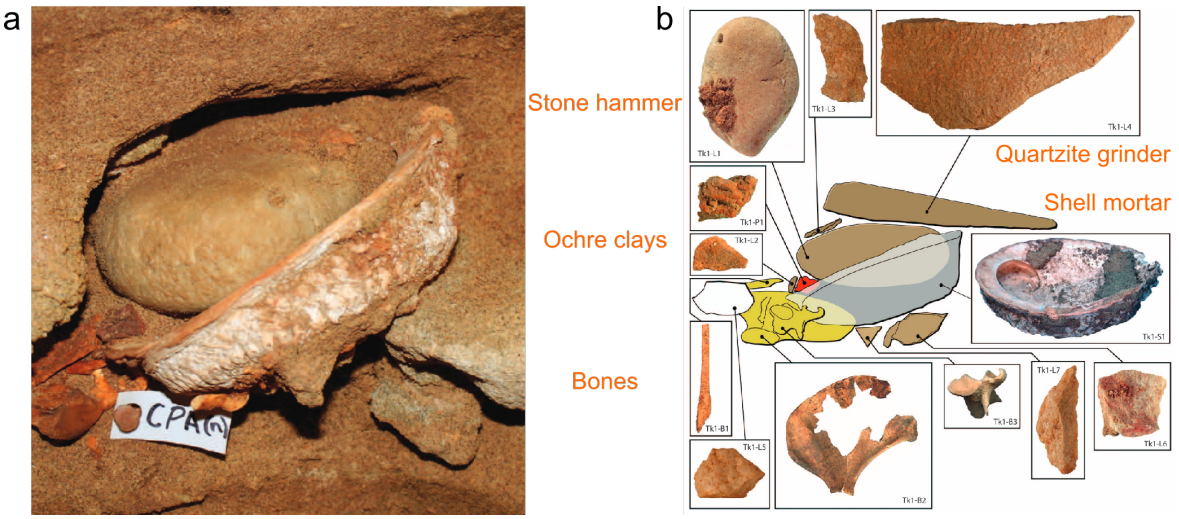

Figure 1.1: Ancient toolkit for processing ochre pigments. a) Photograph of an ochre-processing toolkit found in the Blombos Cave, South Africa. b) The toolkit contained tools for grinding, breaking, and processing pigmented compounds based on ochre clays, fat bone, charcoal, and water (From [1]. Reprinted with permission from AAAS).

Since then, our knowledge of preparing mixtures has kept evolving in a more systematized manner. We are able to understand naturally occurring mixtures like water and atmospheric air, and also other mixtures prepared by living organisms. The pigmented compounds created by our ancestors, needed to be mixed to profit from the color of the ochre powders and the tackiness of the animal fat to obtain a compound that was easily painted and adhered to the painted surface during a useful time [1]. In a similar way, humans prospering in hot weather, constructed their first mud houses using compound materials probably stimulated by termites that build their heat-insulating mounds from the mixture of soil, saliva, and dung [2]. Nowadays, we do more than mixing, we consciously mechanically engineer compounds to create high-performance composites [3]. Our understanding of mixtures has impulsed the emergence of cosmetics, fuel, medicines, vaccines, and various other functional materials and compounds (Figure 1.2). On a day-to-day basis, we make deliberate mixtures to obtain physical or chemical properties that have a better performance than the individual constituent materials.

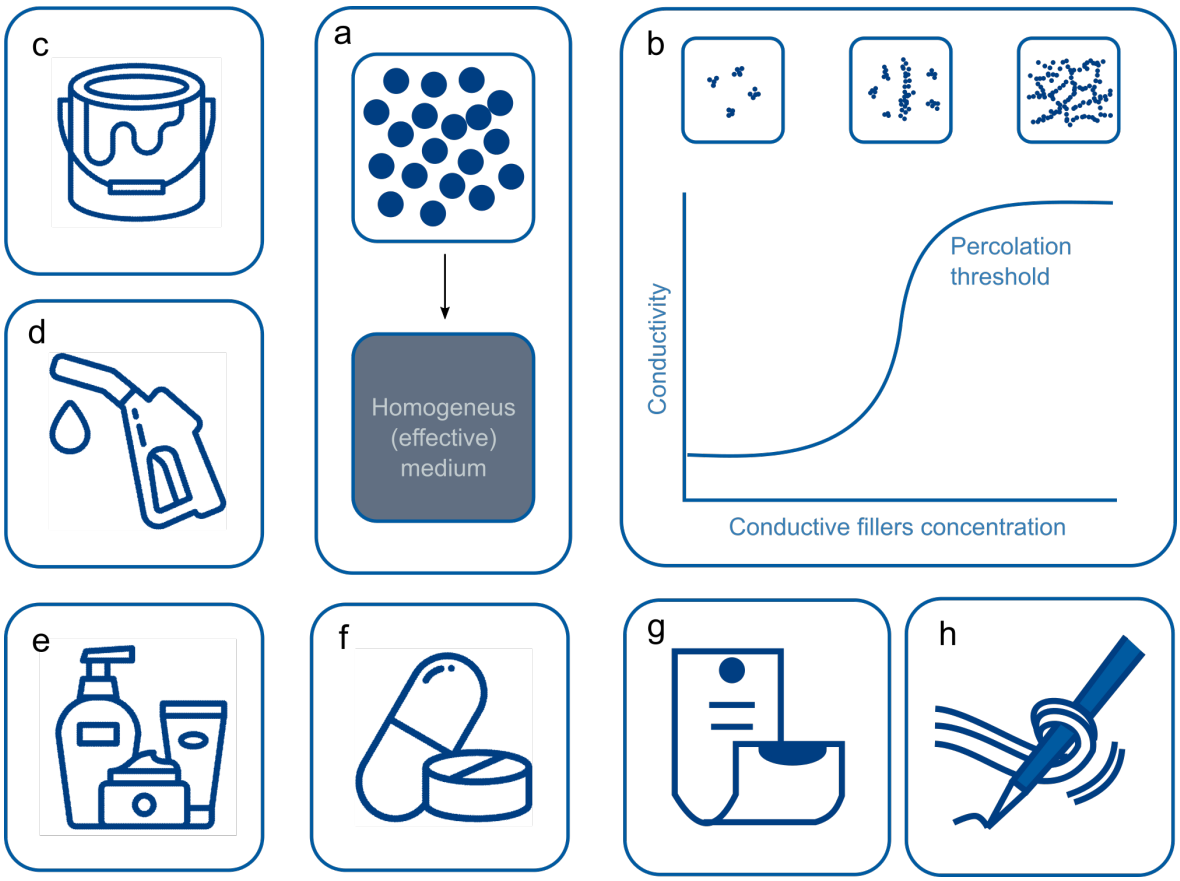

Figure 1.2: Functional mixtures and compounds. Our understanding of mixtures has been studied using different frameworks like the a) Maxwell's continuous approach and the b) percoaltion theory describing the fractal networks built after adding different concentrations of conductive fillers [4]. Such framework examples, have enabled the development of c) paints, d) fuels, e) cosmetics, and f) medical treatments. Here, functional mixtures are developed for g) flexible electronic and h) soft actuation applications (This figure has been designed using images from Flaticon.com).

With the aim to keep developing functional mixtures, in this work, I will elaborate on the benefit and applications of engineered mixtures composed of magnetosensitive powders into flexible polymers to obtain functional magnetically responsive devices. The fabrication of magnetic polymeric composites has emerged as an alternative solution to the challenge of creating stable bulk polymers with intrinsic magnetic ordering [5, 6]. Achieving ferromagnetic ordering in a purely organic material at room temperature is a difficult and often controversial task that has been made possible through the stabilization of free radicals in organic polymers [5]. However, the magnetization of purely organic plastic magnets is relatively low (10^{-4} emu g^{-1}) compared to composite magnetic polymers that incorporate NdFeB (0.5×10^{2} emu g^{-1}) or Fe_3O_4 (0.5×10^{1} emu g^{-1}) fillers [7, 8]. One may think that the addition of such solid fillers might strongly affect the flexibility of the host polymer. Nevertheless, these polymeric composites only change their intrinsic Young's modulus in less than one order of magnitude with the addition of up to 50 wt% concentration of magnetic fillers [8]. This means that magnetoresponsive flexible materials can be easily obtained without sacrificing the intrinsic mechanical performance of well-developed soft polymers.

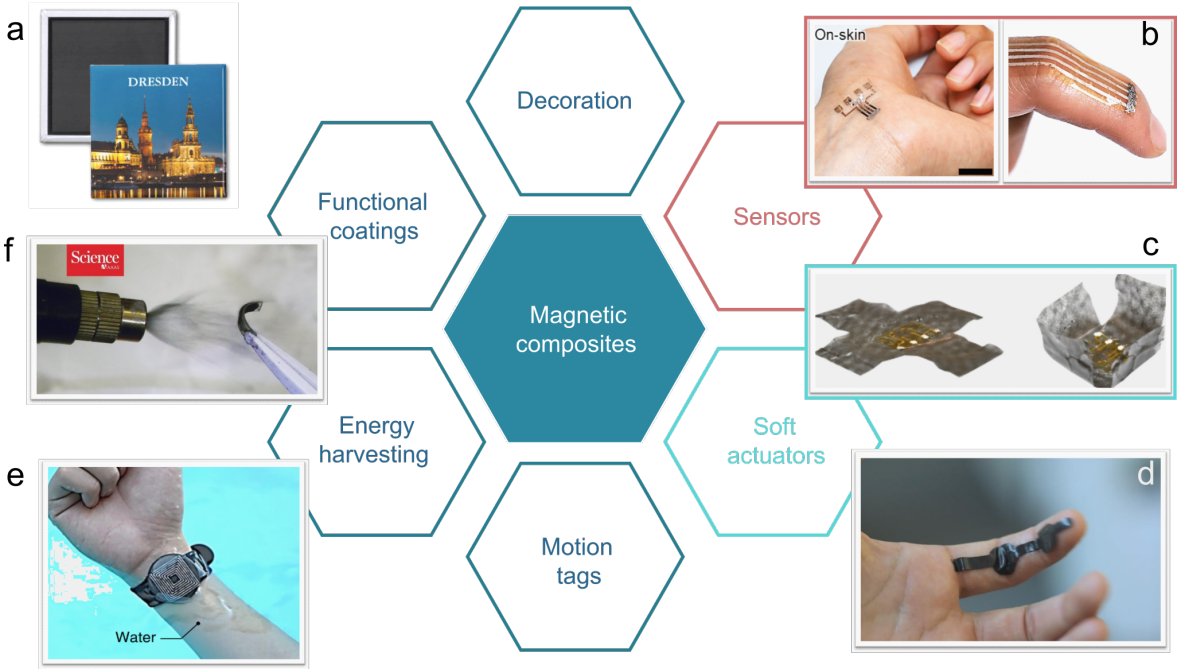

Figure 1.3: Examples showing applications of flexible magnetic composites. Flexible polymeric composites embedding magnetic particles can have different applications. a) From decorative magnet souvenirs (This figure has been designed using images from zazzle.de) to more advanced applications, the development of such composites can be used as functional materials for b) sensors ([9], used under CC BY), c) soft actuators ([10], used under CC BY), d) motion tags ([11], used under CC BY 4.0), e) energy harvesting ([12], Reproduced with permission from Springer Nature), and f) magnetic spray coatings (From [13]. Reprinted with permission from AAAS).

Examples and applications of magnetoresponsive composites have been broadly reported in the literature (Figure 1.3) [14]. From the usage of plastic bonded magnets in magnetic

car mounts to the novel development of magnetic wearable energy harvesting devices [15], magnetic composites can address several technology fields. As depicted in Figure 1.4, through this thesis I explore the technologies arising from the combination of magnetic properties in conductive and/or flexible composites. I investigated the magnetotransport effects and actuation behavior of magnetic polymeric composites, which have been demonstrated for prospective possible applications in proximity sensing, touchless human-machine interfaces, or tetherless actuation mechanisms [16–18]. Building on previous efforts in this area, the general goal of this work is to propose novel approaches to address some of the most common challenges in printed sensors, laminated thin film sensors, and soft actuators that respond to magnetic fields.

1.2 Objectives

From the identification of the research gap, through the composite fabrication, to their implementation, I develop solutions directed towards the fabrication of functional highly integrated magnetoresponsive systems. The general objectives of this work are related to the development of magnetic composites used as sensors and actuators which can be summarized as:

- Fabricate magnetoresponsive composites that benefit from the combination of the magnetic, electrical conductivity, and flexibility of the constituent particle fillers and matrices.
- Direct the progress of magnetic composites towards technologies related to magnetic field sensing and actuation.
- Evaluate the magnetotransport and actuation effects in magnetic composites.
- Provide solutions to the challenges associated with technologies based on magnetoresponsive composites.
- Develop demonstrative scenarios that expand the prospective impact of magnetic-composite-based technologies.

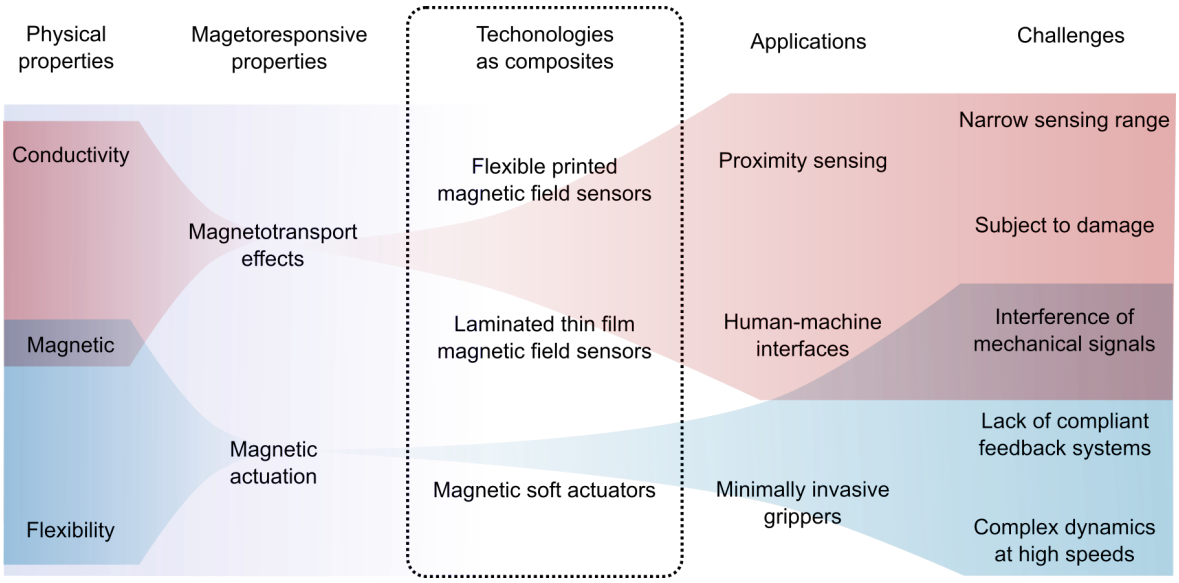

Figure 1.4: Diagram that illustrates the studied technologies in this work. Magnetoresponsive composites are studied through the integration of different physical properties, along with their potential applications and associated challenges.

1.2.1 Accomplishments

Flexibility in magnetic composites is a useful feature but also a challenge. The tasks accomplished during the presented doctoral research include scientific and technological advances to enhance the sensing and actuation performance of magnetically sensitive composites. Such accomplishments can be summarized as:

- Extended the framework to develop printable magnetically sensitive materials for magnetic field sensors.
- Expanded the dynamic range of printable magnetic field sensors in more than three orders of magnitude, establishing the current limits from 36 nT to 5 T at room temperature.
- Organized the workflow for the characterization of noise, sensitivity, and resolution of magnetic field sensors.
- Setting up of the methods for making magnetotransport characterizations of samples in static and continuously bent samples.
- Integrated for the first time flexible magnetic field sensors with highly compliant magnetic skins to avoid the need for bulky magnets and sensors.
- Contributed to the development of fully-electrical strain decoupling strategies from the magnetic field signals of mechanically deformable sensors.

- Collaborated on the development of a novel area of application of flexible magneto-electronics for feedback-controlled magnetic actuators.
- Understood and implemented the magnetic and mechanical properties of flexible composites for their application in soft actuators.
- Expanded the useful dynamic ranges of magnetic soft actuators to the chaotic regime.
- Used non-conventional formats of magnetically sensitive materials to enable repairable, visually imperceptible, or geometrically customized platforms.
- Implemented one already developed patent and additionally submitted 2 patent applications to HZDR Innovation GmbH for the detection of magnetic fields in flexible and printed magnetic field sensors (Section C).
- Actively participated in technology transfer activities of magnetic composites by joining to the HZDR Innovation GmbH team.
- Involved in the preparation of demonstrators exhibited as technology concepts in industrial trade fairs (LOPEC, Electronica)
- Participated in regional and international exhibition events (SPIN 2030, Long Night of Science) highlighting the current and future applications of magnetically sensitive devices and actuators.
- Presented the scientific results at national and international conferences with contributed talks and poster presentations (Section B).
- Took part in the interdisciplinary discussion of my research topic with other doctoral candidates in the DocSeminars organized at HZDR.
- Collaborated and performed joint sensor development with internal (department of "Intelligent Materials and Systems" at the Helmholtz-Zentrum Dresden-Rossendorf), national (Fraunhofer-Institut für Keramische Technologien und Systeme, Fraunhofer-Institut für Werkstoff- und Strahltechnik) and international (North Carolina State University) research partners.
- Fully involved in the preparation of peer-reviewed articles as first and contributing author from writing to experimental and figure design (Section A).
- Extended the reach of the work by designing the artwork published as cover pages, and back cover pages of scientific journals (Figure A.1).

1.3 Structure of the Thesis

The structure of this manuscript is as follows: it begins by discussing the current developments and challenges in the area of magnetic composites, followed by the methods to obtain functional magnetic composites. Then, the results that I obtained during my doctoral research are presented, to finish with the proposal of novel investigation directions that might expand the opportunities of flexible magnetoresponsive devices.

Chapter 2 contains an overview of the relevant physical and magnetoresponsive properties of magnetic composites. During this chapter, the relevant literature and research gaps are addressed to understand the motivations for each of the presented developments.

Chapter 3 describes the general methods employed during the development of magnetically responsive composites. The methods to fabricate printed and thin film magnetic field sensors, as well as different types of magnetic soft actuators are reported. The general material characterization methods to study the composite systems are also detailed. Especially relevant for the development of flexible devices, the steps to study their performance upon mechanical deformations are especially emphasized.

In Chapter 4, the development of different types of composite pastes used for printing magnetic field sensors is described. It shows their potential to create stretchable magnetic field sensors for the implementation of on-skin human-machine interface (HMI), as well as their printing over larger areas to obtain interactive smart surfaces.

The implementation of magnetic field sensors in mechanically active surfaces like human skin and magnetic soft actuators is shown in Chapter 5. There, I emphasize on the use of zero-offset Hall (ZOH) switching current technique to remove mechanical strain contributions from the magnetic signal of constantly deformed flexible sensors. The integration and motivation of flexible sensors in magnetic soft actuators are also elaborated.

The proposed prospective directions for the development of flexible sensors and actuators are summarized in Chapter 6. Unconventional formats for magnetoresponsive systems like transparent, self-healable, and 3D printed, are shown to be useful characteristics for seamless implementation in durable, imperceptible, and multifunctional devices.

Chapter 7 states the main contributions of the present work and the foreseen directions of the development of magnetic composites.

2 Background

This chapter offers a general overview of the previous and recent work sustaining the development of flexible and stretchable devices based on magnetotransport effects as well as the main physical effects occurring on mechanical systems categorized as magnetic soft actuators that trigger their motion through their interaction with magnetic fields. Flexible electronics are introduced focusing on the development of highly deformable systems achieved using stretchable composites. Such composite systems are described by the percolation theory that is mentioned in the text to describe the conductive behavior of conductive fillers embedded in a non-conductive matrix. This work is supported by the previous efforts to implement various magnetically sensitive devices in flexible and stretchable formats, so the description of these phenomena, as well as their implementations, are mentioned. Expanding beyond electrically conductive devices, this chapter states the basis of the mechanical contributions of the interaction of mechanically soft magnetic composites with applied magnetic fields. Apart from enunciating the past and recent developments, some of the main accompanying challenges for the widespread of these technologies will be elaborated to frame the experimental path that guided the obtained results.

2.1 Flexible and stretchable electronics

Metals are electrically conductive materials that a certain extent are intrinsically flexible. Large amounts of electrons move freely along the crystal structure of metals making them highly mobile charge carriers [19]. The electrical cables and wires that power our electronic

devices use metals not only because of their high conductivity but also because of their ductility properties [20]. Flexibility carries many advantages, long cables are more easily transported in reels, are easily installed in tight spaces, and increase reliability so connected devices can be moved around without losing the electrical connection [21]. But there is a limit, bulk metals can only withstand below 1% in elastic strain, and up to 10% at micro and nanoscales [22]. Scientists have investigated for several years new approaches to get >10% strain in reliable conductive materials [23]. Applications are the main driver of such a goal; wearables, flexible displays, motion harvesting devices, and flexible batteries are on the table because of the possibility to have flexible and stretchable functional devices [24–26]. If applications are not exciting enough, new applied and fundamental physics can be studied in flexible electronics [27, 28].

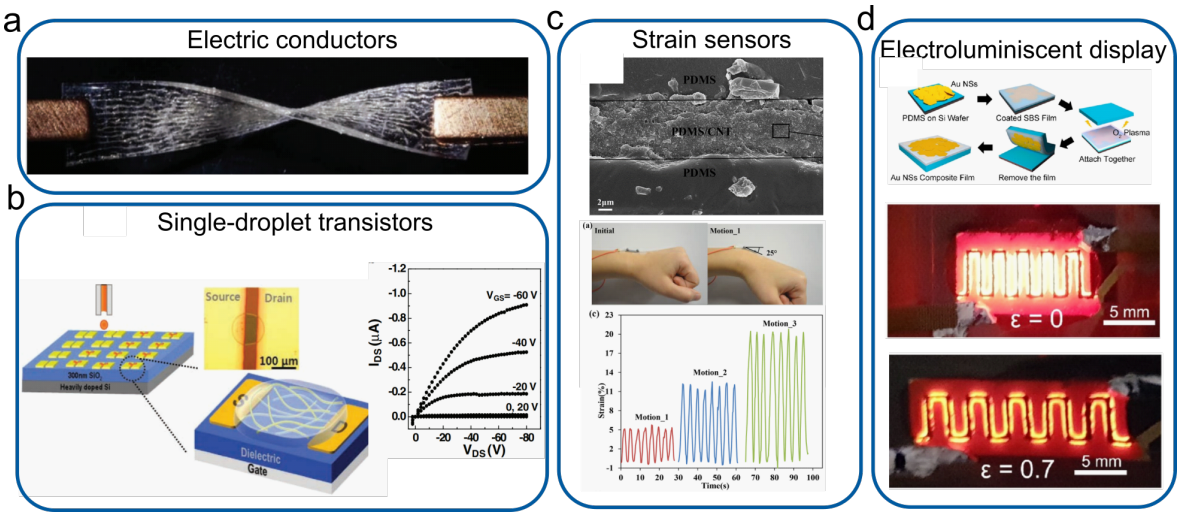

Figure 2.1: Solution processable deformable electronics. a) Electrically conductive composites can be obtained using conductive fillers into deformable elastomers ([29], used under CC BY). b) Transistors from a droplet containing semiconducting fillers ([30], used under CC BY). c) Strain sensors from carbon nanotubes embedded in polydimethylsiloxane (PDMS) matrix (Reprinted with permission from [31]. Copyright 2018 American Chemical Society). d) Stretchable electroluminescent composite used as a display (Reprinted with permission from [32]. Copyright 2018 American Chemical Society).

2.1.1 Conductive composites

Conductive materials showing high resilience to deformation can be obtained in different ways [33]. From thin films on flexible substrates [34], through liquid metals [35], to conductive polymers [36], different approaches have been tested for developing flexible electronics. Among others, using conductive composites is a practical approach for this purpose (Figure 2.1) [4]. Conductive fillers in a polymeric matrix act as a complex highway network to transport electrons through the mechanically flexible material. Recurrent examples showing Ag or Au fillers embedded in PDMS and other elastomers have been used as flexible and

stretchable conductors achieving up to 1.8×10^3 % strain [37–39]. Depending on the fillers and matrix properties, new functionalities beyond electricity transport can be developed. Composites showing stretchable electroluminescent displays have been obtained from the electrical polarization of ZnS:Cu microparticles in a PVDF-HFP matrix [40]. Flexible energy storage and harvesting devices can be obtained using stretchable conductors with high surface area using graphene oxide and yarn fiber-like structures [41, 42]. Profiting from the piezoelectric effects of conductive fillers, wearable strain sensors have been demonstrated. For example, carbon nanotube-based sensors demonstrated enough sensitivity to detect the muscle motion of skin close to the throat during speech [43]. In biomedical applications, composite-based sensors have been demonstrated to track heart beat rate, and nerve pulse detection and stimulation [44, 45]. Profiting from the high compliancy of the polymers and the conductive transport phenomena of the fillers, highly integrated technologies are in constant development.

2.1.2 Percolation theory

The basics to understand the mixture constituents configuration and their properties started with Maxwell and Rayleigh's studies of the physicochemical properties of colloidal systems [46]. Since then, much research has been done to arrive at using conductive composites as mixtures useful for printable electronic applications. Colloids containing fillers in a dispersing medium are typically disordered systems, well-organized particles distributed in a medium are rare exceptions [47]. Different models have been developed to effectively describe these complex disordered systems, such as those describing aggregation of particles with fractal geometry and through percolation theory [48–50]. In materials science, percolation theory describes the interactions and system evolution of random networks of particles in a dispersing media [4]. Consider the conductivity inside a suspension with metallic conductive fillers (Figure 1.2b). Start with a small concentration of particles, there will be few agglomerates of particles in a solution. Adding more fillers increase the number of agglomerates that can start to cluster between them. Clusters grow with the addition of metallic fillers until the clusters are close to each other. Additional conductive fillers will connect neighboring clusters, suddenly forming a complex conductive network. Going to saturation of the solution, more interconnections between already formed clusters will reinforce. The concentration at which clusters are linked between them to form a network is called the percolation threshold which

is characterized by a sudden change in the conductivity of the system [51]. The conductivity of such a system can be reduced to the equation 2.1,

$$\sigma_c = \sigma_f (V_f - V_{th})^s \tag{2.1}$$

with σ_c and σ_f being the conductivity of the composite and the fillers, respectively; V_f and V_{th} the volume fraction of the filler and the volume of percolation threshold; and s the critical exponent of conductivity. But the equation 2.1 does not describe how different parameters of the suspension will affect the percolation, such as shape, size, surface energy, viscosity, etc [52]. For this reason, empirical and Montecarlo simulation results have been used to set the guiding design principles for achieving high-performance percolation networks [53, 54]. The percolation threshold is reduced with high aspect ratios and broad size distribution [4]. Contact areas between fillers are smaller than their total surface areas. Enhancing the chance of contact by increasing the dimensionality to 1D (nano- and microwires) and even 2D (nano- and microflakes) has been proved as an effective method to increase the contact between particles [55, 56].

2.2 Flexible and stretchable magnetic field sensors

2.2.1 Magnetotransport effects

Among the applications for flexible and stretchable composites, the implementation of fillers responding to magnetic fields is not often revisited but has great potential for applications. In conductive composites, the direct implementation of magnetoresistance effects is one of the possibilities to obtain magnetically sensitive composites.

Magnetoresistance effects are observed as changes in the conductivity of a material upon the application of an external magnetic field. Magnetoresistance has been reported since the observations of Thomson in 1857 [57] and can have different behaviors and origins. Here, I summarize the main magnetoresistance (MR) effects used in conductive composites:

- Ordinary magnetoresistance. The resistivity of the material increase with the applied magnetic field due to the Lorentz forces deviating the electrons from the direction of the electric field direction. Thus, the electrons flowing in the material experience larger trajectories reducing their effective mean path. This effect is observed in all metals but

is often neglected due to their small contribution to changes in resistance at room temperatures [58, 59].

- AMR. Observed in ferromagnetic materials like Ni, Fe, Co, and their alloys. It originates from the spin-orbit coupling (SOC) modulation changing the scattering rate and density of states of the charge carriers depending not only on the intensity but also on the direction of the applied magnetic field [60]. Classically AMR effects are below 5% at room temperature.
- LMR. Is a type of magnetoresistive behavior that shows large changes in resistivity that do not show signs of saturation at large fields. Materials like WTe_2, NbP, and Bi have shown this behavior from low to room temperatures. The typical resistance changes can go from 10^3% to 10^5% in applied fields above 20 T at room temperature [59, 61, 62].
- GMR. Multilayers of ferromagnetic and non-ferromagnetic materials coupled with an antiferromagnetic-like ordering will show a tunable *giant* change in resistivity with the intensity of the applied magnetic field [63, 64]. In this case, the resistance decreases as a result of the reorientation of magnetization of the ferromagnetic layers reducing the effective scattering due to inverted spin carriers [65]. The coupling between successive ferromagnetic layers has to be properly tuned and strongly depends on the thickness of the non-magnetic spacer [66]. The amplitude of the GMR effect can typically go from 10^1% to 10^2%.

Hall effects are an additional type of phenomenon that illustrates the interaction of the transport carriers with magnetic fields. Normally measured by the geometrical accumulation of specific carriers along the conductor material, different phenomena have been measured in flexible magnetosensitive systems:

- Conventional Hall effect Originally discovered by Hall in 1879 [67], recurrently used to study transport phenomena in electrically conductive and semiconducting materials [68]. A transversal voltage is generated in a sample with respect to the current I and an applied magnetic field B. The origin of the charge accumulation is the Lorentz force and is measured as a Hall voltage V_{Hall} that can be used to calculate the Hall resistance R_{Hall} as

$$R_{Hall} = \frac{V_{Hall}}{I}. \tag{2.2}$$

The supply current-related Hall sensitivity is a helpful parameter to characterize the performance of the sensors

$$S = \frac{1}{I}\frac{dV_{Hall}}{dB}. \tag{2.3}$$

- **anomalous Hall effect (AHE)**, is observed as an additional contribution to the transversal Hall voltage due to SOC. This effect is pronounced in materials with broken time symmetry like those showing ferromagnetic ordering. In these materials, the electronic band structure is spin-dependent and the spin-splitting of the bands can give rise to a large Berry curvature, which in turn leads to a large intrinsic contribution to the Hall signal [69].

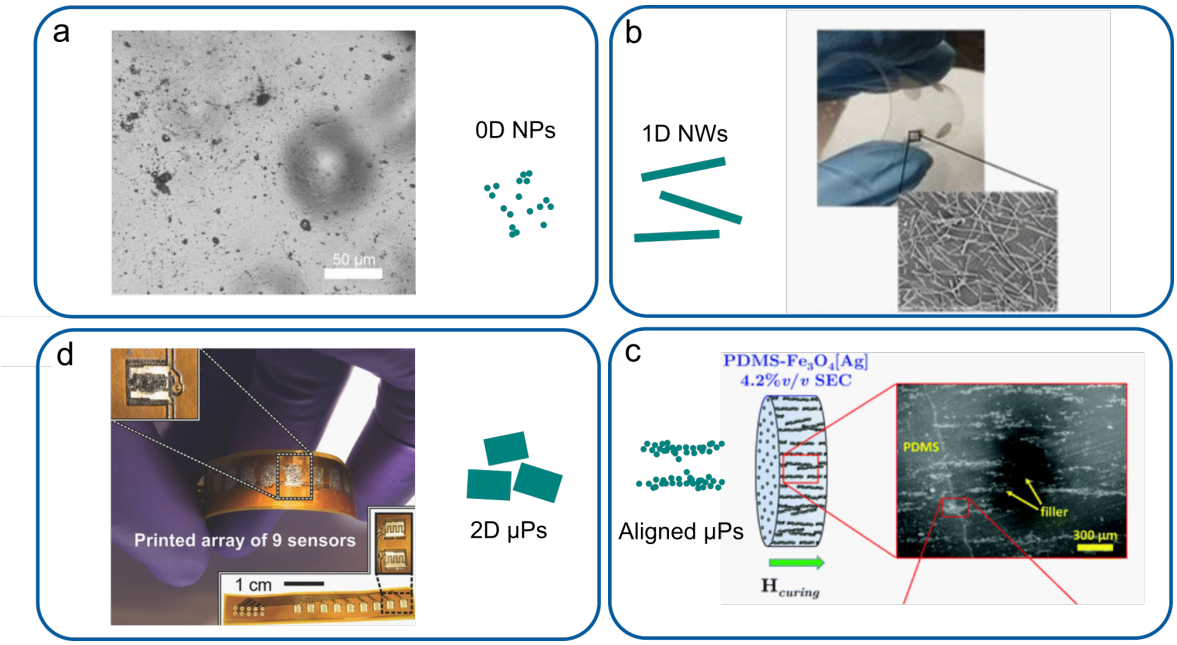

Figure 2.2: Solution processable magnetic field sensors. a) Magnetic field sensor composite based on 0D Co nanoparticles embedded in a gel-like matrix ([70] © IOP Publishing. Reproduced with permission. All rights reserved). b) GMR nanowires (1D) transferred to a flexible substrate (Reprinted from [71], with permission from Elsevier). c) Magnetically aligned magnetite microparticle used for anisotropic magnetic field sensing (Reproduced from [72] with permission from the Royal Society of Chemistry). d) Array of printed magnetic field sensors based on GMR flakes (2D) obtained from thin film deposition ([16], used under CC BY).

2.2.2 Printed Magnetic field sensors

Profiting from the abovementioned magnetotransport effects and electromagnetic interactions, it is possible to create composite-based systems that sense magnetic fields. In these terms, different solution-processable devices that measure magnetic fields have been proposed. For example, using composites with embedded coils is a proven approach to detect alternating magnetic fields by the current induced [73, 74].Coil-based systems are strongly dependent on the size of the coils and the resolution of the printing, giving rise to a

limited frequency range sensitivity. Another approach is fabricating conductive composites with MR properties to be used as sensors (Figure 2.2) [70, 71, 75]. Combining magnetic conductive fillers inside a polymeric matrix resulted in magnetic composites sensitive to magnetic fields. This approach has been demonstrated with 0D Co nanoparticles [70], 1D GMR nanowires [71], chained microparticle arrays [76], and also 2D structures like microflakes [16, 75, 77]. After these initial efforts one decade ago, some additional solution processable magnetoresistive conductive composite examples have been developed [72, 78–83].

Printable magnetic field sensors might offer the potential to scale significantly the production of magnetic field sensors that can be adapted to systems for the Internet of Things, wearables, and consumer applications. The challenges associated with printable resistive magnetic field sensors are related to their limited dynamic range, restricted compatibility with mechanical deformations, susceptibility to damage during operation, and interference of non-magnetic stimuli in their sensing response. The widespread of this technology still has some opportunities to increase its performance:

- Until recently, the estimated highest sensing range of resistive printed magnetic field sensors was restricted from 100 μT to the 1 T range [84]. While classical solid-state magnetoresistive sensors can detect fields in the range of 10^{-9} to close to 10^{2} T [85, 86], the estimated highest sensing range of resistive printed magnetic field sensors was restricted from 10^{-4} to 1 T. The limitation in the low fields is related to the relatively high noise and low sensitivity of the obtained composites, while the limitation in the high fields is due to the saturation of the MR signal with large magnetic fields. In this manuscript, I will provide different approaches to expand the dynamic range of magnetoresistive printed sensors beyond these ranges by employing particle alignment strategies and using non-saturating magnetoresistive fillers.
- On-skin laminated printed sensors might offer customized sensing interfaces that adapt to the body of the user. Printed sensors can be easily integrated into flexible substrates, but until recently there were no examples of printable magnetoresistive sensors compatible with stretchable substrates. Profiting from existing examples of stretchable conductive composites, we identified the possibility to create printable stretchable magnetoresistive sensors. Stretchability might come with the possibility to integrate this technology for ultra-wearable and on-skin applications where large deformations might occur above 10% strain.

- Producing sensors via printing techniques is known to be useful for a high-throughput and cost-effective way of producing sensing arrays over large areas. Until recently, just one example emphasizing large volume production of magnetic field sensors had been demonstrated [83]. Nevertheless, the extensive distribution of printed magnetic field sensors would require thinking in the complete supply chain to satisfy a prospective broad demand for magnetically sensitive inks. Candidate high-performance magnetosensitive materials are typically difficult to produce in a cost-effective way. For example, the fabrication of GMR flakes requires fine tunning and multistep deposition of nm scale thin films [83]. An alternative widely available material showing a large magnetoresistive effect is needed.
- Flexible printed sensors might have an increased risk of damage compared to rigid technologies [24]. This is because they might be continuously deformed when laminated on dynamically moving surfaces. Additionally, when laminated on the surface of the target substrate, they will be the uppermost layer that might suffer from scratches or environmental conditions. There is a current need to provide technological solutions that increase the reliability of printed sensors in the long term even after unforeseen damage.

2.2.3 Thin film magnetic field sensors

The second fabrication strategy to produce magnetic field sensors discussed in this manuscript is the thin-film deposition of metals [87]. Thin film sensors are more widely spread along different research areas and are the current strategy for many current technologies in the market. Flexible form factors are in continuous development, aiming to extend the capabilities of thin films. In particular for flexible magnetic field sensors, there are many examples showing AMR [88, 89], GMR [90], spin valves [91, 92], and Hall effect devices [93, 94]. By employing ultrathin substrates, it has been possible to show flexible and even stretchable magnetic field sensors based on thin film fabrication technologies [17, 95]. Flexible thin film magnetic field sensor performance has been proved sensitive down to 2×10^{-7}T in-plane (IP) magnetic fields and up to 0.3 T [94, 95]. Flexible thin-film AMR sensors have been used as angular sensors for an on-skin compass-like device detecting the geomagnetic fields [96]. GMR-based stretchable devices, on the other hand, have been used for proximity applications mounted in stretchable carriers [97]. Using a spin valve array, a touchless dial interface was possible by detecting the changes in orientation of the sensor with respect

to a cylindrical permanent magnet [98]. Additionally, Hall effect sensors have been proved useful in the control of levitating magnetic suspension systems profiting from the out-of-plane sensitivity of Bi-based sensors [93]. All these applications have profited from the high compliancy of the sensors fabricated in thin foils that can be mounted in a target substrate with minimal mechanical interferences [97].

Thin film sensors show high performance and they are expected to be implemented in future light and portable technologies after addressing some of their current challenges:

- Most of the examples up to date tend to have IP sensitivity to magnetic fields. Only a few examples based on thin film deposition showing out-of-plane (OOP) sensitivity exist. These have been achieved employing Bi thin films and spin valves showing large perpendicular magnetic anisotropy (PMA) [93, 99, 100]. While monolayers of Bi are relatively easy to obtain to create a Hall effect sensor, the sensitivity of Bi is only in the range of 1 ΩT-1 [99] (3 orders of magnitude lower than commercial semiconducting sensors); on the other hand, GMR-based spin valves need precise tuning to achieve the desired antiferromagnetic OOP coupling [100], so they are not easy to scale in large volumes.
- Limited performance during continuous deformations. Being based on conductive materials, thin film sensors are subject to changes in resistance when they are not mechanically conditioned. While strategies to diminish these effects exist, like geometrical IP and OOP buckling, and neutral plane encapsulation strategies [95], an electrical method that removes the mechanical contributions from the sensing signal will increase the seamless fabrication of flexible sensors without increasing the processing steps from the other methods. Previous examples to remove misalignment effects and other offset contributions in the sensing signal of Hall effect sensors exist, these strategies based on switching the direction current during the Hall measurements will be explored in this manuscript.
- Use case scenarios are still to be broadened. Like other flexible electronic technologies, flexible magnetic field sensors still have a way to go to show performance comparable to their rigid counterparts [24]. Meaning that instead of replacing the widespread rigid technologies, the scientific and industrial community still has to find killer applications for the implementation of flexible systems. In these applications, the performance can be compromised by the appropriate form factor owing to their mechanical properties. Until recently, there was no exploration of the use of flexible magnetic field sensors

in the area of soft robotics [101], where the smart combination of mechanically imperceptible thin film sensors might work as useful feedback systems for the control of the actuation of such flexible robots.

2.3 Magnetic soft actuators

2.3.1 Potential of soft actuators

The employment of magnetic composites can go beyond their use as printable materials for sensing magnetic fields. Using the flexible properties of these materials, deformations can occur after applying magnetic fields expanding the application scenarios of these composites. Humans have been repurposing materials for a long time. If we take our example from the Blombos Cave [1], prehistoric *H. Sapiens* were already using stones and shells as mortars. Tools and devices facilitate our tasks on a daily basis and expand human capabilities. With the development of automatized tools, a machine can be left operating with minimal human supervision, effectively delegating a lot of our activities to robots that perform repetitive tasks in an efficient way [102]. Robotic systems are nowadays at the core of most of the major manufacturing processes [103]. Mechanical robots allow for the high-volume production of processed goods using a smart combination of mechanics, electronics, and computation [104]. Mechatronic systems are typically controlled by a computer connected to a set of sense- and state-reporting devices [105]. Such feedback systems check for the correct operation of the automated linear and rotating actuators that move in a precise and controlled manner.

Typically, the most advanced single actuators (holonomic actuators) are designed to achieve up to six degrees of freedom (DOF), which increasingly adds up to the complexity of the feedback-reporting requirements of the actuating systems [106]. DOF describe the possible translations and rotations that a body can exert. For a rigid body, these are limited to 3 translations like walking (forward-backward), strafing (left-right), elevating (up-down), and rotations like roll, pitch, and yaw [107]. Systems of joints and actuators can achieve more than 6 DOF like the arm joints enabling grasping objects at any point from distinct directions [108].

Inspired by the broad motion capabilities of the biomechanics of living organisms, the scientific community has dedicated efforts to mimic these functional mechanisms [109].

Unlike their rigid linear and rotational actuator counterparts, soft actuators can be considered as a continuum of joints and connectors that give rise to an infinite number of degrees of freedom [101]. Think in a simple back-and-forth movement of an end-effector. In a linear actuator the motion can be achieved by translating the end-effector between the two position states, on the other hand, in a soft actuator these results can be achieved by an infinite number of configuration patterns. It might sound that the added complexity to achieve the same result is detrimental to the desired output, but from another perspective, the complex motion patterns of soft actuators open a broader set of solutions to solve a motion problem [110]. If an obstacle is placed in front of the simple linear actuator, it will be impossible to complete the motion task, but a soft actuator may be able to circumvent the obstacle to complete the translation task. Basically, soft actuators profit from their large number of DOF and configurations to provide flexible solutions in unexpected conditions. This behavior is very similar to living organisms that have developed motion and processing mechanisms that allowed us to adapt to unforeseen circumstances.

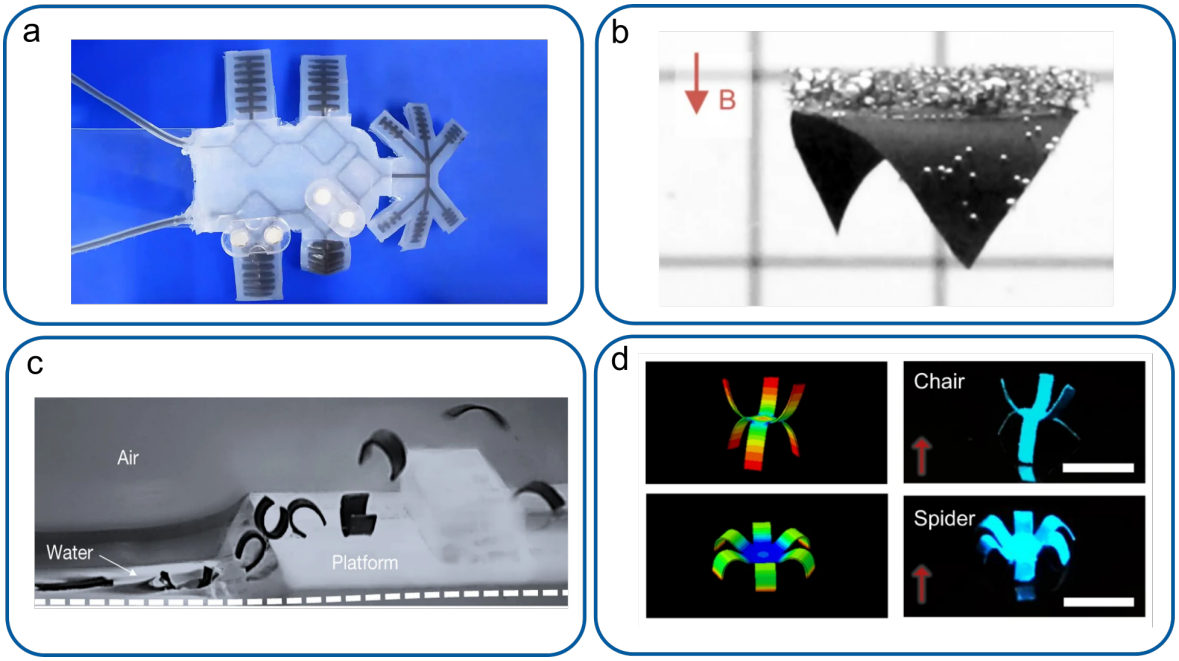

Figure 2.3: Magnetic soft actuators. a) Soft actuator using the magnetorheological response to move upon the application of external magnetic fields ([111], used under CC BY 4.0). b) Magnetic membrane of NdFeB/PDMS moved remotely for cargo transport underwater ([112], used under CC BY). c) Multifunctional magnetic actuators that swim, roll, jump and walk over different obstacles ([113] Reproduced with permission from Springer Nature). d) Reconfigurable magnetic membrane that assembles into different shapes depending on its magnetization profile ([114], used under CC By 4.0).

Based on these principles, soft actuators have been proven useful for universal grippers, machines that can hold varied objects without the need for redesigning the gripping arm [115]. Universal gripers have been shown as multifunctional machines that can hold delicate objects like glassware, or soft objects like tennis balls, with a variety of shapes and weights

[116]. Soft grippers benefit from the high compliancy of their constituent materials to conform to the surface of the target surface providing a very reliable and adaptable grasp to the target surface. Apart from grippers, soft actuators had been demonstrated for direct and secure interventions with humans [117]. This is possibly one of the main goals of the area, to be able to create safe and seamless machines that can collaborate directly with humans naturally adapting to our biomechanics [109]. This may create mechanical aids for rehabilitation, fine motricity, accessibility, surgery, and general assistance in motor tasks [118]. For this aim, soft actuator systems that are light, energy efficient, and smart systems are in development. Different inputs, such as pneumatic, thermal, electric, magnetic, and others, have been used to stimulate the motion of soft actuating systems [119–122]. Among them, magnetic interactions driving the actuation of soft materials are highly beneficial to obtain untethered, light, and reconfigurable motion (Figure 2.3) [123, 124].

Magnetic soft actuators respond differently based on the coercive field of their fillers [14]. During the application of an externally applied magnetic field, the constituent magnetic fillers can be remagnetized or not, giving rise to different interactions:

- Magnetically soft materials typically tend to have a gradient-mediated actuation, where the exerted force is dependent on the magnetic field gradient $\nabla\mathbf{B}$ and the magnetization $\mathbf{M}$, as summarized by the equation

$$\mathbf{F} = \nabla\mathbf{B} \cdot \mathbf{M} \tag{2.4}$$

- Magnetically hard materials will not change their magnetic momentum during the application of the magnetic fields used for actuation. In such cases, torques may arise with respect to the intensity and direction of the applied magnetic field as

$$\tau = \mathbf{M} \times \mathbf{B} \tag{2.5}$$

Despite the impressive demonstrations in the area of magnetic soft actuators, there are still challenges to be overcome to approach the use of such systems in real applications. These are related to:

- Complex dynamics when the actuators are driven at high speeds. Soft actuators do not excel necessarily due to their high-speed properties, several damping and non-linear mechanisms make their operation at high frequencies a challenge [125]. Particularly for magnetic soft actuators, there is a lack of description of the dynamic modes happening

at high speeds. Such instabilities should be accounted for by some type of feedback mechanism.

- The lack of mechanically compatible magnetic feedback systems that allow for a seamless reporting of their actuation state. Since the actuation of such systems is done via magnetic fields, the sensing units have to be able to measure the relevant magnetic field parameters to asses the correct operation of such systems. One possible direction is the implementation of mechanically imperceptible flexible systems that can be directly laminated on the surface of the soft actuators without losing their characteristic mechanical properties [97]. Nevertheless, flexible platforms that are straightforward to fabricate and have a low contribution of mechanical signals into their magnetic sensing signal are missing.

In this work, it will emphasize the use of magnetic soft actuators that are obtained from different types of elastomers and shape memory polymers. Their dynamic motion and possible applications will be evaluated. Special focus will be given to their integration with flexible control units that allow for registration of their actuation going towards the development of fully flexible mechatronic systems.

3 Materials and methods

3.1 Printing sensors and interconnects

3.1.1 Printed interconnects

The resistance and magnetoresistance effects of printed magnetic field sensors were addressed using a 4-point layout. It consists of 4 parallel contacts with a defined pitch from 0.1 to 10 mm. The contact layout is defined using custom-designed vinyl foil (Oracal 751) shadow masks produced using a plotter cutter (Silhouette Portrait). The high stickiness of the foil is reduced by attaching and peeling the vinyl foil with a cloth 10 times, this ensures an easy peel-off after the printing of contacts. After attaching the vinyl foil to the target substrate, conductive Ag paste is painted over the stencil mask. The printed interconnects are dried for 5 min at room temperature before electrical measurements.

3.1.2 Preparation of magnetoresistive flakes

Si/SiO_2 4-inch wafers spin-coated with a sacrificial layer of AZ1505 photoresist (Microchemicals GmbH, Germany) were used to fabricate AMR flakes from thin film [Ta (5 nm)/Py (100 nm)] deposition. Using a sputtering deposition rate of 0.14 nm s^{-1} and 0.18 nm s^{-1} for Ta and Py, respectively. The deposition was conducted with a base pressure of 1×10^{-7} mbar and Ar sputter pressure of 9×10^{-4} mbar. Flakes were obtained after dissolving the AZ1505 sacrificial layer in a US bath with acetone. The flakes were recovered with a permanent

magnet and rinsed with isopropanol 5 times. Finally, the flakes are heated at 70 °C for 1 h obtaining a dry powder.

The procedure to obtain GMR flakes is identical but using 5 × 5 cm^2 glass substrates. This was to avoid the inhomogeneities on the edge of 4-inch substrates. Multilayer stacks of [Py (1.5 nm)/Cu (2.3 nm)]$_{30}$ coupled at the second antiferromagnetic maximum were sputtered. The deposition was conducted with a base pressure of 1 × 10^{-7} mbar and Ar sputter pressure of 1 × 10^{-3} mbar. The following flakes' obtention and drying were identical to that of AMR flakes.

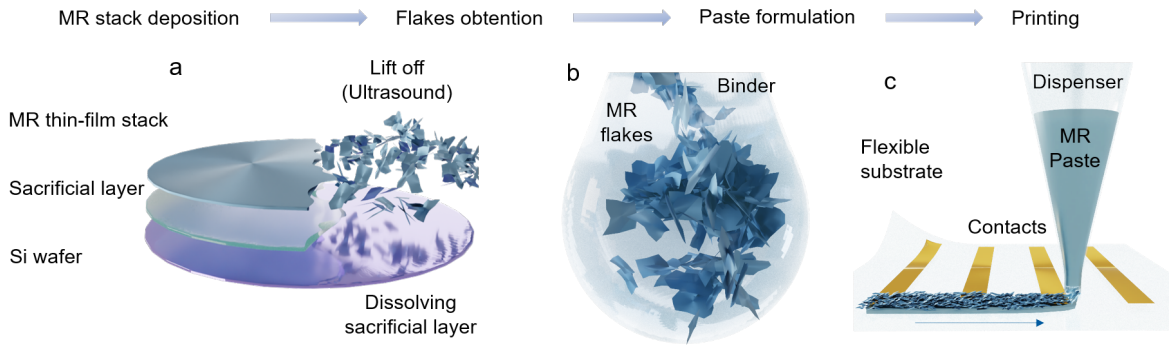

Figure 3.1: Fabrication process of printed MR sensors. a) Process starts with the thin film deposition of a material showing MR on a Si wafer with a sacrificial layer. The wafer is submerged in a suitable solvent to dissolve the sacrificial layer. Flakes are created using ultrasound during the removal of the sacrificial layer. b) Fakes recovered with a magnet are embedded in a non-conductive polymeric binder material to produce a printable paste. c) A flexible foil with contact traces is used as a substrate to print the MR paste.

3.1.3 Formulation and printing of stretchable MR pastes

Stretchable pastes were obtained using SBS block copolymer (Sigma-Aldrich, Germany). Known for having rubber-like physical properties at room temperature. The SBS pellets were dissolved for 24 h with constant stirring in Xylol (0.15 g mL^{-1}). This solution was used as a binder of the MR flakes. A total of 50 mg of dried powder of flakes was added per each mL of SBS binder. The paste is mixed using a stirring stick inside the container manually or using a vortex device at 2500 rpm. The obtained paste was painted or printed using stencils to define the desired geometry and left dried at room temperature for 2 h.

3.1.4 Formulation and dispenser printing of LMR sensors

LMR sensors are based on bismuth (Bi) 2-µm-size particles (Hainess & Maassen GmbH). The paste was obtained after adding the specific weight concentration of Bi particles (from 82

to 90 wt%) in a butylmethacrylate-type binder using a speedmixer (DAC 15oSP, Hauschild GmbH und Co. KG, Germany). Afterward, the homogeneous dispersion of particles is ensured by using a three-roll mill (S50, Exakt Advanced Technologies GmbH, Germany). The produced paste was dispensed (VC1100 dispenser, VIEWEG GmbH, Germany) into the desired substrate using a screw valve (DV-5005DFS, VIEWEG GmbH, Germany). The printed structures are then dried in a nitrogen atmosphere for 30 min at 80 °C (FT6060, Heraeus GmbH, Germany).

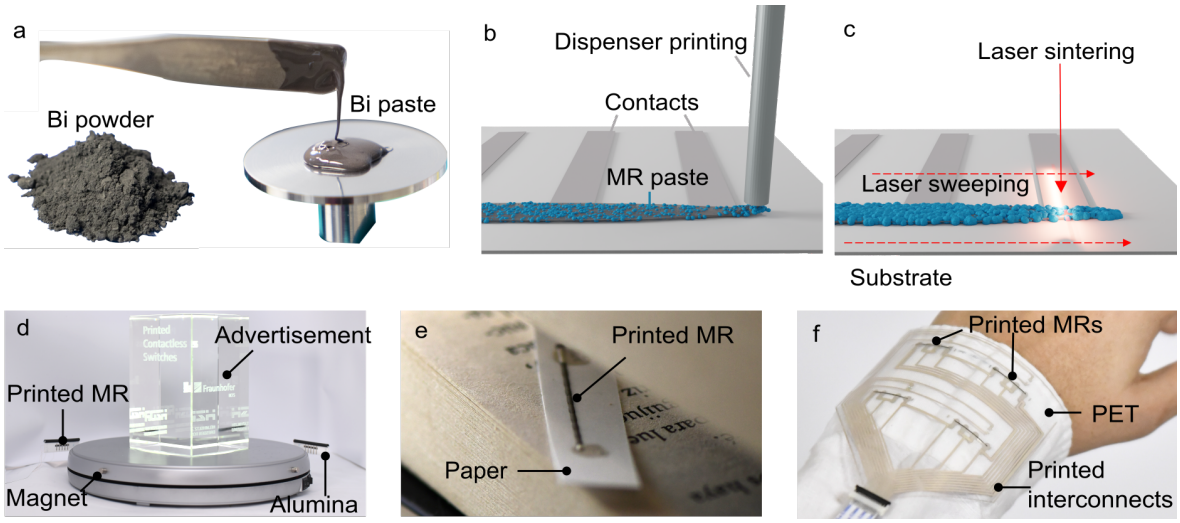

Figure 3.2: Dispenser printing of Bi-based LMR magnetic field sensors. a) Bi powder is used as filler to create a LMR magnetosensitive paste. b) The paste is dispenser printed onto a substrate and c) laser sintered to achieve conductive sensing elements. The method is highly versatile and can be used to print on d) ceramic (alumina), e) paper, and f) polymeric (PET) substrates, making it suitable for various applications such as smart-advertisements, -books, and -clothes. ([126], used under CC BY 4.0)

3.1.5 Laser sintering of LMR sensors

The printed Bi paste has to be sintered to achieve a conductive state. This was done using a LIMO900 Line Laser (FocusLight/LIMO GmbH, Germany) in air conditions. The system uses a microscopically optimized high-power diode laser array that produces a laser beam ($\lambda = 980$ nm) with a tophat profile (30×0.1 mm^2). The organic phase is removed and the particles sintered during the sweeping of the laser through the printed structures with laser fluence in the range of 10 to 100 J cm^{-2}.

3.1.6 Encapsulation of printed LMR sensors

Encapsulated sensors can increase their resilience to bending. Printed LMR sensors were encapsulated using a 10 vol% polyvinyl alcohol (PVA) solution in deionized water. The solution

was dispensed over the sensing area and baked for 1 h at 70 °C. This strategy effectively moves the maximum stress surface away from the sensing layers towards the polymer PVA encapsulation layer.

3.1.7 Reforming of printed LMR sensors

A sensor connected in a 4-point configuration was tested for the resilience of the LMR response to heat treatments to 130 °C. By using a hotplate and a infrared (IR) camera, the temperature changes on the sensor were followed during the thermal treatment. When printed in thermoplastic substrates such as PET, sensors can be treated thermally to acquire a 3-dimensional shape. After checking the viability of the procedure using the magnetoresistance characterization described in Section 3.3.1, the sensors were reformed. A reforming mold was 3D printed using the stereolithography method (Form 3, Formlabs, United States). The mold was designed to contain a curved section to place the bent sensor and fixed it in place during the thermal reforming treatment. A temperature of 130 °C was sufficient to thermoform the PET substrate without deforming the resin 3D printed mold. After 30 min in an oven with atmospheric conditions, the sensor was removed from the mold and a reformed shape was obtained with a self-standing curved geometry in a relaxed state. After the reforming treatment, the LMR response was checked again using magnetotransport characterization (Section 3.3.1).

3.1.8 Printing and self-healing of MR sensors

Sensors that are able to heal via their magnetic interactions are produced by a combination of a self-healable polymer with magnetically soft particles. The self-healing composite is obtained using a PDMS framework containing a polyborosiloxane (PBS) self-healing polymer. 0.1 g of 10:1 PDMS solution (184 silicone elastomer, Sigma Aldrich, Germany) is combined with 0.9 g of a second solution of hydroxyl-terminated PDMS with 50 mg of boric acid (Sigma Aldrich, Germany). The solution is further dissolved with 4 mL of a 1:1 mixture solvent of n-hexane and isopropanol (Sigma Aldrich, Germany) to enable an easy dispersion of the magnetic fillers in the viscous solution. By adding a volume concentration of 36.5% of permalloy (Py) fillers inside the self-healing polymer is possible to reproducibly enable the attraction between sections of a damaged sensor after applying a maximum alternating magnetic field (AMF) of 130 mT at 50 Hz with an electromagnet. The sensors are printed

on a desired substrate containing the electrical contacts to asses the resistance and magnetoresistance response after drying for 1 h at 80 °C. After deliberate damage of the sensor using a scalpel, the sensor is placed on the surface of the electromagnet connected to a 220 V_{AC} supply to promote healing via magnetic fields. The healing is confirmed by the recovery of the conductive state and the magnetoresistance is checked using the method described in section 3.3.1.

3.1.9 Printing of transparent MR sensors

FeNi nanowires were prepared using an electrodeposition growth strategy using anodic aluminum oxide (AAO) templates. The average pore size in the AAO was 60 nm and 100 µm diameter and length, respectively. After preparing the electrode via sputtering of a Cr(20 nm)/Au(50 nm) bilayer, a solution of $NiCl_2$ (0.4 mol L^{-1}), $FeCl_2$ (0.1 mol L^{-1}), and H_3BO_3 (0.1 mol L^{-1}) was used for the electrodeposition of FeNi nanowires. After electrodeposition, the template was removed using phosphoric acid solution (0.5 mol L^{-1}). The nanowires were recovered after an ultrasonic bath in isopropanol. Nanowires dispersed in the isopropanol solution were dispensed over a target surface with conductive contacts to print transparent magnetic field sensors. This process was done over a permanent NdFeB magnet with a surface field of 200 mT for achieving proper alignment and percolation of the nanowires. Nanowires were treated using a weak acid solution (0.5 g $L^{-1)}$ for 10 s to remove the surface oxidation layer. The sensors were then encapsulated using PDMS to prevent oxidation of the material in ambient conditions.

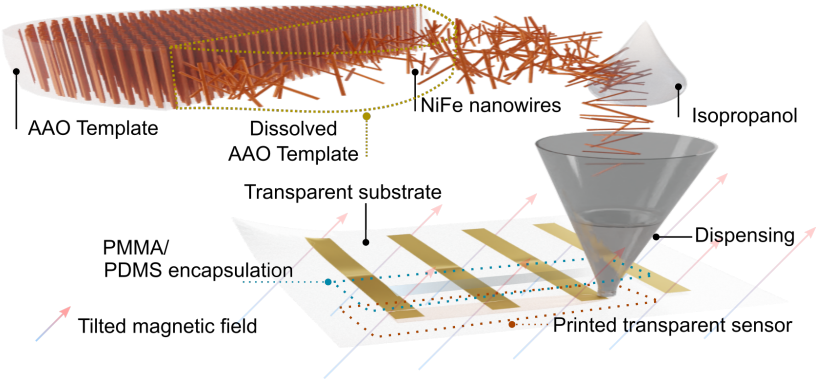

Figure 3.3: Printing of transparent magnetic field sensors. NiFe nanowires are electrodeposited in AAO templates. After dissolving the template in a phosphoric acid solution, the nanowires are resuspended in isopropanol to produce a dispensable solution. During drying, an external magnetic field aligns the nanowires to obtain conductive and transparent magnetic field sensors.

3.1.10 3D printing of MI sensors using L-PBF

The fabrication of 3D printed magnetic field sensors is achieved by means of laser powder bed fusion (L-PBF) technique (AM400, Renishaw, UK) which incorporates a Yb:YAG laser module that promotes the fusion of Invar 36 powders (D_{50} = 52.7 µm, Thyssenkrupp Materials Trading GmbH, Germany). Invar has excellent mechanical stability upon temperature changes and has a high magnetic permeability, suiting it for the 3D printing of magnetosensitive structures. The manufacturing of highly dense (99.5%) Invar36 pieces is achieved by using an exposure time of 100 µs, hatch distance of 110 µm, and volumetric energy density of 94.7 J mm^{-3}. With this is possible to print Hall-bar structures used to measure the magnetoimpedance effect magnetoimpedance (MI) of the samples with using the method described in Section 3.3.1 but varying the frequencies from 750 Hz to 8000 Hz to asses the frequency-dependent sensing of the 3D printed structures.

3.2 Thin film sensors and interconnects

3.2.1 Flexible substrate preparation in PDMS coated carrier suibstrate

The fabrication of flexible substrates for lithographic patterning requires the stabilization of the foils in rigid carriers for processing. Unless otherwise specified, I employed 5 × 5 cm^2 glass slides with spin-coated with PDMS (1:10 curing agent to base ratio) (184 silicone elastomer, Sigma Aldrich, Germany). The PDMS layer is spin coated at 1000 rpm and baked for 2 h at 80 °C. The good adhesion of the PDMS with the thin polymer foils through Van der Waals interactions results in a highly stable platform to process the flexible foils during the complete lithographic and sputtering deposition process. The typical foils employed in this work are Mylar (2.5 µm, 7 µm, Chemplex Industries, USA) and PET (125 µm, Melinex ST 504, Puetz GmbH + Co, Germany) substrates. After placing the flexible substrates on top of the PDMS-coated carrier, the samples are vacuum treated (0.1 mbar, 3 cycles to atmospheric pressure) to remove bubbles in the interface between the polymers.

3.2.2 Thin film interconnects

Substrates prepared using the method described in Section 3.2.1 are employed as a base for the lithographic pattern of Au contacts. The substrates with laminated flexible foil are spin-coated with Ti-Prime adhesion promoter at 3000 rpm for 30 s and baked at 120 °C for 2 min. Then, the AZ5214e image reversal photoresist is spin coated on top at 4000 rpm for 30 s and baked for 1 min at 110 °C. The coated sample is exposed using a direct laser writing machine (DWL 66, Heidelberg Instruments) with the desired layout containing equidistant contact pads. After exposure, the sample is reverse baked at 120 °C for 2 min and then exposed with a 365 nm UV lamp (ProMa, Proma Systro) for 30 s for flood exposure. The sample is then developed using AZ351B developer diluted in deionized water with 1:4 ratio. Samples are then dried with nitrogen gas. Samples still mounted in the carrier substrate with PDMS are placed for sputtering deposition of the Au contacts. Samples are deposited using a 5 nm adhesion layer of Cr and 50 nm of Au (1×10^{-8} mbar base pressure, 8×10^{-4} mbar Ar deposition pressure. The deposited samples are lifted off in an acetone bath without ultrasound (only short pulses, if needed) to avoid the delamination of the patterned structures.

3.2.3 AHE sensors fabrication

The fabrication of AHE sensors is done via sputtering of a bilayer of Co and Pt films on Mylar ultrathin substrates. The Mylar (2.5 µm, Chemplex Industries, USA), is prepared into a PDMS carrier as described in Section 3.2.1. The samples are then lithographically patterned using the procedure described in Section 3.2.2 for the image reversal AZ351B photoresist. The deposition of 1 nm to 4 nm Co and 1 nm Pt layers is done via Ar sputtering at 1×10^{-8} mbar base pressure, 8×10^{-4} mbar Ar deposition pressure at 2 Å s^{-1}. The lift-off of the samples is carried out using an acetone bath without ultrasound.

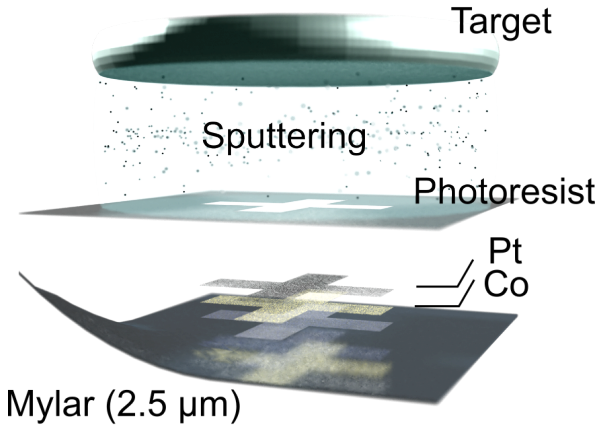

Figure 3.4: Fabrication of ultrathin flexible AHE sensors. Sensors fabricating via sputtering deposition are prepared on ultrathin Mylar foil (2.5 µm). After the lithographic pattern using direct laser writing of the AZ5214e photoresist, a bilayer of Co and Pt is deposited.

3.3 Electrical characterization

3.3.1 Magnetoresistance characterization

Different types of sensors with magnetoresistive and Hall effect responses were characterized in this work. For magnetoresistance characterization, the sensors were connected using 4 point configuration selecting the appropriate alternating current (AC) output current (0.1 to 10 mA) using a Tensormeter (HZDR Innovation GmbH, Germany). During the resistance measurement, a computer-controlled field is applied to the sensor by electromagnet coils to check the magnetoresistance response MR. Unless otherwise stated, the magnetoresistance response is calculated as

$$MR = 100\% \times \frac{R(H) - R(H_{sat})}{R(H_{sat})}, \tag{3.1}$$

for H_{sat} as field saturation, and H as the current field value. From the MR profile of the sensor, the derivative of the MR response (without % transformation) is calculated as the derivative of the MR with the magnetic field:

$$S = \frac{d(MR)}{dH}. \tag{3.2}$$

The sensor characterization of printed LMR sensors was done at higher magnetic fields and lower temperatures. For this reason, we employed a Hall measurement system (775, Lakeshore - W, United States) having a superconducting magnet supply (625, Lakeshore,

United States) able to apply fields in the range from 0 to 7 T and test the sensors down to 5 K via a He temperature controller (340, Lakeshore, United States). Since the sensors do not show saturation, the magnetoresistance, in this case, is calculated using

$$MR = 100\% \times \frac{R(H) - R(H_0)}{R(H_0)}, \tag{3.3}$$

with $R(H_0)$ the resistance at fixed temperature when there is no applied magnetic field.

3.3.2 Hall characterization

Samples with a Hall cross geometry are measured using a ZOH switching current strategy [127]. This strategy helps to remove artifacts from the Hall signal related to strain and inhomogeneous geometrical features [127, 128]. The strategy consists of switching the current direction that feeds the Hall element in two perpendicular directions. The Hall resistance measured in each of the directions is averaged to provide the transversal component of the ZOH resistance as

$$R_{ZOH} = \frac{R_{Hall1} + R_{Hall2}}{2}. \tag{3.4}$$

The switching of the contacts is done using a Tensormeter (HZDR Innovation GmbH, Germany) using ZOH analysis with a minimum switching speed of 50 ms. Accordingly, the sensitivity of Hall effect sensors was calculated as the derivative of the Hall resistance with respect to the field changes as

$$S = \frac{d(R_{ZOH})}{dH}. \tag{3.5}$$

3.3.3 SOT characterization

AHE samples showing strong spin-orbit torque (SOT) characteristics were analyzed using transport measurents. Thin film sensors fabricated using [Co(<1.5 nm)/Pt(1 nm)] bilayers are characterized using a Tensormeter (HZDR Innovation GmbH, Germany). The first and second harmonic Hall resistance signals are measured after applying a 500 mT IP with respect to the sample plane. The sample is slightly tilted to avoid random switching of the sample to an angle of < 5 °. Then the measurement is performed with the field applied close to the in-plane direction of the sample following the ZOH measurement strategy described in Section 3.3.2.

3.3.4 Noise characterization for resolution determination

The resistance level (and the Hall resistance level) in time is measured during a defined timelapse (typically 30 s) with a Tensormeter (HZDR Innovation GmbH, Germany). Using a fast integration time (typically 10 ms) and performing an fast Fourier transform (FFT) algorithm, the noise spectral density is obtained using a dedicated Wolfram Mathematika script. The maximum resolution ρ_{max} is then extracted using the noise level n_f at the frequency where white noise f_c is achieved as

$$\rho_{max} = n_f \times \frac{\sqrt{f_c}}{S_{max}}, \tag{3.6}$$

with S_{max} the maximum sensitivity level obtained from the sensor.

3.3.5 Magnetoresistance during static bending

Flexible sensors can be laminated onto substrates with different curvatures, so we tested the magnetoresistance response using fixed bending conditions. The magnetoresistance of flexible magnetic field sensors was measured using a sliding holder that deform the test sample at the midpoint creating a convex configuration. The holder contains two mobile jaws that move linearly against each other. The sensor attached to each of the sides of the jaws is bent when they get closer. The radius of the bent sample is checked using an image from the side view of the sensor. When the bending radius was defined, the magnetotransport characterization is done according to the description in Section 3.3.1.

3.3.6 Magnetoresistance during cyclic bending

Flexible samples could be bent several times during their lifetime, in order to check the resilience to many deformations we perform cyclic bending tests. A sample is attached to a Phenom XL Tensile Tester (MT10821, Thermo Fisher Scientific, United States) that contains mobile jaws that programmatically open and close at defined positions. After placing a sample in the holder and selecting the maximum and minimum opening distance, the machine is commanded to move between the selected positions for a defined number of cycles. If needed, a magnetic field is applied by placing a permanent magnet close to the sensor area. The applied field is then measured using a Gaussmeter to estimate the average field during the cyclic bending test.

3.3.7 Magnetoresistance during static stretching

Stretchable samples can have significant deformations and elongations, so we tested the magnetoresistance of samples in different static stretching states. A printed sensor is mounted on a 100% pre-stretched VHB tape using a dedicated system of clamps and pulleys. By removing the tension in the pulleys, the VHB tape and hence the sample is relaxed to the 0% strain state. During the relaxation process, an OOP buckling process occurs enabling the stretchability of the sample. By fixing the tension of the pulleys between 0% and 100% strain, the sensor can be measured using the magnetotransport characterization described in Section 3.3.1.

3.3.8 Hall effect measurements during static bending

Flexible sensors showing AHE were tested during bending mechanical deformations. Using a 3D printed holder with moving jaws, the sensor laminated into a PET foil was fixed at different bending radii. At each selected bending radius the Hall characterization of the sample was obtained as described in Section 3.3.2. After measuring with the ZOH method, the sample was also measured using the conventional Hall configuration in order to assess the differences in the measurement mode.

3.3.9 Hall effect measurements during cyclic bending

Similar to the printed MR sensors, the AHE sensors were bent for several cycles to check their performance during continuous deformations. A Phenom XL Tensile Tester (MT10821, Thermo Fisher Scientific, United States) was used to programmatically bend a flexible AHE sensor. The jaws move at a speed of 2 mm min^{-1} to bend the sample between 10 and 15 mm radius for 600 cycles. During the cyclic bending test, the conventional and ZOH resistance are tracked to assess their differences. A field of 50 mT is applied to the sensor during the cyclic bending test.

3.3.10 Hall effect measurements during non-deterministic bending

Studying the sensing capabilities of AHE sensors when subjected to non-deterministic deformations is a useful approach to emulate situations closer to reality. When the sensors are laminated into mechanically moving systems like actuators or the skin of the user, different deformations can occur that are not preestablished. We used ZOH measurements to remove the non-predictable deformations of a sensor mounted on the palm of a user. The AHE sensor fabricated on Mylar (Section 3.2.3) was mounted using body cream onto the skin of the user. The sensor was connected to a Tensormeter (HZDR Innovation GmbH, Germany) via 50 µm-thick Cu wires attached with Ag paste. The sensor placed close to a crease of the palm is repeatedly bent after closing the palm of the user. This deforms the sensor and the corresponding changes in the conventional Hall effect measurements are observed. After approaching a permanent magnet (NdFeB, spherical 5 mm radius) to the sensor, the changes in conventional and ZOH signals were also registered.

3.4 Magnetic soft actuators

3.4.1 Magnetic soft actuators based on PDMS-NdFeB particles

Permanently magnetized particles will experience magnetic torques and actuation upon external magnetic fields. The synchronized actuation of magnetic particles inside a flexible matrix causes the bending of the system responding to actuation fields. A mixture containing 70 wt% magnetic NdFeB microparticles (MQP-15-7, Magnequench) in PDMS 1:10 curing agent to base ratio (184 silicone elastomer, Sigma Aldrich, Germany) is degassed with a mechanical pump from 1 to 4 h. 4 h degassing was observed to generate void free composites that remove possible defects during fabrication. 5×5 cm^2 glass substrates with a sacrificial PVA layer are prepared via spin coating (1000 rpm, 30 s) and baking (80 °C, 1 h) as temporary carrier substrates. On top of the PVA sacrificial layer, the PDMS mixtures with magnetic particles are spin-coated at 1000 rpm for 30 s and baked for 2 h at 70 °C. The cured sample is magnetized using a 2.3 T OOP magnetic field produced by electromagnetic coils (EM2, Magness Corp.). By dissolving the sacrificial PVA layer in deionized water, an easy peel-off of the magnetic membrane was possible. The samples were rinsed in deionized water 5 times to remove the remanent traces of PVA on the surface of the polymer. The obtained magnetic membranes were cut to the desired geometry by scalpel, die cutting, or plotter cutter

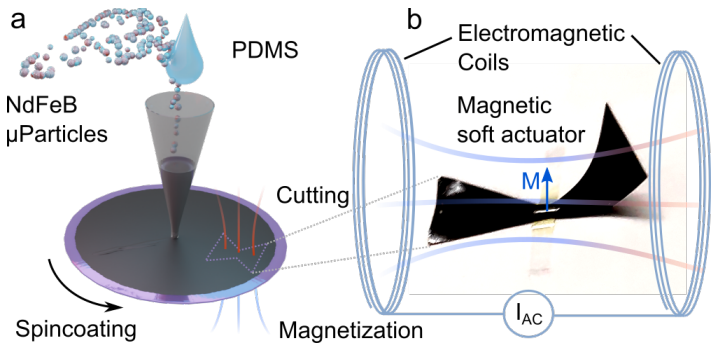

Figure 3.5: Fabrication of magnetic actuators using PDMS matrix. a) NdFeB microparticles are mixed with PDMS, and the solution is then spin-coated into a substrate with a sacrificial PVA layer for easy peeling of the membrane with deionized water. After magnetizing the samples and cutting them to the desired geometry, they can be used as a magnetic actuator or flexible permanent magnet. b) Out-of-plane magnetized samples are able to perform a clapping-like motion when placed in between electromagnetic coils that can be driven with DC or AC currents.

(Silhouette Portrait, Silhouette America Inc.). The actuation of these magnetic membranes is done using an electrically controlled coil pair (Lehrmittel Corp., Germany) with a coil diameter of 115 mm and coil thickness of 35 mm (4.5 mH, and 1 Ω_{DC}). An alternating voltage signal feeding a power amplifier system (KEPCO BOP 20–10 M, United States) drives the generation of AMF for the robot actuation. This system can generate fields up to 10 mT in the expected actuation frequency regimes (0.1 to 1000 Hz). Important to note that these permanently magnetized membranes were also employed as magnetic skins that nicely conform to the skin of users substituting the use of bulky permanent magnets.

3.4.2 Magnetic soft actuators based on DiaPLEX-NdFeB particles

Magnetic soft actuators deform upon the application of an external magnetic field, but this deformation typically disappears after the removal of the applied field. In order to fix the actuation state of magnetic membranes, we employed shape memory polymer (SMP) matrix (DiAPLEX, MM5520, SMP Technologies) with embedded NdFeB microparticles (MQP-15-7, Magnequench) [129]. The content of magnetic particles inside the polymer matrix varied between 10 and 80 wt% and was mixed using a vortex device. The obtained mixture is poured into a glass container and baked for 1 h at 70 °C. After cooling down, the obtained films are magnetized in the OOP direction using a 2.3 T field produced by electromagnets (EM2, Magness Corp.). The thickness of the membranes is controlled through the volume added to the glass container (1 to 16 mL) obtaining films from 25 to 300 μm. The actuation of the obtained magnetic foils is obtained after temporary local heating of a selected area followed by the application of an actuating external magnetic field (35 mT, ITS-MS-7040-12VDC,

Intertec Components, Germany). Local heating is achieved using a visible light lamp (SRAM HXP-R120 W 45C VIS, 2800 lm, integrated 350–720 nm bandpass filter, Leistungselektronik JENA GmbH, Germany). The NdFeB particles act as photoabsorption elements heating the sample via the photothermal effect. The system acts as a photothermally and magnetically driven soft actuator that can be tetherless actuated via radiation and magnetic fields. Given the SMP properties of DiAPLEX, the system recovers the original flat layout after heating the actuator in the absence of magnetic fields. Moreover, the sensor can hold the actuation state in case the light is turned off before the removal of the magnetic field, in such a way it cools down on the actuated state and holds it until another heating cycle occurs.

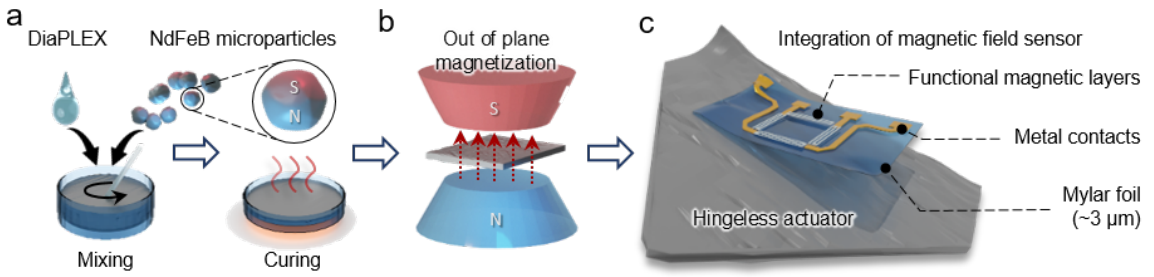

Figure 3.6: Fabrication of magnetic actuators using SMP matrix. a) NdFeB microparticles are embedded in a SMP matrix (DiAPLEX). The mixture is then poured into a glass dish and baked at 70 °C for 1 h for curing. b) The obtained membrane can be magnetized in the OOP direction at 2.3 T using electromagnets. The magnetic membrane based on SMP is able to actuate to magnetic fields only after local heating of the area to be actuated. c) Such a platform can be used as a reconfigurable actuator that can be controlled through a laminated magnetic field sensor on top of the magnetic membrane. ([10], used under CC BY 4.0)

3.4.3 Magnetic soft actuators based on Irogran-Fe(chained) particles

Actuators having chained magnetically soft fillers have been proven effective to create a lifting motion upon alignment with an external magnetic field. For the fabrication of an easily processable flexible magnetic composite with rapid curing at room temperature, we used an Irogran (PS 455-203, Huntsman Corporation) binder dissolved in tetrahydrofuran (THF Emplura, Sigma Aldrich). This mixture can be cured at room temperature for 1 h so it is not needed to place an electromagnet coil in close proximity to a heating device. Adding 10 wt% of Fe microparticles (D_{50} = 4.2 µm, JCF2-2, MMPs, Jilin Jien Nickel Industry) via vigorous stirring to the Irogran mixture creates the base for the soft actuators. The mixture is let dry in an appropriate container placed in between two electromagnetic coils that generated a magnetic field (10 mT) parallel to the IP direction of the sample. During the drying, the particles inside the composite align in the direction of the applied field creating a system with chained magnetic particles. After 1 h of continuous exposure to the magnetic field in

ambient conditions the composite is solidified and cut to the desired actuator geometry. The actuator is fixed from one edge and left a free actuation edge in between an electromagnet pair that generates a horizontal (with respect to ground) magnetic field in the range of 0 to 700 mT creating lifting angles up to 85°.

3.5 Materials characterization

3.5.1 SEM

SEM micrographs were acquired using a Phenom XL Desktop SEM (Thermo Fischer Scientific, United States). A large proportion of the samples characterized in this work are fabricated into flexible polymers that are not conductive, for this reason, it was important to select the appropriate setting parameters to avoid excessive charging of the samples. This was done by typically selecting 5 kV acceleration voltages and a low vacuum of 60 Pa. The images were acquired using the secondary electrons detector of the Phenom XL desktop scanning electron microscopy (SEM). Samples were mounted using carbon tape to fix the viewing angle as top or lateral visualizations depending on the expected features of the samples. A Phenom XL Tensile Tester (MT10821, Thermo Fisher Scientific, United States) was employed to perform in situ SEM characterization during different bending events, if necessary.

3.5.2 Optical miscrocopy

Optical microscopy of the samples was done using an optical microscope (Olympus BX-51) using the brightfield reflected light mode. Especially relevant during the lithographic processes to check the development, undercut, and lift-off of the processed samples.

3.5.3 Contact angle

For printed materials, the interaction between the binder solution and the target substrates became relevant to obtain good coverage of the surface. For this purpose, I analyzed the contact angle of the binder with the target substrate by using a drop-shape analyzer (DSA 25, Kruess, Germany). The tangential calculation module from the ADVANCE (Kruess, Germany) software permits the estimation of the contact angle of 7 µL droplets. The same system was

used to perform a manual peeling test of selected binders gluing a 5 × 30 mm^2 polyethylene terephthalate (PET) probe. By using the continuous acquisition mode of the ADVANCE software, a series of images during the detachment of the PET probe was registered. By qualitatively checking the elongation behavior of the binder during the peeling test, it was possible to identify the suitability for stretchable applications of SBS-based pastes against polyepichlorohydrin (PCH)-based pastes.

3.5.4 Magnetic fields characterization

The produced magnetic fields by electromagnets, coils, permanent magnets, and magnetic composites used in this work were characterized using a Gaussmeter (HGM09s, MAGSYS, Germany). This consists of a Hall probe that detects the out-of-plane component of the tested magnetic fields. Whenever necessary, the probe was mounted into a micromanipulator (Thorlabs, United States) to map the magnetic field down to 500 µm distance steps. By changing the orientation of the Hall probe, the full profile of the components of the magnetic field could be measured.

3.6 Demonstrators

3.6.1 Lamination of flexible sensors into target surfaces

The sensors shown in this work were employed for different application scenarios that illustrate the potential use of these systems for HMI, safety, communication, feedback control, and actuation capabilities. In such cases, the sensors have to be conformally placed into a desired target surface for their implementation. This is typically done by means of a water-soluble PVA adhesion layer between the sensor flexible substrate and the target surface. After use, the sensor can be delaminated by adding deionized water to the PVA gluing layer. In the case of sensors fabricated on Mylar foils dedicated for on-skin applications, they are attached using body cream or protective jelly (Vaseline, United States) that allows for temporary attachment of the sensors to the skin of the user. Additionally, sensors laminated on PDMS substrates and actuators can be readily attached through Van der Waals interactions without the need for an additional adhesive layer.

3.6.2 Human-Machine Interfaces

The application scenarios of magnetic field sensors interacting with digital objects were achieved via NI Labview software (National Instruments, United States). The magnetic field signals were acquired using either a data acquisition systems (DAQ) (USB 6211, National Instruments, United States) or a Tensormeter (HZDR Innovation GmbH, Germany). By interfacing the sensors with 50 µm-thick wires attached using Ag paste, the sensors can be powered and read. Typical currents were in the range of 0.1 to 10 mA. The resistance and Hall resistance signals were registered using the data logger implemented in the custom build Virtual Instruments. The sensors responding to magnetic fields were used as inputs for commanding a programmed response through the USER32.DLL libraries that manipulate the events occurring in a Microsoft Windows interface. Using the commands keybd_event and mouse_event was possible to use the sensors as peripheral input devices. Whenever needed, additional conditioning electronics were added between the sensor and the DAQ as described in Section 4.17.

4 Printing magnetic field sensors

4.1 Overview

Normally designed to comply with deformable systems, stretchable electronics have been developed to create strain, pressure, humidity, light, and bio- sensors [130–132]. In addition to the aforementioned examples, magnetic stretchable sensors fabricated using thin film techniques were also developed in the last decade [97, 133]. These were proven useful human-machine interfaces that were mechanically imperceptible when laminated even directly into the skin of the users. Having a light yet functional on-skin device sensitive to magnetic fields is a way to increase the perception capabilities of humans, in a way, the users now can interact with magnetic fields that were previously elusive to their senses [96]. Among these developments, we noted that there were no examples of a stretchable printed material with magnetic field sensing capabilities. A printable and stretchable magnetosensitive material may sum to the advantages of magnetic electronic skins by providing an easy way of fabrication. Here, I will show the obtention of magnetically sensitive pastes based on 2D particles showing AMR and GMR effects.

The findings presented in Section 4.2 have been published in the following articles [9, 134]. The results highlighted in this manuscript summarize my contributions to these publications, with additional data from the papers needed for the comprehension of this study. The electronics interface and sensor preparation for the GMR on skin demonstration were conducted by Dr. M. Ha, Dr. G.S. Cañón Bermúdez, and Dr. Y. Zabila.

4.2 Printed stretchable magnetic field sensors

Different approaches to fabricating solution-processable magnetic field sensors have been previously reported. For example, zero dimensional (0D) Co nanoparticles (NPs) in gel-like matrices fillers showed high MR amplitude at the expense of high noise [70]. 1D GMR nanowires and chained Ag-coated magnetite particles were also reported as magnetic field sensors based on magnetoresistive fillers [71, 76]. The main challenge for the previous examples was having a well-conducting stable material. Significant advances were obtained after employing magnetically sensitive 2D structures, using them was possible to obtain magnetic field-sensitive composites with improved stability. Flakes consisting of GMR multilayers were proven to work in different matrix binders printed on paper, and polymeric substrates [16, 77, 135]. This opened the opportunity to combine the high-resolution deposition needed to obtain GMR thin films and the easy printing of solution-processable pastes. Despite previous efforts in this area, we observed that no printed materials have been developed specifically for use as magnetic field sensors and that are also compatible with the mechanical strain of human skin.

4.2.1 Flakes from thin films

The road to printing magnetic field sensors starts with obtaining conductive fillers that show MR properties. The approach to fabricate conductive flakes showing MR effect is shown in figure 3.1. This fabrication strategy is effective to create engineered flakes from single-layer and multilayered stacks with precise control of the thickness [135]. This strategy is particularly required for the fabrication of engineered flakes with GMR effect whose sensitivity is dependent on the thickness of the metallic and magnetic layers. The strategy consists in depositing the MR stack over a substrate with a sacrificial layer; the sacrificial layer is dissolved in ultrasound to create flakes from the deposited material (see section3.1.2 for details). The thin film is transformed into flakes by a cracking mechanism using ultrasound that seized the deposited film area when the sacrificial layer is dissolved in acetone.

Flakes obtained with this method showed a broad size distribution that is beneficial to the percolation in conductive composites. Figure 4.1a shows the classical shape of dry Py powder. Flakes tend to roll themselves in tubular geometries consistent with observations of strain formed during the deposition. The length l (longer axis) and width w (shorter axis) of these

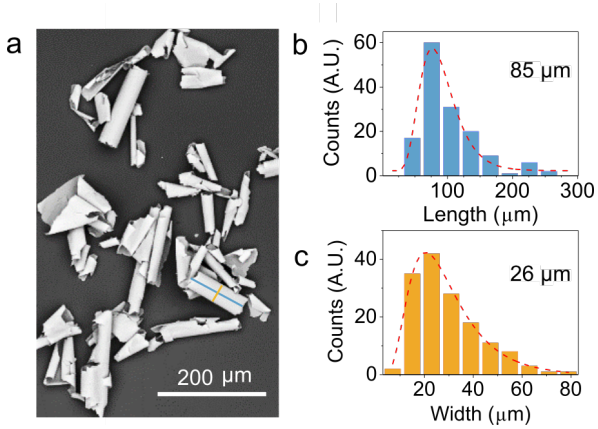

Figure 4.1: Size distribution of flakes obtained from thin film deposition. a) Dry MR flakes of 100-nm-thick Py showing a predominance of rolled-up structures. b) Size distribution of the length (top) and width (down) of the flakes. (Adapted from [134], used under CC BY 4.0)

structures were found to have a log-normal distribution with a mean length and width of $l_m = 85$ µm and $w_m = 26$ µm, respectively. Accordingly, the standard deviation of the width and length were $\sigma_l = 31$ µm and $\sigma_w = 9$ µm.

4.2.2 SBS block-copolymer as a suitable matrix for stretchable magnetic field sensors

The path to obtaining a stretchable magnetic field sensor continues with the selection of the matrix binder. Skin is a highly deformable organ that can withstand up to 100% strain deformation [136]. Examples of systems holding the percolation network above 260% were already reported in the literature [137]. The use of block-copolymers with non-covalent cross-linking showed great potential for creating resilient interconnections between particles and also good adhesion to polymer substrate like Mylar [138].

Binder-flakes and binder-substrate behavior tests confirmed the applicability of the SBS block-copolymer as an attractive binder for the MR particles. We compared the SBS block-copolymer behavior with the PCH elastomer (PCH was previously reported with the best performance as a binder for GMR printed sensors [16]).Stretchable sensors need to maintain a stable percolation even during mechanical deformations. The stability will strongly depend on the interactions between the selected binder system and the conductive fillers. We studied the binder-GMR film interaction by testing the contact angle and adhesion (Figure 4.2. SBS polymer showed a smaller contact angle with the substrate compared to PCH, 12.5°, and 41.2°, respectively. The contact angle is a signature of the surface energy and physicochemical interactions of the binder with the substrate [139]. A smaller contact angle

is a sign of better wettability, so the SBS polymer will tend to cover the surface of the MR film more. The behavior as adhesive gives another advantage to SBS based pastes, it shows dissipative adhesive behavior. Peeling tests of two surfaces glued by the selected binders showed that PCH has an abrupt removal of the peeling probe. In comparison, the SBS system forms threading behavior which is a signature of a continuous dissipation of the peeling forces between the two surfaces. Translated to the behavior as a stretchable composite, having damped changes upon mechanical perturbations provides a more stable network deformation that prevents from sudden changes in the percolation network.

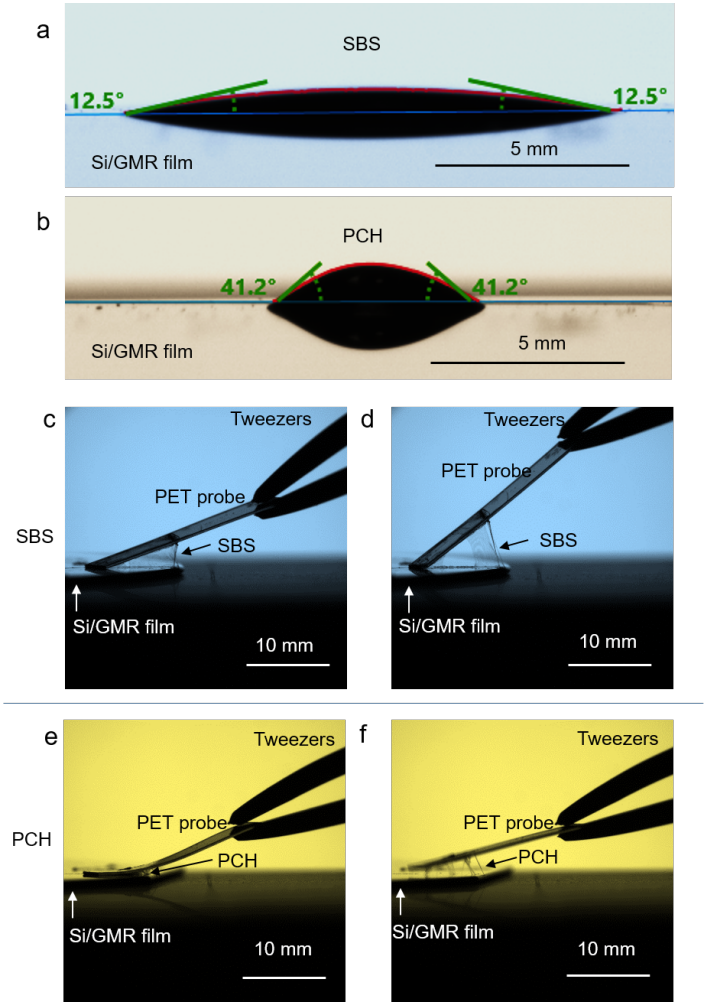

Figure 4.2: Comparison of binder interacting with MR thin films. The contact angle of a) SBS and b) PCH droplets (7 µL) on a GMR multilayer film deposited on a Si wafer. SBS shows better wettability having a smaller contact angle with the GMR surface. Peeling tests shows the dissipative behavior of SBS having a continuous deformation from c) small to d) large peeling angles. In contrast, PCH peeling tests showed that after e) peeling to a small angle, f) the peeling probe detaches suddenly from the GMR film surface. (Adapted from [9], used under CC BY 4.0)

Apart from the binder-film contact angle and adhesion tests, Figure 4.3 shows SEM micrographs that illustrate the interaction of the binder with the MR flakes. After adding a droplet of binder solution to dry particles lying on a Si substrate, we observed the

incorporation of the flakes inside the SBS volume (Figure4.3a). This was in sharp contrast to the behavior of the particles with PCH that repelled the particles to the surface of the droplet (Figure4.3b). Additionally, it was observed that particles inside the SBS binder planarized themselves and self-assembled a tight cluster inside the polymeric matrix. Even after mixing the flakes to incorporate the particles in the binder (Figure 4.3b-f there was a clear difference in the flake state in both cases. With this qualitative result, we expected to have better incorporation of the flakes inside the SBS matrix, resulting in more stable encapsulation of the flakes [140].

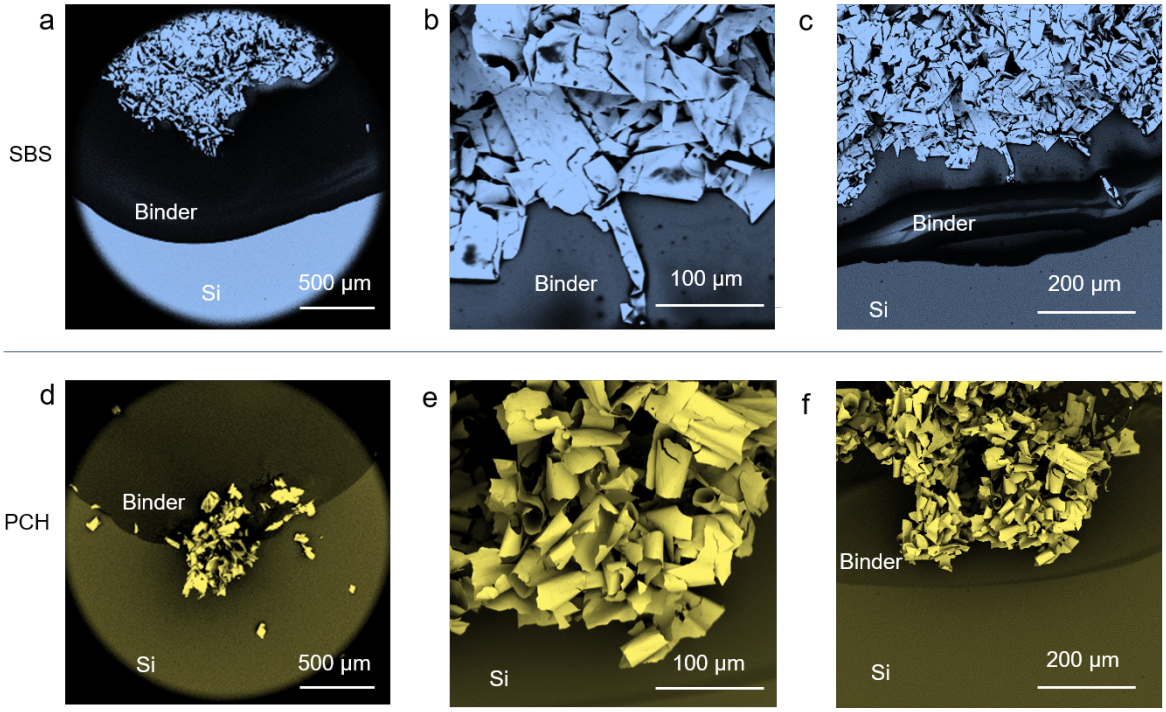

Figure 4.3: Comparison of binder-flake interaction test. SEM micrographs showing a) a self-assembled cluster of flakes formed inside an SBS droplet. b) After mechanical mixing, flakes are planarized c)inside the droplet. d) When adding a PCH droplet over dry flakes, they tend to stay outside the binder. Even after mechanical mixing e) flakes remain in their characteristic rolled shape f) inside the PCH droplet. (Adapted from [9], used under CC BY 4.0)

4.2.3 Sensing performance of printed magnetic field sensors based on flakes showing AMR effect

As described in section 2.2.1, MR effects are present in all conductive materials, but the strength of this effect is strongly dependent on the intrinsic properties of the materials. Ferromagnetic materials show AMR effect, where the interaction of the magnetization of the material with respect to the applied field plays a critical role in the transport phenomena [60]. Among ferromagnetic materials, Py thin films, are the most widely used ferromagnetic

material for sensors, this is related to its high MR effect (up to 5%) and small saturation fields (below 10 mT) [141]. Here, Py-based printed sensors were studied to revise their performance to detect magnetic fields.

Figure 4.4 shows the dependence of the AMR response with respect to the applied magnetic field $\mu_0 H$ of 100-nm-thick Py films and printed sensors. Thin film samples refer to as-deposited Si wafers with AZ1505 sacrificial layer. First, we measured the classical anisotropy of the thin film samples measured perpendicular and parallel to the current direction. When measured perpendicular to the applied current, we observed an AMR amplitude of 1.9% that saturated above 5 mT fields. The AMR amplitude is reduced to -0.3% in the parallel direction. In comparison, after processing the film samples to prepare our paste (Figure 3.1, we found that the MR effect was still in the samples with an amplitude of 0.35%. The printed sensors did not show saturation up to 400 mT. This expands more than 80 times the field range detection of Py thin film magnetic field sensors. A second feature characteristic of the printed sensors compared to the thin film case was that the sensors showed an isotropic response. When the current traveled in the parallel and perpendicular direction with respect to the magnetic field, the sensor showed identical behavior. Depending on the applications, an absolute field strength sensor might be useful independently of the direction of the field flux. The printed sensors can be useful in such scenarios because they will respond to the strength of the magnetic field independent of the direction of the magnetic field source.

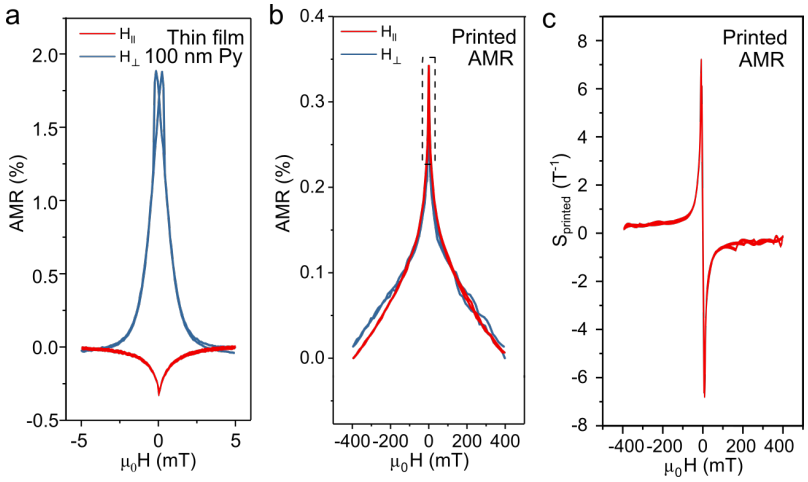

Figure 4.4: AMR response of Py thin films and printed sensors. a) Thin film 100-nm-thick Py and b) the printed sensor AMR response. Signals were recorded by applying the field in-plane and changing the angle with respect to the current direction to obtain parallel and perpendicular curves. c) Sensitivity of the printed AMR sensor response to magnetic fields. Sensors show a maximum sensitivity of 0.07 T^{-1} at 8 mT (Adapted from [134], used under CC BY 4.0).

Sensing parameters such as sensitivity, noise, and resolution, determine the range of applications suited for the printed magnetic field sensors. As described in section 2.2.2, the

field detection of current printed sensors goes from 100 μT to 1 T. Electronic platforms that provide continuous exposure to magnetic fields can have physiological effects on organisms subject to this stimulus. Considering this, the WHO has established an exposure limit to static magnetic fields of 40 mT [142]. Any attempt to use magnetic fields beyond this safety limit could have health consequences in the long term. Aimed for stretchable on-skin HMIs, sensors should be able to detect fields in the mT and better in the sub-mt range. This possibility is studied in terms of the resistance noise of the sensor and their sensitivity to the applied magnetic fields (Figure 4.5).

To understand the sensor's resolution capabilities, we went from back-of-the-envelope estimations, through graphical analysis, to noise spectral analysis. Figure 4.5a shows the variation of resistance of a printed sensor measured for 1-minute periods without applied magnetic fields. During these resistance traces, the resistance of a 25.693 Ω printed magnetoresistor had a maximum deviation of ±2 mΩ. We can start with back-of-the-envelope calculations to understand the resolution capabilities of the sensor. Assuming a deviation from the mean of $\Delta R_{mean} = 2$ mΩ and a maximum sensitivity of $S_{max} = 0.12$ T^{-1} $= 3.083$ Ω T^{-1}, the maximum resolution of the sensor should go below $\rho < \Delta R_{mean}/S_{max} = 640$ μT. This quick estimation indicated that the sensor might be useful below the mT range. Following with the graphical analysis of the resolution, changes in resistance of the sensor were tracked during 10 magnetic field cycles between 0 and 300 μT (Figure 4.5b). From graphical inspection of the 3-σ error bars, it was clear that the sensor was able to discriminate 100 μT steps. The complete estimation of the maximum resolution requires using noise spectral analysis and identifying the noise level at 1 Hz n_{1Hz} value. Using an FFT transformation of the signals shown in Figure 4.5a, we obtained the noise profile of the sensor in frequency spectra (Figure 4.5c). Accordingly, the noise showed a $f^{-1/2}$ trend with characteristic noise value of $n_{1Hz} =$ 6.1×10^{-4} Ω Hz$^{-1/2}$. Using equation 3.6, the total estimation of the maximum resolution of the sensor was $\rho_{max} = 60$ μT. This resolution is suitable for fields below the WHO safety limit, and confirmed the compatibility with on-skin HMI applications.

4.2.4 Sensing performance of printed magnetic field sensors based on flakes showing GMR effect

GMR technologies profit from the name, the *giant* changes in conductivity due to the intensity of an external magnetic field. Using GMR based flakes has demonstrated the possibility of achieving up to 37% GMR in printed sensors [16]. Despite having a significant resistance

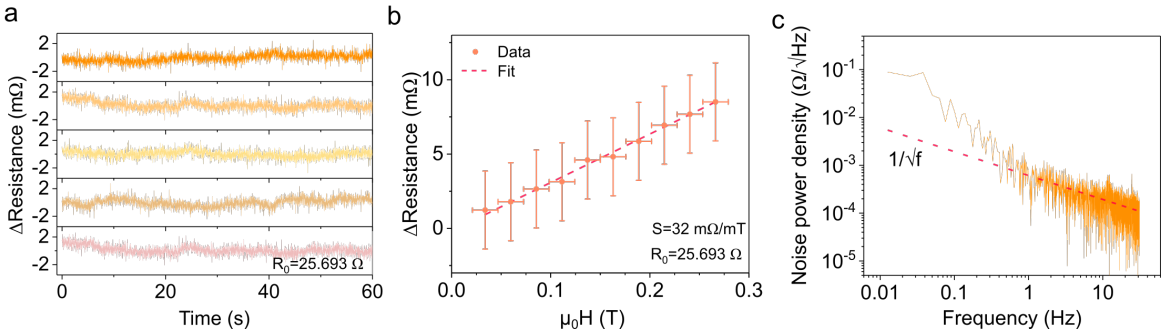

Figure 4.5: Noise analysis for the estimation of the resolution of printed AMR sensors. a) The signal in 1 minute periods of the printed sensors showed a variation of ±2 mΩ from the mean resistance $R_0 = 25.693$ Ω. b) Sweeping a small field intensity (from 0 to 300 μT) applied to the sensor, showed a variation of the resistance with respect to the R_0. Graphical analysis of the 3-σerror bars illustrates the possibility to detect field steps below 1 mT. c) The spectral analysis of the resistance traces shows that the noise density of the printed AMR sensors have a $f^{-1/2}$ tendency. Based on these parameters, a resolution of 60 μT was calculated for the AMR printed sensor (equation 3.6) (Adapted from [134], used under CC BY 4.0).

change, these examples show their maximum sensitivity above 100 mT; this is above the WHO safety threshold for static magnetic fields [142]. We needed to find a good GMR stack candidate that allowed us to sense reliably smaller magnetic fields safe for human interaction. As explained in section 2.2.2, the amplitude of the GMR effect is affected by the thickness of the deposited layers. Particularly, the thickness of metal interlayers has to be tuned to have *giant* magnetoresistance coupling [65]. Depending on the thickness, the system can show several maxima points. The first maximum is typically larger than the others but at the expense of having a stronger coupling, meaning that higher magnetic fields are needed to disturb this coupling [66]. In sensing terms, this results in lower sensitivities to small magnetic fields. For this reason, we decided to study the suitability to print magnetic field sensors based on $[Py/Cu]_{30}$ multilayer system tuned at the 2nd maximum. We expected to have a sufficiently good GMR response with maximum sensitivities below the 40 mT safety limit. For this purpose, we followed the method described in Figure 3.1 by depositing 30 bilayers of [Py(1.5 nm)/Cu(2.3 nm)] on 5 × 5 glass slides covered with an AZ1505 sacrificial layer.

As-deposited $[Py/Cu]_{30}$ thin films showed a GMR effect of 8% with the field applied along the in-plane direction, and a 0.4 % amplitude with the field passing in the out-of-plane direction with respect to the film plane (Figure 4.6). This anisotropy is expected from in-plane GMR stacks, where the switching of the magnetic layers occurs parallel to the plane of the films. for these multilayer stacks, saturation of the GMR signal was reached at 20 mT holding below the 40 mT safety threshold. In comparison, Figure 4.6b shows the 2.1% of GMR response of the printed sensors in both, the in-plane and out-of-plane magnetotransport configurations.

This is similar to our observations with the response of AMR printed sensors (see section 4.2.3), where isotropy is gained in the printed formats. A second recurrent phenomenon in the printed samples was the observation of the reduced MR amplitude and larger detection ranges. In the case of the printed GMR sensors, this change is less pronounced, showing ≈ 90% of the dynamic range at 20 mT fields. Calculation of sensitivity (Figure 4.6) confirms the suitable characteristics of the printed sensors to perform in the desired field ranges. Having a maximum sensitivity $S_{GMR} = 2.5\ T^{-1}$ at 0.9 mT, the printed GMR sensors are well suited to work below the WHO safety limit of 40 mT [142].

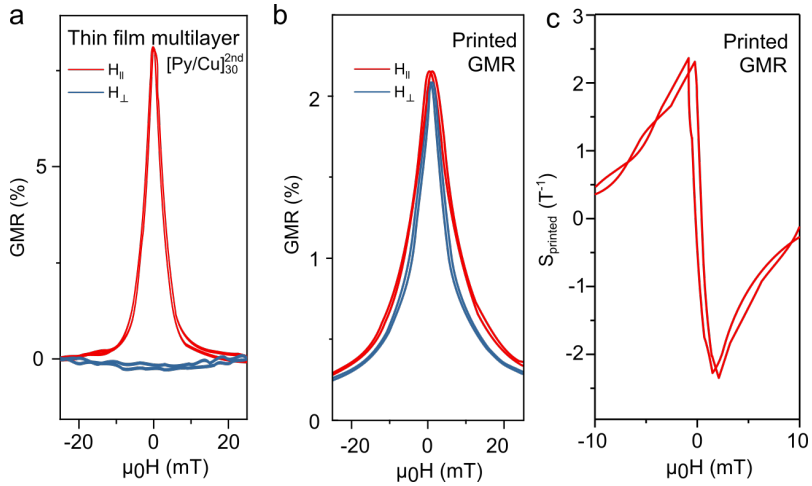

Figure 4.6: GMR response of a $[Py/Cu]_{30}$ multilayer thin film and a printed GMR sensor. a) Thin film GMR multilayer of $[Co/Cu]_{30}$ and b) corresponding printed sensor GMR response. Signals were recorded by applying the field in-plane and changing the angle with respect to the sample plane to obtain parallel and out-of-plane curves. c) Sensitivity of the printed GMR sensor response to magnetic fields. Sensors show a maximum sensitivity of 2.5 T^{-1} at 0.9 mT (Adapted from [9], used under CC BY 4.0).

4.2.5 Bending of printed magnetic field sensors

The first approach to developing flexible and eventually stretchable electronic printed elements is understanding their behavior during mechanical bending. Bending stresses are known to affect the conductivity of flexible conductive elements. In Figure 4.7, I describe the influence of bending in the printed sensing materials and their MR amplitude.

Figure 4.7a, shows a lateral view micrograph of a sensor bent (folded) to a radius $r_b = 20$ μm. The printed paste, with a thickness of ∼ 40 μm, is conformally following the Mylar foil shape without any visible delaminated areas. This observation confirms the excellent adhesion and support of the SBS block copolymer as a matrix for the MR flakes. Magnetotransport characterization of the printed AMR sensors during bending revealed a consistent response of the sensor around 0.25% down to 2 mm (Figure 4.7c). Correspondingly, the composite

paste fabricated from GMR flakes, corroborated the resilience of the printed material to micrometric folding (Figure 4.7d). This extreme bending represents a 2-order-of-magnitude enhancement with respect to previously reported magnetic field sensors.The stability of the GMR amplitude was also confirmed, from flat to even the 16 µm folded state, the sample preserved a GMR amplitude of 1.5 ± 0.1% (Figure 4.7f). Owing to the resilience to severe mechanical deformations and stability of the MR response, we confirmed the suitability of the sensor as a highly flexible magnetic field sensing printable platform.

4.2.6 Stretching of printed magnetic field sensors

Ultraportable devices, aimed to be worn on the skin of the user are expected to be more than mechanically flexible. Stretchability is another key feature to be compatible with skin mechanics. E.g. Human skin strain limit can go close up to 100% strain [136].To obtain a stretchable platform, we laminated a Mylar foil into a biaxially strained very high bonding

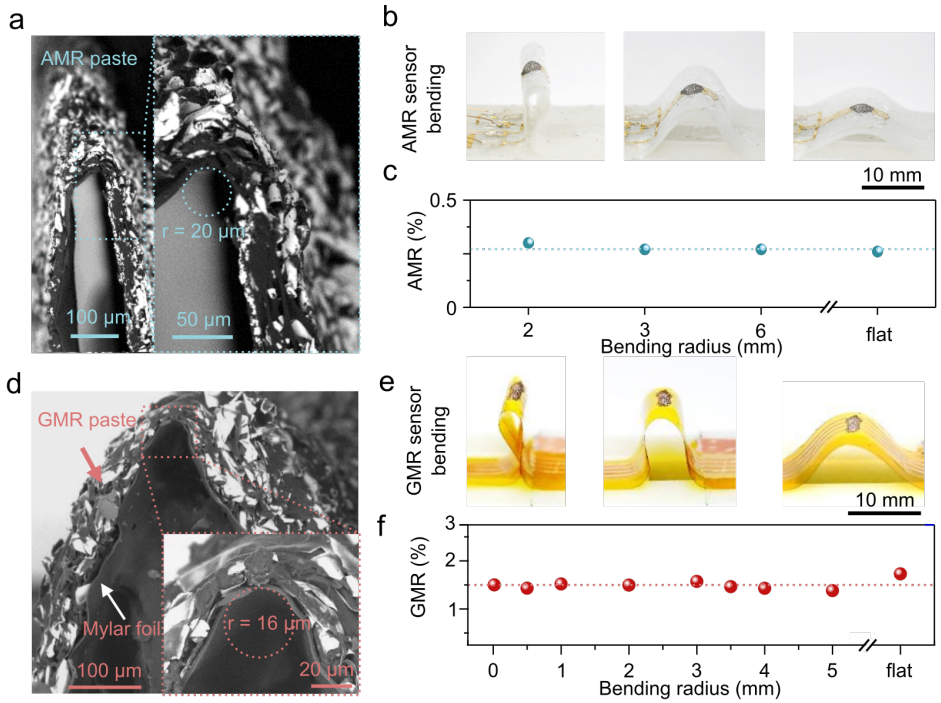

Figure 4.7: Bending performance of printed AMR and GMR sensors. a) SEM micrographs showing a folded printed AMR sensor (inset shows the detail of the bending radius r =20 µm) printed on Mylar foil. b) Photographs of a printed AMR sensor during a static bending experiment showing different bending radii. c) The AMR response of the printed sensor is stable at around 0.25% during these mechanical deformations (Adapted from [134], used under CC BY 4.0). Similarly, d) SEM micrographs showing a folded printed GMR sensor (inset shows the detail of the bending radius r =16 µm) printed on Mylar foil confirms the resilience of the paste and good adhesion to the substrate. e) Photographs of a printed GMR sensor during a static bending experiment showing different bending radii. f) The GMR response of the printed sensor is stable at around 1.5% during these mechanical deformations (Adapted from [9], used under CC BY 4.0).

tape (VHB) film (100% strain) [133]. Figure 4.8 describes the performance of the printed GMR sensors during relaxing-stretching tests.

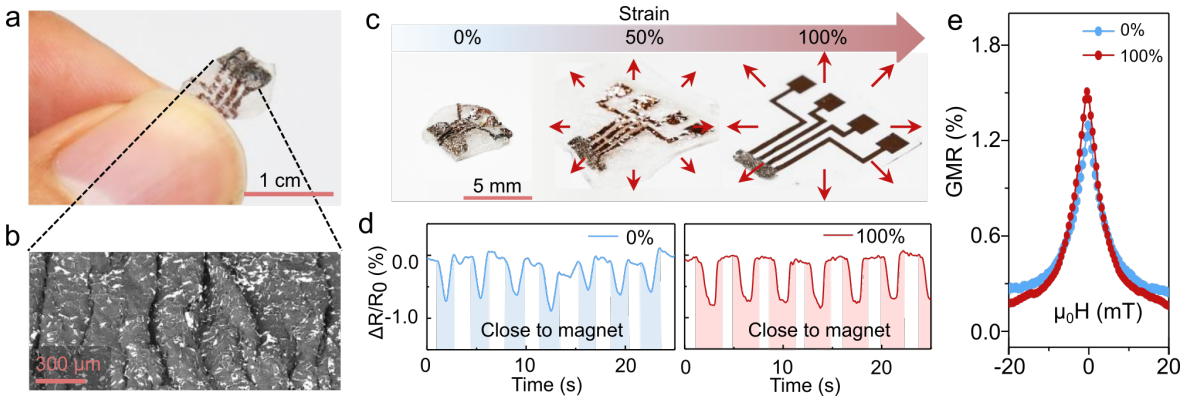

Figure 4.8: GMR response of printed sensors during stretching. a) Photograph o a magnetic field sensor printed on a pre-stretched VHB foil, b) the SEM micrographs show the topography of the out-of-plane buckling of the samples. c) The response of a 100% biaxially strained sensor, d) is checked by following the changes in resistance after approaching a permanent magnet. e) Magnetotransport characterization reveals that the sensor is functional in the relaxed (0%) and strained (100%) states showing a GMR of 1.3% and 1.5%, respectively (Adapted from [9], used under CC BY 4.0).

Figure 4.8a, shows a picture of a printed sensor after relaxing the strain of the VHB carrier film. It shows an uneven surface characteristic of an out-of-plane buckling pattern as revealed by the SEM micrograph in Figure 4.8b. An initial test of a stretched and relaxed printed sensor, consisting in approaching a permanent magnet (shadowed areas 4.8d), verified the persistence of the GMR effect showing a similar decrease in the resistance signal during the time of interaction. Magnetotransport characterization (Figure 4.8e) shows the GMR of the relaxed and stretched sensor in the region of ±20 mT. The amplitude of the GMR is 1.3% and 1.5%, accordingly. Despite having a decrement in the GMR response during this extreme deformation, the printed sensor is still functional and has a similar sensing profile compared to the fully stretched case. Confirming a resilience to 100% strain changes validates the use of this material to print magnetically sensitive materials that are mechanically compatible with the demands of human skin. It is worth noting that the sensor in the 0% strain state shows less stability with respect to the strained state. It is expected that deformation affects the sensor signal nominal resistance stability. In this regard, we developed electronic conditioning and readout mechanisms that account for mechanical instabilities being possible to detect magnetic fields under the influence of mechanical stresses. This is addressed in part in the following chapter for hall effect sensors 5 and on a submitted patent for magnetoresistive sensors [143]. Strain insensitive sensing is a current challenge of flexible electronics and continuous development of solutions will allow the development of artifact-free readout of such signals [24].

4.2.7 Printed magnetic field sensors for on-skin touchless HMIs

Over time, there is an increasing amount of machines and devices around us. Touchless human-machine interfaces could allow interaction with the physical and digital world in more efficient and seamless ways. Here, we present a simple yet illustrative possibility of interaction with a digital platform using laminated on-skin printed magnetic field sensors.

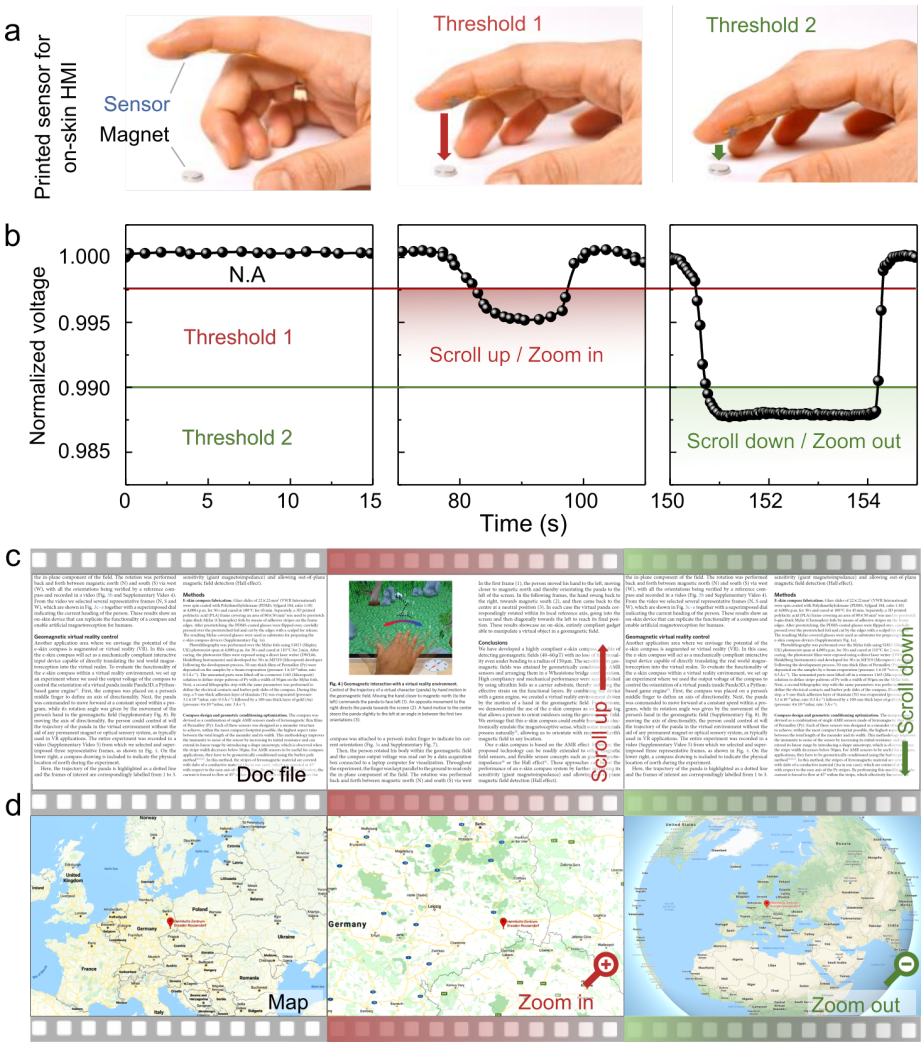

Figure 4.9: Printed GMR sensor laminated on-skin employed for a touchless HMI interface. a) A printed GMR sensor laminated on the skin of a user can be approached to a permanent magnet to detect different proximity levels. It is possible to define two different threshold levels that depend on the proximity of the finger to the magnet. b) Signal trace showing the normalized voltage. The threshold levels are defined to perform two different tasks that allow control of two applications via touchless interaction. c) First example shows scrolling through a digital document and d) the second example changes the magnification view of a digital map interface (Adapted from [9], used under CC BY 4.0).

Touchless interaction using magnetic fields is demonstrated in Figure 4.9. A printed GMR sensor is laminated on the finger of a user (Figure 4.9a). Depending on the distance between a permanent magnet and the finger, is possible to define action threshold levels for different commands (Figure 4.9b). Two examples are shown, Figure 4.9c employs the user-defined

thresholds to scroll up and scroll down through a PDF document. This is done with a single gesture and the amount of scrolling is defined by the time in the action area. This differs from the classical scrolling wheel in mouse peripherals, where the scrolling is defined for the number of repetitions or turns to the scroll wheel. In a similar way, Figure 4.9d uses proximity gestures to change the magnification on a digital map.

4.3 Printing LMR sensors towards large area and large volume applications

Arrays of magnetic field sensors distributed over broad sensing areas enable applications in magnetic imaging, biomedical sensing, or environmental monitoring applications. Such arrays are typically fabricated using MEMs fab technologies, which are limited to the size of the wafers employed. Printed magnetic field sensors stand up as an attractive alternative to reduce the complexity of sensor array fabrication. In this study, I demonstrate the fabrication of magnetic field sensors using Bi. This feedstock material has large magnetoresistance and can be readily processed as conductive filler to create printable pastes. The volume capabilities of the paste fabrication using Bi are increased by several orders of magnitude compared to the thin film flakes approach (Section 4.2.1), thus opening up opportunities to scale up the production of printed magnetic field sensors.

The findings presented in the next sections of this chapter have been published in the following article [126]. The results highlighted in this manuscript summarize my contributions to the work, with additional data from the published work needed to follow the motivation for this study. Tunning of printing and laser sintering parameters of the Bi paste was conducted by C. Voigt, Dr. S. Mosch, Dr. M. Kussnezoff, Dr. M. Fritsch, and Dr. M. Vinnichenko. Dr. Y. Zabila designed the electronics used for the readout of the MR panels. The assistance for the low-temperature magnetotransport characterization of printed Bi sensors from P. Makushko is highly appreciated.

4.3.1 Fabrication of printed sensors showing large non-saturating magnetoresistance

Bi powders (D_{50} = 2 µm) were used to formulate a paste compatible with the dispenser printing method (Figure 3.2a). The paste was dispensed over rigid or flexible substrates to define the layout of the sensing elements, which typically consists of a 4-contact configuration connected through the Bi paste (Figure 3.2b). The paste needs to be sintered using a micro-optically optimized high-power diode laser array, which rendered it conductive and enabled it to function as a magnetoresistive sensor (Figure 3.2c). The direct dispensing of the Bi paste onto ceramic, paper or polymeric substrates demonstrates the versatility of the technique in enabling the integration of magnetic field sensors into different platforms (Figure 3.2d,e,f).

4.3.2 Sensing performance of printed magnetic field sensors based on Bi powders showing LMR effect

Bismuth is an attractive material system in solid-state physics due to its different quantum and topological effects, such as large magnetoresistance, quantum oscillations, and bulk topological insulation [144]. Bi single- and polycrystals have shown large magnetoresistance effects above 100% at room temperature [59]. The results shown in Figure 4.10 reveal the magnetoresistive behavior of the Bi-based printed sensors. When printed onto an alumina substrate, the sensor exhibits a LMR effect of 64% at 2.3T (Figure 4.10a). The curve initially follows a parabolic behavior, transitioning to a quasilinear regime above 1 T. The sensitivity of the sensor showed a saturation, with a maximum sensitivity S_{max} close to 0.31 T^{-1} (Figure 4.10b). Spectral analysis of the sensor signal measured at different current sources showed that the best performance was achieved at current levels close to 1 mA (Figure 4.10c). Although noise levels were lower at 19.7 mA, we observed a non-convergent signal over long integration times due to the low-frequency noise following a f^{-1} trend. The 1.14 mA spectral profile showed a $f^{-1/2}$ trend, suggesting the possibility of integrating up to the corner frequency of 2.8 Hz and achieving a maximum resolution of ρ_{max} = 14 µT (Equation 3.6).

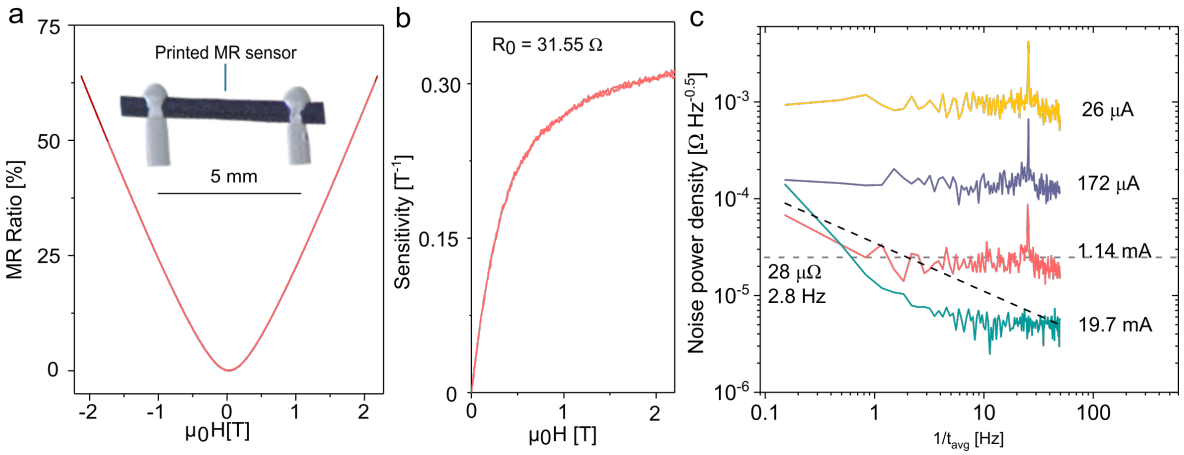

Figure 4.10: Sensing performance of printed acLMR sensors. a) Sensor printed on alumina with a contact pitch of 5 mm (inset), which exhibits a LMR effect of 64% at 2.3 T. b) The sensitivity response changes from parabolic to linear saturation. c) To determine the optimal feeding parameters, we analyzed the spectral noise for different current sources. The results showed that the best performance was achieved with a current level close to 1.14 mA for a 31.55 Ωmagnetoresistor (Adapted from [126], used under CC BY 4.0).

The high mobility and cyclotron frequencies of the charge carriers of bismuth allow for achieving quantum limits at relatively low magnetic fields. The transition from classical parabolic to linear magnetoresistance has been reported as the quantum regime transition, and we observed it in our printed samples at room and low temperatures (Figure 4.11). Figure 4.11a shows the LMR response of the sensors from 5K to 300 K (MR at room temperature is

detailed in Figure 4.11b). The printed LMR sensor showed resistance changes up to 3900% at 7 T for low temperatures, and 146% at room temperature. As observed in Figure 4.11c, the changes in resistance transition from a parabolic behavior to a quasilinear regime. This was observed by the saturation of the magnetoresistance sensitivity. In the case of room temperature measurements 4.11d, the sensitivity saturates to a 0.35 T^{-1}. The transition from parabolic to linear regimes is known as a quantum transition of the system [144]. To estimate the field where this transition occurs, we calculate the second derivative of the magnetoresistance and took the field of the full width at half maximum (FWHM) of a Gaussian fitting. This showed a transition to the quantum regime in the range of 0.3 to 0.9 T, which was consistent with previous studies of bismuth [144].

4.3.3 Bending performance

When printed on flexible foils, electronics will be subjected to mechanical deformations that might change their conductivity and sensing performance. We started to analyze the role of encapsulation to enhance the resilience to bending of the printed magnetic field sensors. When the sensor was subjected to 50 cycles of bending, it showed a drift on the base resistance of 69%. Such high changes over the long term could hinder reliability and eventually damage the printed sensors. For this reason, we used an encapsulating layer of PVA that would enhance the resilience of bending by effectively moving the region of maximum stress away from the sensor layer. During mechanical bending, it is expected that the failure points during bending stresses are located on the surface of the material. Adding an encapsulation layer moves the plane of maximum stress to the polymer which tends to resist more stresses due to its good elastic mechanical properties. This is schematized in Figure 4.12a,b. This strategy already reduces the resistance change drift aging to 5% which is 14 times lower than the non-encapsulated case (Figure 4.12d). The following bending tests for Bi printed sensors were performed using a PVA encapsulation layer.

To study the stability of the magnetoresistance response at different bending conditions we performed a static bending test (Section 3.3.5). The magnetoresistance response at different bending radii (from flat down to 3.5 mm) was recorded during the bending and the flattening back of the sample. During this step-by-step bending cycle, the magnetoresistance changes were kept stable at around 4.2%. This was the first positive hint of the stability of the response of the sensor independent of their bending state.

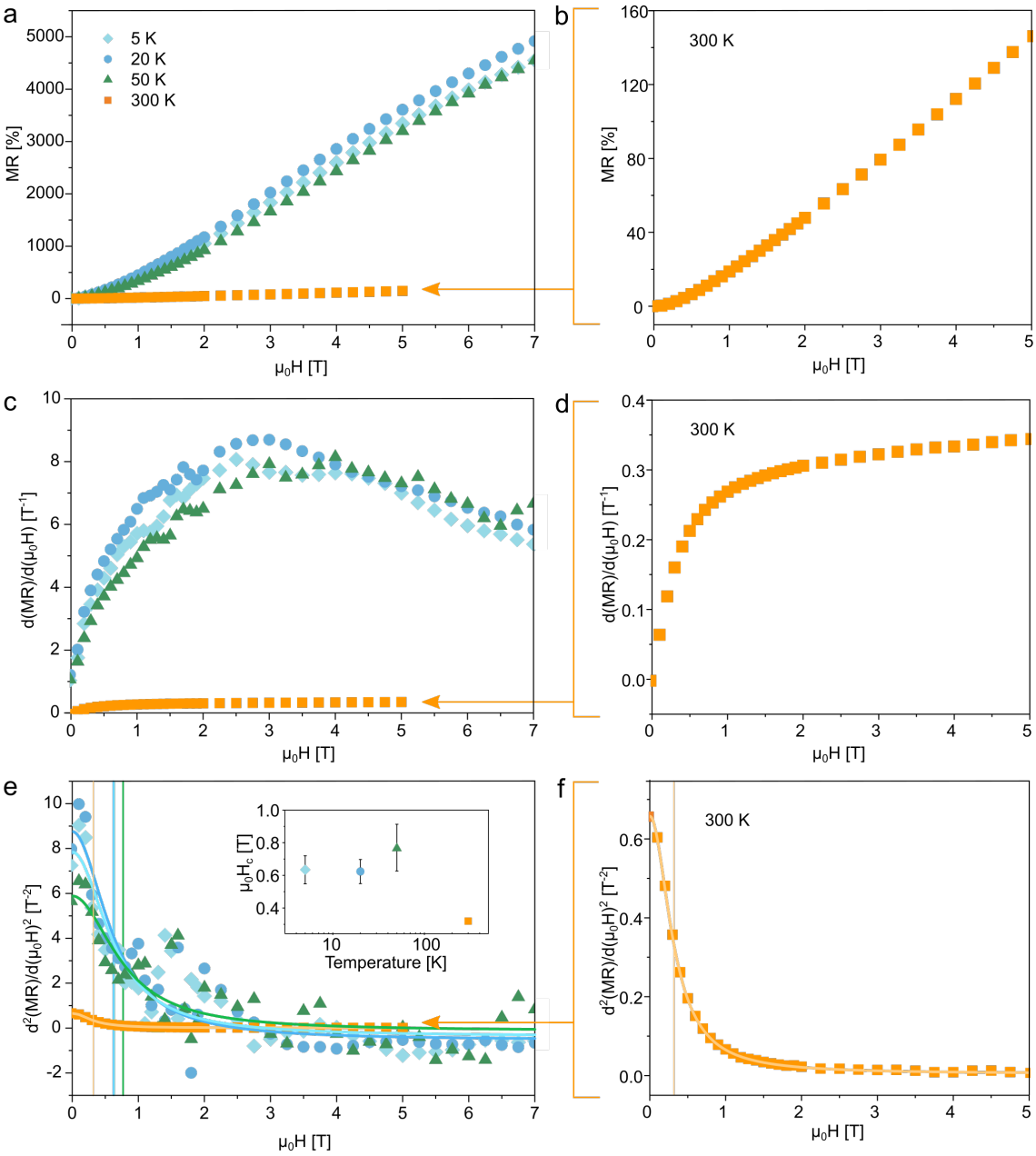

Figure 4.11: Large non-saturating magnetoresistance in bismuth printed sensors. a) Magnetoresistance response of a printed magnetic field sensor tested at low (5 K, 20 K, 50K) and room temperatures (300 K). b)Shows the detail of the magnetoresistance at room temperature. c) The first derivative of these changes with respect to the field shows the transition of the sensitivity from a parabolic to a quasilinear regime d) even at room temperatures. e) Checking the FWHM of the second derivative was useful to estimate the transition field to the quantum regime of the sensor at different temperatures. f) Shows the detail of the room temperature case (Adapted from [126], used under CC BY 4.0).

Following with the mechanical tests of encapsulated printed Bi sensors, we performed a bending cyclic test on a sample connected to a multimeter to follow their resistance changes. As observed before, the resistance of our magnetoresistive sensors can be influenced beyond magnetic contributions. The mechanical deformation of our sensors has a significant contribution to the resistance changes of the sample. Figure 4.14a shows a schematic representation of the profile of the resistance signal during a typical bending cyclic test.

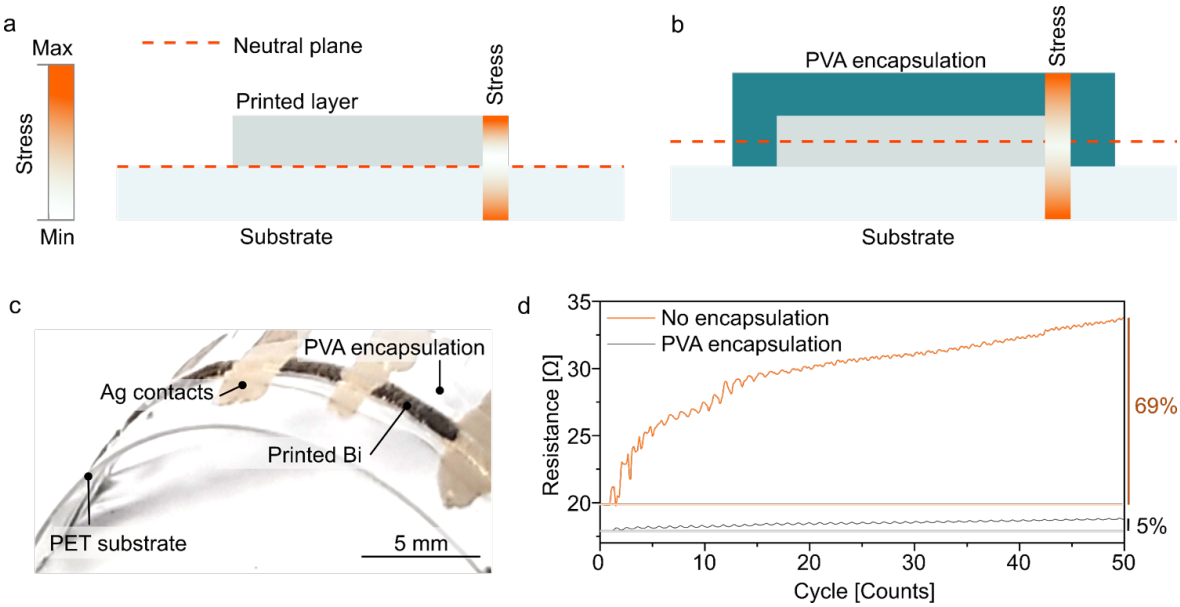

Figure 4.12: Encapsulation of printed Bi sensors to improve bending resilience. a) Schematic representation of the maximum stress located on a flexible foil during bending. The maximum stress levels are normally located at the surface of the foils during bending. The maximum stress on the system will be located on the sensor area if the sensor is not encapsulated. b) An encapsulated sensor will move the high-stress points to the encapsulated layer, effectively protecting the sensing area. c) A picture of a sensor with a PVA encapsulation layer. d) Plot showing the resistance drift due to the aging of the sensor during a cyclic bending test from a 15 to 30 mm bending radius. A sensor that is not encapsulated showed a resistance change of 69% during the initial 50 cycles. In comparison, an encapsulated sensor showed a change of 5 % increase in resistance due to these mechanical deformations (Adapted from [126], used under CC BY 4.0).

When a magnetic field is applied to the sensors, the resistance will change according to the LMR effect of the sample and the intensity of the field. Additionally, the resistance will oscillate with the frequency of mechanical cycling. These contributions to the resistance arising from the gauge and piezo effects that are dependent on the current strain of the sample during the bending test (i and ii Figure 4.14a). When the magnetoresistance effect is tested with a permanent magnet, there will be also proximity contributions that will increase

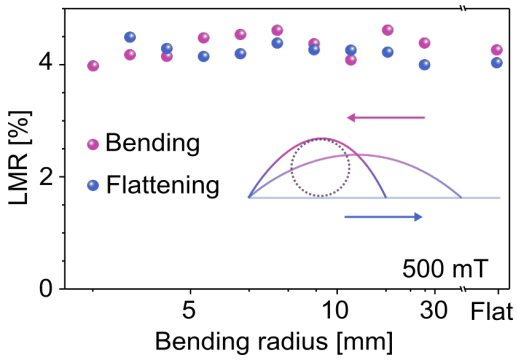

Figure 4.13: Performance of printed LMR sensors during static bending tests. An encapsulated sensor printed on PET was bent from a flat to 3.5 mm bending radius and flattened back. During this experiment, the magnetotransport characterization up to 500 mT was recorded after fixing the sample at selected bending radius. The sample showed a stable LMR response of 4.2% during the complete bending down to 3.5 mm and flattening back cycle (Adapted from [126], used under CC BY 4.0).

the amplitude of the oscillations of the resistance when the magnet is placed for several cycles during the actuation (iii and iv Figure 4.14a). Figure 4.14b, shows the real data of the sensor resistance subjected to 2300 bending cycles (bending radius from 15 mm to 30 mm). The signal shows sudden changes that correspond to the magnetoresistive response when a permanent magnet approaches the sensor. The oscillation of the resistance is also observed due to the mechanical deformation of the sample, with an additional drift contribution corresponding to the aging of the sample (<10% during 2300 cycles). By examining the amplitude of the resistance changes before and after removing the permanent magnet (350 mT average fields) (Figure 4.14c) we noticed that the changes of magnetoresistance were stable around 1.9% (Figure 4.14c). Meaning that the LMR effect of the sample is not reduced even during the wear experienced during this mechanical test. This result is prospectively useful in the case these sensors would be used for wearable applications where several mechanical deformations can occur.

4.3.4 Temperature stability

Apart from mechanical deformations, printed sensors might be subjected to other environmental and processing events with temperature changes. High temperatures in ambient conditions could affect the oxidation state of materials and possibly change their transport characteristics. For these reasons, sensors printed on alumina were tested up to 130 °C in ambient atmosphere and checked for their magnetoresistance after this heating treatment (Figure 4.15). Using thermal images to check the temperature distribution on the printed sensors, we observed that the metallic contacts and the Bi printed area have a lower temperature than the surrounding substrate and hot plate due to their high heat exchange capabilities in contact with the cold air (Figure 4.15a-d). When checking for the magnetoresistance of the sensors before and after the annealing treatment, it was observed a consistent response close to 7.5% at 500 mT in both cases.

In the current market of printed and flexible electronics, it exists several processing approaches that allow for new form factors. One of them is the in-mold electronics strategy that employs 2D printing fabrications over thermoformable substrates to reshape into desired 3D geometries. This allows for the creation of light and highly conformal functional panel consoles as needed in the automotive industry. The target temperature of the high-temperature test was suited to be compatible with the thermoforming processing of PET substrates (Section 3.1.7). We checked for the possibility of postprocessing our printed LMR

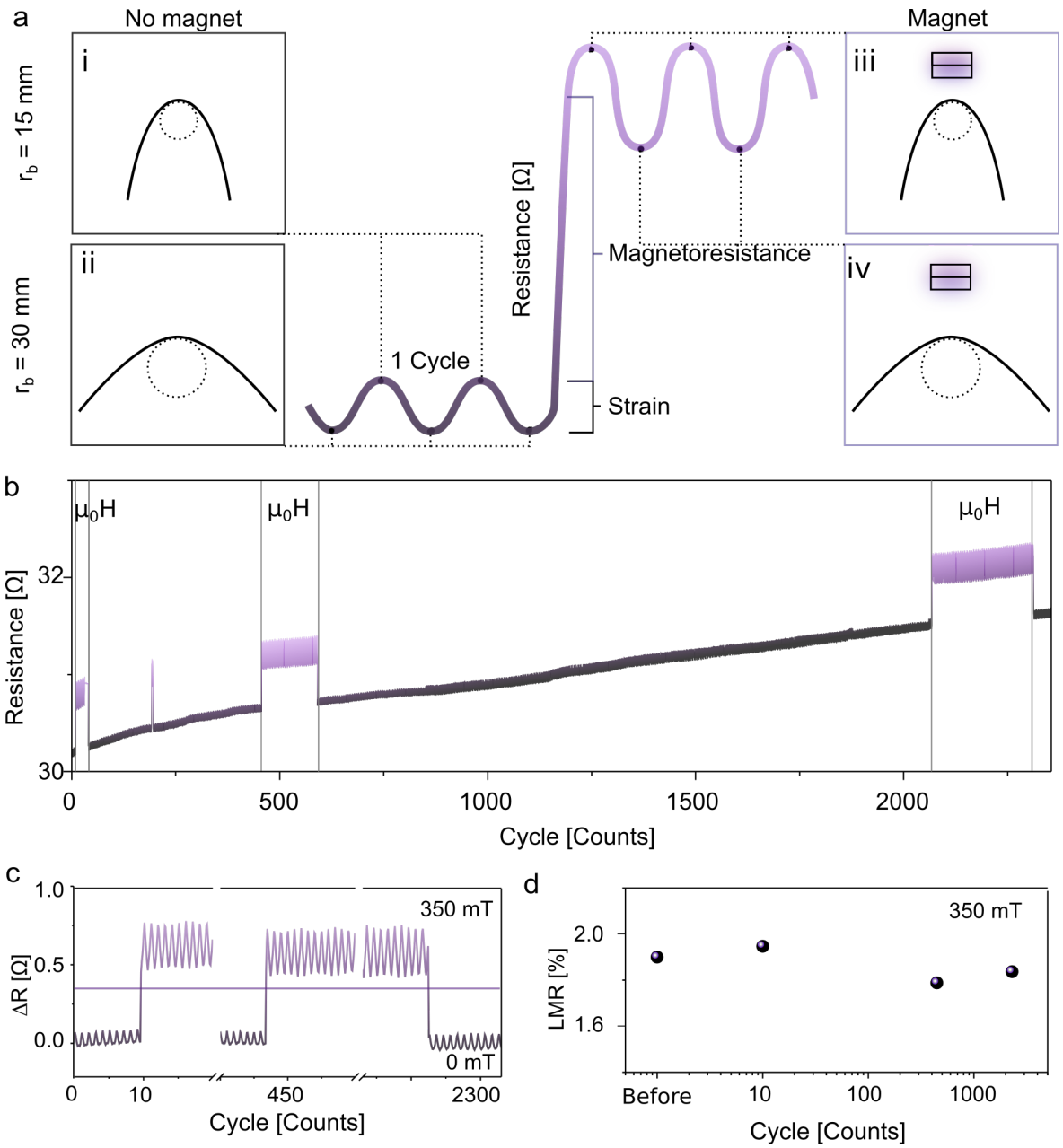

Figure 4.14: Performance of printed LMR sensors during cyclic bending tests. a) Schematic representation showing a printed LMR sensor bent from i) 15 mm to ii) 30 mm. The resistance of the sensor will oscillate with the frequency of the bending test due to gauge and piezo effects. After approaching a permanent magnet the base resistance level will increase due to the LMR effect of the printed Bi sensors. If the permanent magnet is fixed in position during several bending cycles (iii, iv), the oscillations in resistance will show a larger amplitude due to the change in the proximity to the fixed magnet. b) Resistance data of a printed LMR sensor bent during 2300 cycles and intermittently approaching a permanent magnet to check the LMR response. c) The changes in resistance just before and after approaching a permanent magnet showed that the sensors remain with d) a stable LMR response (Adapted from [126], used under CC BY 4.0).

sensors with thermoforming-like processing. An encapsulated sensor printed over a PET foil was fitted into a 3D-printed mold. The mold with the sensor was heated at 130 °C for 30 min at ambient air conditions. Comparing the magnetoresistance before and after the reforming process we observed a reduction in the magnetoresistance effect from 2.5% to 1.9% at 300 mT. Meaning that while the MR response remains on the sensor it will have a

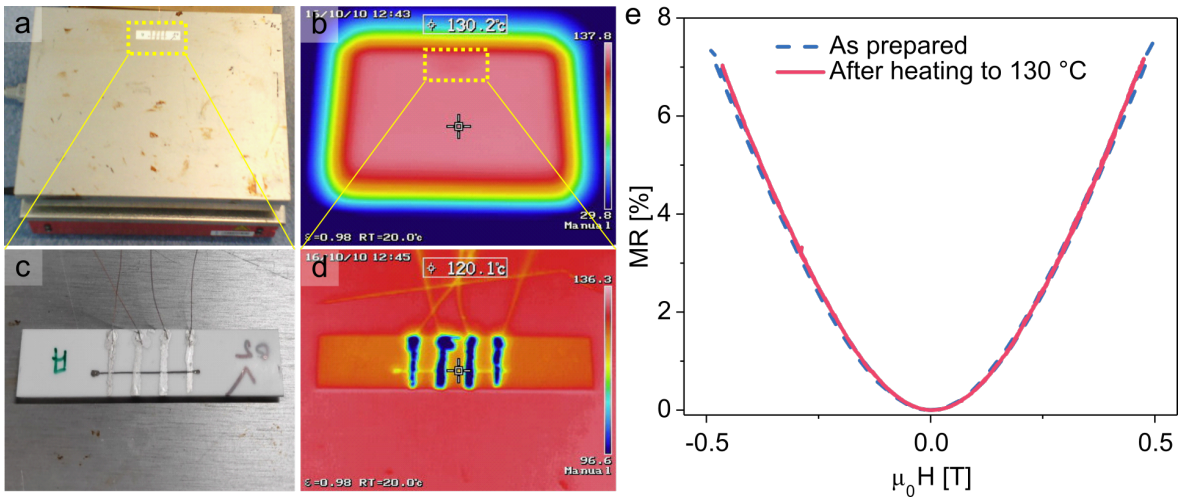

Figure 4.15: Thermal treatment of printed LMR sensors. a) A LMR sensor printed on rigid alumina substrate was heated at 130 °C in atmospheric conditions and b) checked with an infrared camera. c) The sensor area was d) checked with IR imaging to observe the distribution of the temperature observing a lower temperature (120 °C) on the printed area due to the fast exchange of heating with the air in the room. e) Magnetoresistance of the sample prior to and after the temperature treatment (Adapted from [126], used under CC BY 4.0).

slight decrease (20%) in the total MR response. Despite not being examined in this work, the reduction in the LMR effect could be related to the partial oxidation of defects created during the bending of the sample just prior to the thermoforming treatment.

4.3.5 Larger area interactivity

In Section 4.2.7 it was shown the possibility to create a printed touchless HMI that was laminated on the skin of the user. This example showed how laminating flexible magnetic field sensors onto a magnetically non-sensitive surface (like the human skin) could create new technological possibilities. Magnetic fields can travel through several common materials

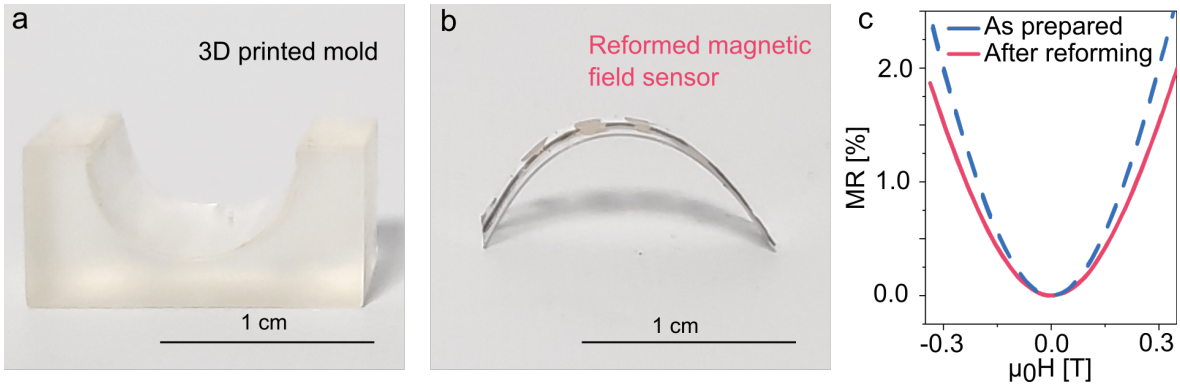

Figure 4.16: Thermoforming of printed LMR sensors. a) A 3D-printed mold having an arc structure with a radius of 5 mm is used to fit a sensor printed onto PET. b) By heating the sample for 30 min at 130 °C inside the mold, a reforming process of the substrate occurs producing a self-standing arc configuration. c) The sensor magnetoresistance was tested before and after the reforming process (Adapted from [126], used under CC BY 4.0).

without significant distortion like plastics, glass, wood, concrete, and more. This enables the possibility to extend the touchless capabilities even when the sensors are behind or inside diamagnetic and paramagnetic materials. This enables seamless interaction of laminated arrays of sensors placed over, under, or behind various objects such as walls, windows, or desks. With this principle, almost anything can be converted into an interface.

To show this concept, an array of sensors was printed on PET and laminated over different surfaces to illustrate the possible applications of interactivity over larger areas. Figure 4.17 shows the electronics design principle for such panels. As explained previously, mechanical and temperature effects can affect the readout of printed magnetoresistive elements. For such reason, different electronic conditioning approaches have been developed to stabilize the readout of resistive sensors. Wheatstone bridge configurations are known to help to stabilize temperature changes of resistive sensing elements [145]. Here, a similar approach was implemented as the electronic conditioning of the printed LMR sensors arrays (Figure 4.17a). A single line of printed Bi is sectioned into two parts by a middle contact creating two MR sections (Magnetoresistor, and Magnetoresistor'). This is used as the sensitive half of the Wheatstone bridge. Onto an external PCB are added one resistor with comparable resistance to the printed sections and a variable resistor that tunes the output voltage of the bridge. The output voltage of the bridge is connected to a voltage amplifier that works as a digital converter by amplifying any negative voltages from the bridge to "Low" values and any positive output voltage to "High" values (Figure 4.17). By tuning with the variable resistor, the bridge is left slightly unbalanced to have a negative voltage output when there is no magnetic field applied to the system. Meaning that the system is normally "Low" if no magnetic field is applied. By approaching a permanent magnet to the "Magnetoresistor" area, the balance of the bridge changes to positive voltages producing a "High" signal voltage after amplification. In the case that a magnet is approached to the "Magnetoresistor'" area, the voltage of the bridge only becomes more negative meaning that the digital signal remains without change in the "Low" level. With this behavior, only the "Magnetoresistor" area is effectively sensitive to the proximity of permanent magnets.

Using this design principle, we printed an array with 4 sensing units (Figure 4.17). 4 Bi MR lines were printed over PET substrate and connected through printed Ag contacts. The connection of the panel was done using an FFC-like connector layout that allows for easy interconnection with external electronics. The layout contained space for placing surface mounting devices (SMD) LEDs for visual reference to the user. Figure 4.17d shows the circuit

design for this implementation where all the sensors are connected in series with a common current source. Each sensing unit was connected to an operational amplifier. The amplified signals are registered through a DAQ device that is connected to a computer for the control of user-defined commands.

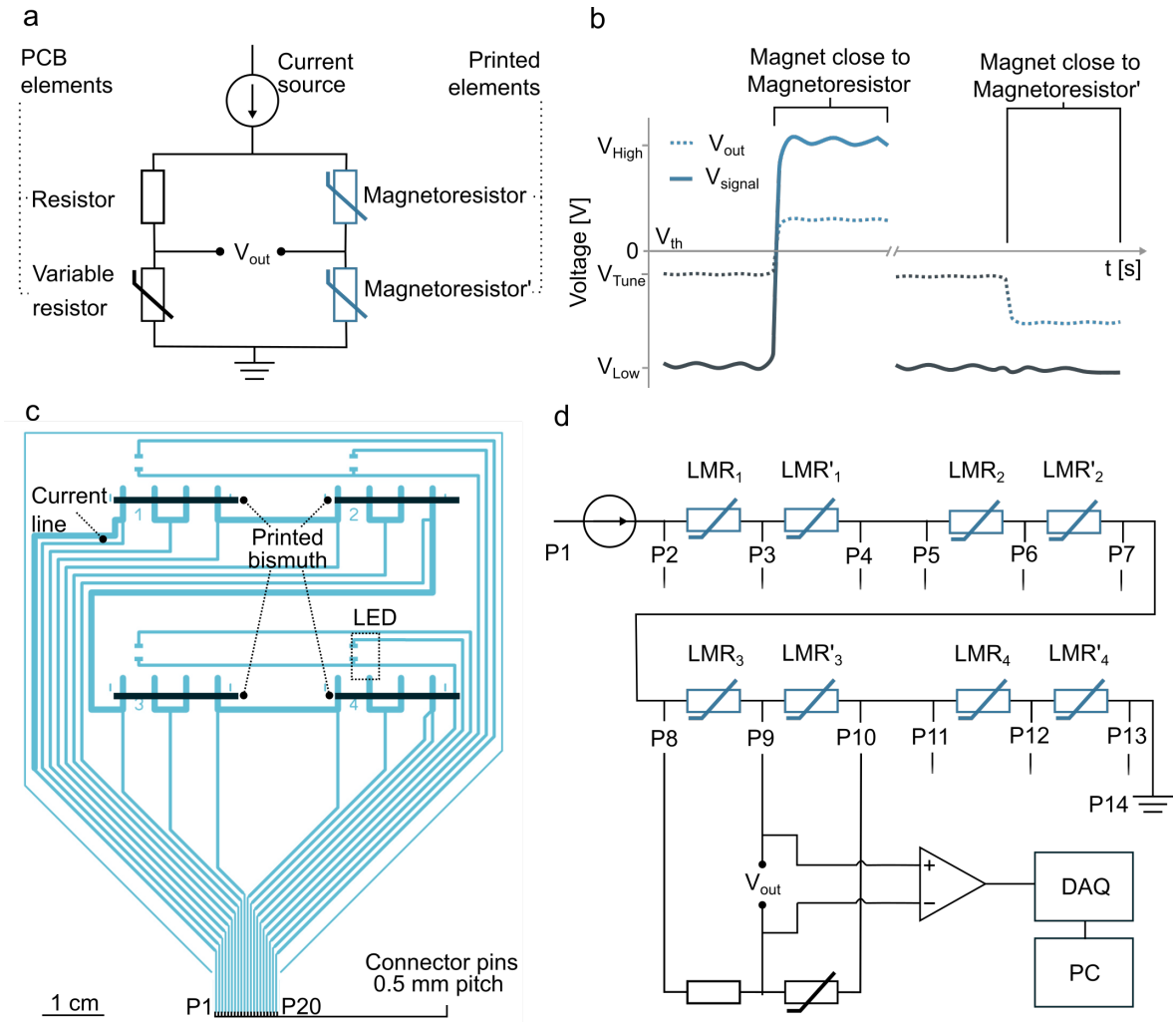

Figure 4.17: Electronics design of magnetically interactive printed panels. a) schematics of Wheatstone bridge configuration implemented with magnetoresistors for the detection of magnetic fields. It consists of two printed magnetoresistive elements balanced by resistive elements in an external PCB. The output voltage depends on the tuning of the variable resistor and the changes of resistance upon the application of magnetic fields to the printed sensors. b) Schematic representation of the digitalization of the signal produced by a Wheatstone bridge balanced towards negative voltages. The digital signal only responds to the proximity of a permanent magnet to one of the magnetoresistors, leaving to the second magnetoresistor the function of temperature stabilization. c)Layout of a printed panel with 4 Wheatstone bridge sensing units. d) Schematics of the electronic readout system of the magnetically interactive panels consisting of an array of printed sensors connected in series to a current source and connected to a computer through a DAQ system. This implementation allows for flexible programming of user-defined commands upon the proximity of a permanent magnet to the corresponding sensing area (Adapted from [126], used under CC BY 4.0).

As a first implementation example, Figure 4.18 shows the integration of the magnetically interactive printed panel into an interactive poster. In this concept, the printed panel is used to change the content displayed into a poster-like system. The printed panel is placed behind the poster screen, hiding it to avoid visual interference with the content displayed.

A projector in the front displays the content on the visible side where users will interact with the poster using a permanent magnet (Figure 4.18a). Using two of the sensing units of the panel, we defined the commands of action when a permanent magnet approached to each of these areas. In this case, we programmed the system to change the content displayed in the poster (Figure 4.18c). Panel d on Figure 4.18 shows a typical signal trace of the system. Both sensing units have a normally "Low" level until the user approaches a permanent magnet to the sensitive areas changing the signal level to "High" during the event. With the shown sequence the user changed the content of the poster from layout 1 to layout 2 (6 s timeframe) and the other way around (16 s timeframe). All the interactions with the sensing panel were remotely activated by the magnet without direct contact with the sensors that were hidden behind the projection screen.

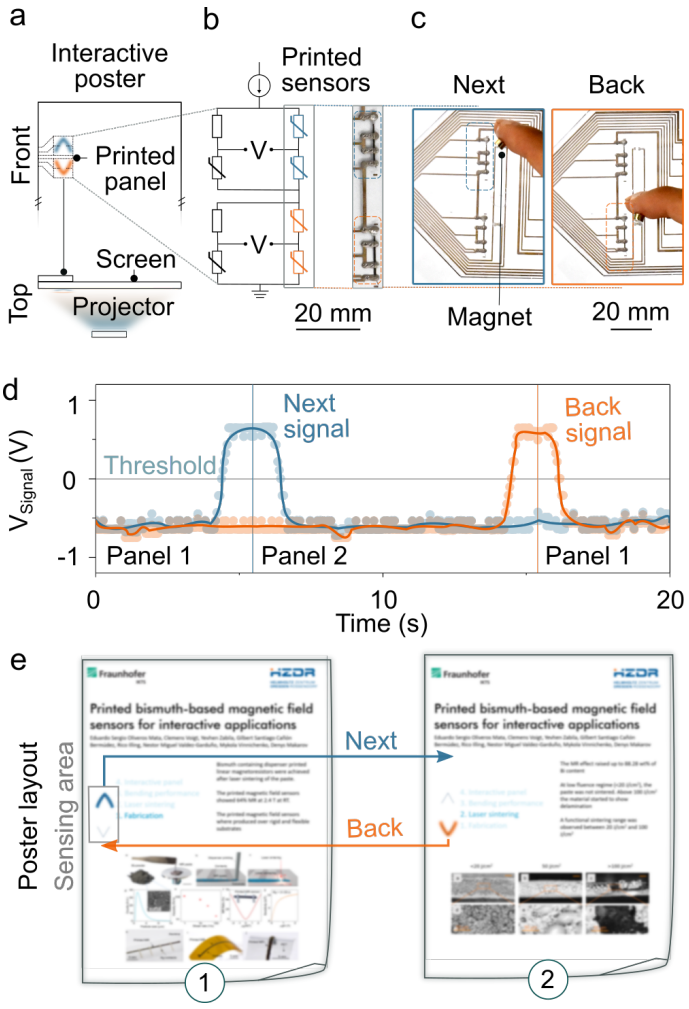

Figure 4.18: Printed magnetically interactive panels for interactive posters. a) An array of printed LMR sensors is placed behind a projector screen that acts as an interactive poster. b) Two sensing units are c) used to trigger next/back commands to change the content displayed on the poster based on the proximity of a permanent magnet from the visible side of the poster. d) Signal traces in time of the two sensing areas (Next-blue, Back-Orange) showing the activation of these areas at 6s and 16 s, correspondingly. e) The layout of the poster changes from layout 1 (left) to layout 2 right during these commands (Adapted from [126], used under CC BY 4.0).

In a similar way, the printed panel was repurposed to act as a hidden keyboard for safety applications. On-request printing of interactive units might be useful for the current trend of smart home applications, where several appliances can be connected and automatized through electronic add-ons. Figure 4.19 shows the use of the printed panel as a hidden input password keyboard. By placing the panel behind a cover on the entrance of the door of the user, it is possible to enter a password by using a permanent magnet (Figure 4.19a). Each of the sensing areas are assigned to one digit that are sequentially activated by the user that wants to enter (Figure 4.19b-d). The signal displayed in Figure 4.19e shows the sequential activation of each of the digits of a user-defined password that eventually grants access to the user.

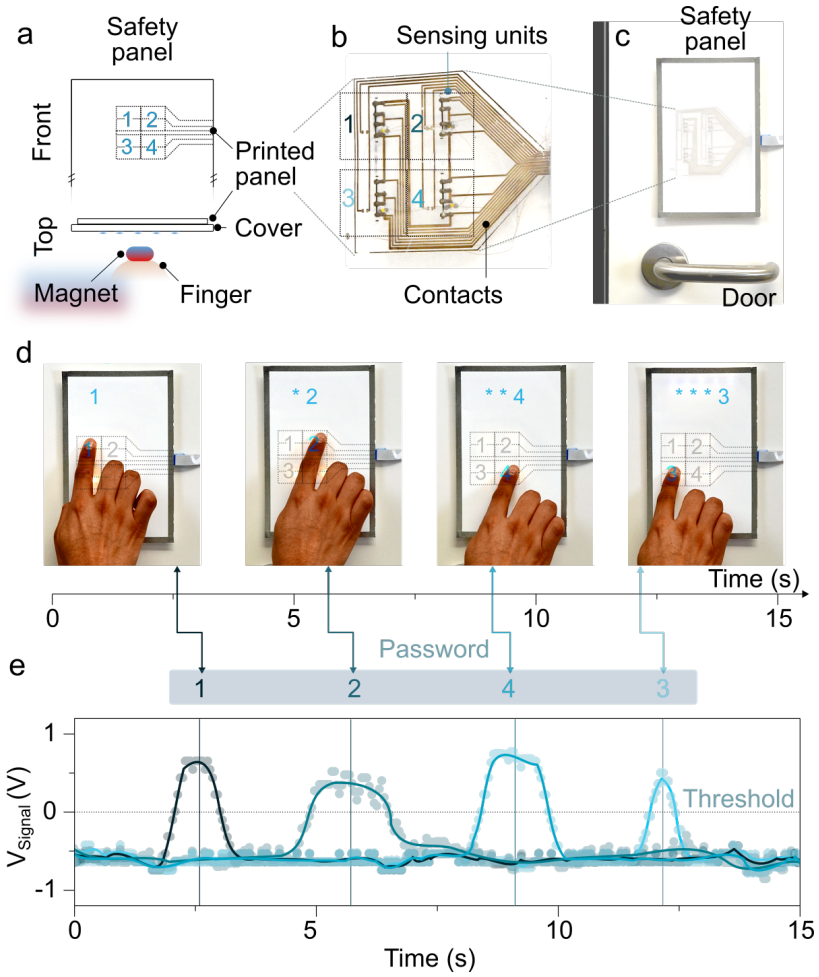

Figure 4.19: Printed magnetically interactive panels for safety applications. a) A magnetically interactive panel is placed behind a cover close to a door. The panel is used as a touchless keyboard to access a password code that confirms permission to enter a room. b) Each of the sensing units is assigned to a digit and c) placed in a user-defined location. d) Sequence of pictures showing the touchless keystrokes made by the user to make a sequential input of the password "1243". e) Timetraces of each independent signal where "High" signal levels are registered as a keystroke of the correspondent digit (Adapted from [126], used under CC BY 4.0).

The examples presented in this chapter demonstrate the potential of remote interaction between printed sensors and magnetic fields, enabling touchless interactive devices for on-

skin and larger areas. Such devices are particularly useful in settings such as surgery rooms or public spaces, where the risk of pathogen transmission can be reduced. However, to fully implement printed magnetic field sensors, several challenges are still to be addressed, including the development of conditioning electronics, the integration of magnetic field sources, and the reduction of power consumption. Despite these challenges, the scientific and technological advances achieved so far provide a solid foundation for exploring the possibilities and limitations of printed magnetic field sensors.

While printing sensors directly onto flexible substrates expand the range of target materials, it also introduces the risk of mechanical deformations that could impact the sensor's performance. Strain effects are a persistent challenge in flexible electronics. Understanding their contributions is the first step toward addressing this issue but we have to do more, and strategies are needed to remove the mechanical contributions from the signals of flexible electronic devices. In the next chapter, I show a method to remove a significant part of the mechanical signals from the sensing signal of magnetic field sensors.

5 Bringing magnetic field sensors to mechanically active surfaces

Flexible magnetic field sensors might suffer from several mechanical deformations. In general, it is possible to identify three general cases and challenges associated with the integration of flexible sensors into different types of surfaces:

- **Lamination into a static flat surface**, where the sensors are placed in rigid surfaces like walls, windows, or furniture. This implementation benefit from the thin format of the flexible sensors but there are no major stresses due to deformation. Typically, no major calibration procedures would be required after integration.
- **Lamination into a static curved surface**, implies that the sensor will be deformed during the fixation process to a rounded target surface. The sensor will experience constant bending stress that might change the initial resistance and sensing characteristics of the device. The sensor can be calibrated after integration to account for these changes.
- **Lamination into mechanically active surfaces**, which considers that the sensor is implemented into systems that are constantly moving and deforming. These cases impose greater challenges due to the fact that the resistance and sensing parameters can be affected continuously due to mechanical stresses. Simple calibration cannot account for the deformations occurring during the normal operation of the device.

In this chapter, it is shown the effective reduction of mechanical contribution to the signal of magnetic field sensors even when they are continuously deformed when laminated

into mechanically active surfaces. The results shown in Sections 5.1 and 5.2 are part of a manuscript under preparation that reports the fully-electrically decoupling of mechanical strain in magnetic field sensors.

5.1 Highly sensitive out-of-plane flexible magnetic field AHE sensors

Using thin film fabrication of magnetic field sensors has been demonstrated as a valid approach to creating magnetic field sensors [17]. Examples using AMR, GMR, tunnel magnetoresistance (TMR), Hall, and planar Hall effects have been shown to create magnetic field sensors on flexible foils [17]. Among these, examples showing selective out-of-plane sensitivity are related to the use of out-of-plane GMR and Bi Hall effect sensors [93, 99, 100]. These examples have been proven useful as temporary and latching switches and as laminated sensors for wearable electronics. Their challenges for extending these technologies are related to the involved fabrication of OOP GMR multilayers and the limited Hall sensitivity of Bi thin films. High sensitivity is needed to screen mechanical effects from the sensing signal and the use of more simple sensing stacks would increase the feasibility of accessible production methods. A good candidate to cover these two challenges is the use of thin films with high intrinsic AHE and strong spin-orbit coupling [69]. [ferromagnet (FM)/Pt] systems are known to have a large anomalous Hall angle, coming from the highly polarized current produced in the Pt layer that generates strong spin-orbit torques in the ferromagnetic layer [146]. Using ultrathin layers of Pt (smaller than the spin diffusion length) is possible to enhance the spin-orbit coupling and as a result the anomalous Hall sensitivity of the system [146, 147]. We decided to study the system [Co (1-5 nm)/Pt (1 nm)] (Figure 3.4) profiting from the high intrinsic AHE of Co and staying below the range of the spin diffusion coefficient of Pt (1.2 nm at room temperature). As for flexibility, we employed ultrathin Mylar (2.5-µm-thick) foils as substrates for having highly conformal magnetic field sensors (Figure 5.1a) that can be bent to different surfaces with a small mechanical interference (Figure 5.1b).

The AHE of 400-µm-width Hall crosses deposited on Mylar were tested for different Co thicknesses (Fig 5.2a). The series of samples showed an exponential trend of sensitivity with the thickness of the Co layer (Fig 5.2b) showing a sensitivity close to 100 $\Omega\ T^{-1}$. These results showed the possibility to have tunable sensitivity over two orders of magnitude upon the change in thickness of the Co layer by a few nm. By testing the Hall resistance noise of the

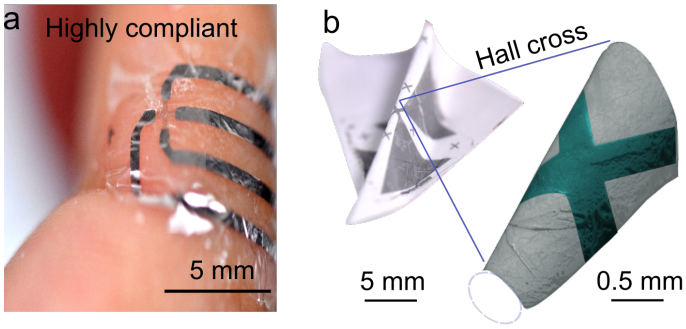

Figure 5.1: Flexible ultrathin AHE sensors. a) AHE sensors fabricated depositing a bilayer of [Co (1.5,2,3,4 nm)/Pt(1 nm)] onto an ultrathin Mylar flexible foil. The sensors are highly compliant and can be laminated on different surfaces b) with minimal mechanical interferences as shown with a sensor placed on a folded paper plane.

1.5 nm Co Hall crosses at different currents (Figure 5.2c), we estimated a high resolution of these sensors of 20 nT (Eq. 3.6).

5.2 Cleaning the signal of strained magnetic field sensors

This section contains the results of the characterization of the flexible AHE sensors using the ZOH spinning current strategy that is known to remove parasitic contributions from the Hall offset signal [127, 128, 148, 149]. Figure 5.3a shows a schematic representation of a Hall cross as a Wheatstone bridge circuit. A current source feeds the current direction of the Hall cross, and a voltage is generated in the direction perpendicular to the current. In an ideal Hall cross with perfectly symmetrical arms, the Wheatstone bridge will be perfectly balanced with identical resistive values and a voltage difference of $\Delta V = 0$ V. In that way, any measured voltage change corresponds to the voltage generated by means of the Hall effect of the sample. In reality, the arms in a Hall cross will have small geometrical and alignment defects

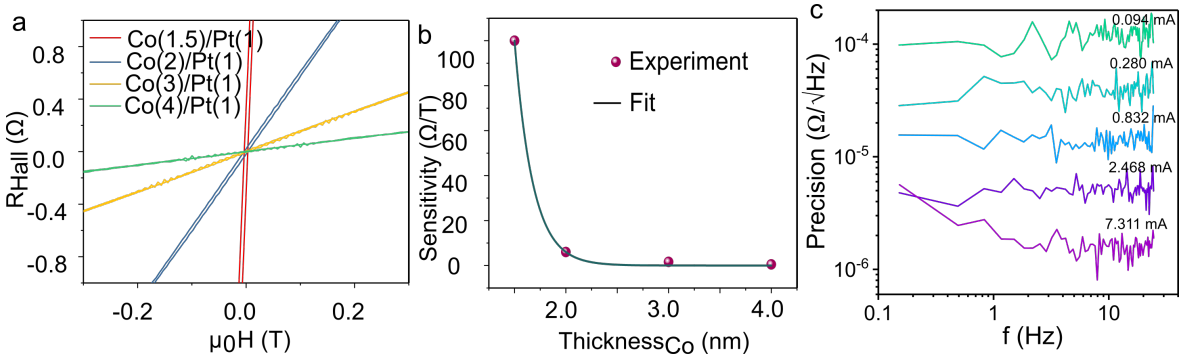

Figure 5.2: Performance of flexible AHE sensors. a) The Hall resistance dependence of 400 μm-width Hall crosses showed b) an exponential trend of the sensitivity with the reduction of Co thickness. c) After checking the noise of the Hall resistance for the sensors fabricated with 1.5 nm Co layers, we estimated a maximum resolution of the sensors of 20 mT when driven at 7.3 mA.

that will change the balance of the Wheatstone bridge outside the equilibrium $\Delta V \neq 0$ V. In such cases, the sensor signal will have an additional offset due to these geometrical defects even when no magnetic field is applied. Additionally, in case the Hall cross is designed for flexible applications, bending effects can also contribute to the offset changes. For example, during uniaxial bending, the sections of the Hall cross parallel to the bending axis will experience larger tensile stress while the areas perpendicular to the bending axis will experience smaller tensile stress. This again changes the balance of the bridge and further offset in the sensor signal is expected. If the flexible sensor is aimed to be used in flexible applications where mechanical deformations occur, the Hall resistance signal might not be reliable due to the fact that it will contain magnetic and mechanical contributions. For these reasons, we opted to use the ZOH spinning current strategy that we expected to diminish the offset effects. As explained in Section 3.3.2, by switching the direction of the current flowing through the Hall cross, measuring the respective Hall resistance in both directions, and averaging them, it is possible to remove the longitudinal contributions from the transversal signal of the Hall structure.

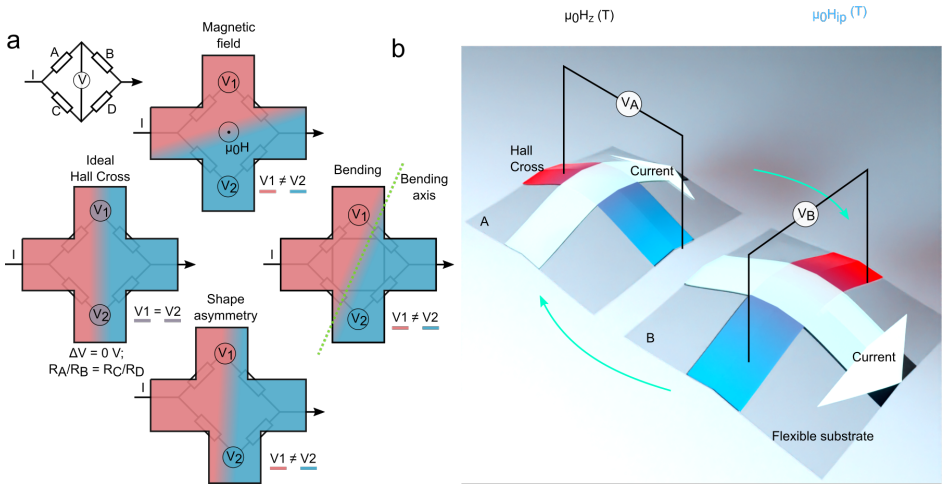

Figure 5.3: Offset reduction in Hall effect sensors. a) Magnetic field sensors using Hall geometry can be modeled as a Wheatstone bridge, where the transversal voltage accounts for the corrections of the bridge voltage coming from shape asymmetries and mechanical deformations. A perfectly aligned Hall cross would show a zero voltage difference along the bridge, but the misalignment of arms or stresses occurring during the fabrication or operation of the sensors will change this offset away from the zero voltage level. b) Using the ZOH switching current strategy is an effective method to account for these artifacts in the offset signal and here, I explore it to actively using it for continuous monitoring of sensors placed in mechanically active surfaces. In this strategy, the current is passed through the two orthogonal directions of the Hall structure, and the ZOH voltage is obtained as the average of the transversal voltage in each of the directions.

Figure 5.4 shows the comparison between the Hall resistance signal of a bent flexible AHE sensor [Co (2 nm)/Pt(1 nm)] measured using the conventional Hall and the ZOH strategies. When the sensor characteristics are measured using conventional Hall measurements during a static bending experiment (Section 3.3.5), the sensor shows a clear instability of the Hall

resistance signal. By changing the radius between the flat down to a 3.1 mm bending radius, the signal offset changes non/monotonically between 3 Ω and -30 Ω. This behavior confirms the unsuitability of using conventional Hall measurements to measure a sensor that is constantly changing its mechanical configuration. Figure 5.4b shows the Hall signal at the same bending conditions as those shown in (Figure 5.4a). The signal shows a linear behavior during the full bending test, with an offset that keeps in the range from ± 0.1 Ω(Figure 5.3c), and sensitivity for 9 Ω T^{-1} (Figure 5.4d). These results show the decrease of the offset range using ZOH more than 100 times with respect to the measurement using conventional Hall measurements. By checking the sensitivity profile of both cases, we noted a similar pattern in both cases showing a sensitivity of 9 Ω T^{-1} and 7 Ω T^{-1}, for the ZOH and Conventional Hall cases, respectively. As noted in (Figure 5.4a), not only offset but additional artifacts leak into the Hall effect signal that might be related to the longitudinal contributions of the MR response of the film. Meaning that the technique also removes additional magnetotransport contributions from the Hall signal. These artifacts also affect the calculation of sensitivity giving an effective lower value for the measurement using conventional Hall measurements.

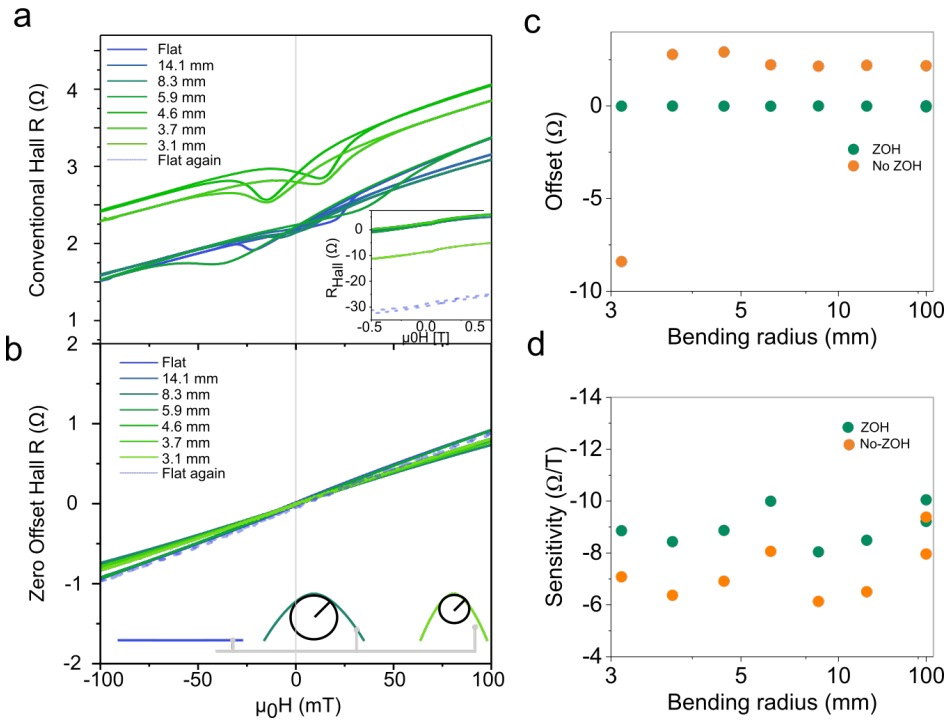

Figure 5.4: Comparison of conventional Hall and ZOH in bent samples. a) Conventional Hall effect measurement of a [Co (2 nm)/Pt(1 nm)] AHE sensor during a static bending test. The signal shows some artifacts related to the magnetoresistance of the sample with an additional strong influence on the offset position. b) Measurements employing the ZOH methodology remove most of both contributions and show a highly linear behavior of the sample at different bending radii. c) Comparison of the offset resistance for conventional and ZOH measurements and d) the calculated sensitivity in both cases.

For testing the effect of the ZOH switching strategy during continuous deformations of the

film, we placed a sensor for a cyclic bending test of 600 cycles (from 10 to 15 mm) in a constant field of 50 mT (Figure 5.5). Due to the aging of the sample, the resistance drifts slowly at a rate of 8.1 $\times 10^{-6}$ cycle^{-1}. Taking as an example the detail of the resistance of the sample after 400 cycles of bending, we noticed the classical resistance fluctuations given by the straining of the sample accompanied by the slow wear of the sample (Figure 5.5b). By checking the conventional Hall resistance, we notice that the signal fluctuates without drift with an standard deviation (SD) standard deviation of 0.028 Ω. The signal shows an average value of 3.234 Ω with a clear oscillation pattern that accounts for the leaking of the strain contributions to the Hall signal. When using the ZOH switching current strategy, the Hall signal has an average of 0.410 Ω with a SD of 0.004 Ω. Meaning that during continuous deformation of the sensor between 10 mm and 15 mm radius, the ZOH strategy reduces the mechanical contributions into the sensing signal by more than 6 times. For larger deformations, this reduction in mechanical contributions would be even more significant as the observation during the static bending tests. Such capabilities demonstrate the possibility to use the produced AHE sensors even when they are continuously deformed as if they are laminated on actuators or skin applications.

Sensors used for on-skin applications might be particularly subjected to continuous unpredictable deformations. This reduces the possibilities of calibration of the signal response because of the reconfigurability of the stresses during motion. When a highly compliant sensor film is laminated on the skin of a user, the sensor will adapt to the naturally occurring curvatures of the skin. As an example, Figure 5.6 shows a schematic representation of a sensor film laminated on the palm of the user. When the palm is extended, it is expected that almost flat or low curvature profiles will be observed. But when the palm is closed (e.g. to

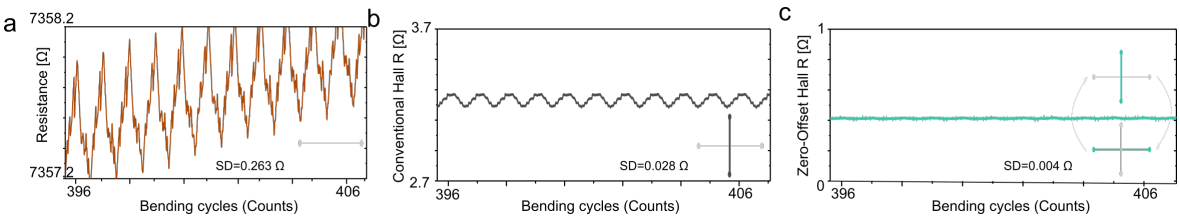

Figure 5.5: Comparison of the signal of the AHE sensor during a cyclic bending test at a constant field of 50 mT. a) The resistance of the Hall effect sensors shows the oscillations typically observed during the cycling of the samples at different curvatures. In each cycle, the sensor increases the base resistance, and the dynamic deformations are observed as low and high levels of resistance. b) The conventional Hall resistance of the sample is plotted, here the drift is effectively removed but the strain-related oscillations still persist in the signal. c) The ZOH resistance signal shows low remainders of the mechanical deformation in the magnetic field signal. Notice that the amplitude range in all the plots is the same (1 Ω), so even with a visual inspection is possible to notice the effects of the fully-electrical decoupling of the signal in the continuously deformed AHE sensors.

hold an object) strong deformations with high curvature will be generated. Higher curvature means higher stresses on the sensing area that can pass to the signal of the sensor.

Based on the positive results obtained from static and cyclic bending experiments, in which we used ZOH to remove most of the mechanical contributions in controlled tests, we decided to test the mechanical filtration capabilities of ZOH on the non-deterministic folding of palm skin. Figure 5.6b shows a sensor laminated on the extended palm skin of the user (top), after closing the palm the sensor is corrugated and conforms to the creases formed during this gesture (right). The sensor, in this case, can be repeatedly bent during the normal opening and closing of the hand. Figure 5.6c shows the changes in resistance, conventional Hall, and ZOH signals during the deformation of the sensor, as well as during the detection of a permanent magnet proximity. The 35-second-long sequence contains signals from the sensor placed in the palm of the user. At approximately 12 s, a permanent magnet was quickly approached and removed while the hand remained still. At 16 seconds, the hand began to close and then opened again, causing deformation of the sensor. At 20 s, the sensor was approached even closer with a permanent magnet. Another deformation occurred after the hand was closed and opened for a longer period at 27 s.

The analysis of the ZOH resistance demonstrated the effective removal of the mechanical contributions from the magnetic field signal even during non-deterministic deformations of the skin. The resistance level only responds to mechanical deformations. The conventional Hall contains mechanical and magnetic contributions that are even of similar amplitude (few Ω). The ZOH, "on the other hand", only responds to the magnetic contributions occurring during the sequence.

Such capabilities are a very promising result that could place the use of highly flexible Hall effect magnetic field sensors even on surfaces that are constantly moving. The skin is one example where laminated magnetic field sensors might find applications in the production of accessibility wearables that are used for communication or interaction. Such a highly user-integrated platform would need to be mechanically imperceptible and easy to wear. This means that not only the sensor but also the magnetic field source has to be a highly conformal system. In such cases, our magnetic electronic skins can meet with flexible magnetic skins. Magnetic skins can be produced with permanently magnetized particles embedded in a polymeric matrix (see Section 3.4.1). For this demonstration, neodymium-iron-boron (NdFeB) microparticles embedded into a PDMS matrix are spin-coated to create a 100-µm-thick flexible magnet. The compliant magnet was laminated to the thumb of the user as a motion

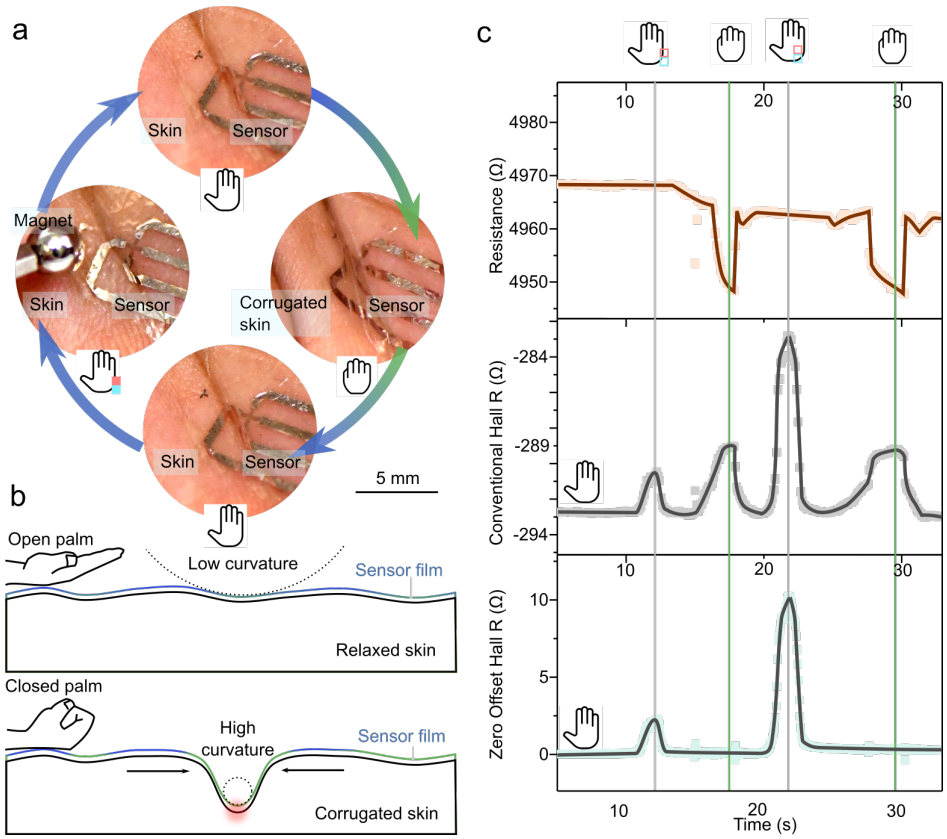

Figure 5.6: Mechanical stress decoupling in on-skin laminated sensors. a) An AHE sensor laminated in the palm of the user is subjected to magnetic and mechanical stress stimuli. The sensor is even placed close to a folding line of the palm and severely folded during the closing of the palm (note the symbols of extended and closed hands on each panel). b) Schematic representation of the layout of the sensor on the skin. When the palm of the user is extended, several folding with low curvature will be formed, when the palm closes some high curvature regions might appear creating a large deformation in the laminated sensor. c) The resistance (top), conventional Hall (middle), and ZOH (down) resistance are plotted during the operation of the sensor laminated in the palm of the user. The experiment starts with the sensor placed into the open palm, after approaching a magnet (12 s), the conventional and ZOH signals show a response to the magnet as expected. Then the user closes and opens the palm (16 s), the resistance and conventional Hall resistance respond to this gesture, which is not desired for the selective detection of magnetic fields; notably the ZOH signal remains highly stable during this deformation. After approaching the magnet even closer to the sensor (20 s), the sensitivity of the sensor is clearly confirmed in both, the conventional and ZOH resistance signals. A second deformation of the sensor also confirms the effective decoupling of the mechanical contributions in the ZOH signal.

tracking label with respect to an AHE sensor placed on the finger [Co (1.5 nm)]. In such a case, after approaching the thumb to the phalanx with the sensor, the system would notice the proximity and use it for triggering a user-defined command. In this example, we employed it as a Morse communicator, where the user writes a message based on the proximity and the duration of the gestures. The user writes HZDR with a combination of long and short pulses that are determined by the duration of the signal over a threshold level of 2 Ω. Such ultraportable typing devices might be adapted to user-specific configurations of magnetic labels and sensors. The flexible magnetic skins used in these demonstrations show a typical surface field of only 15 mT, this field is already enough to actuate the full dynamic range of the highly sensitive AHE sensors. Given the high flexibility, sensitivity, and selectivity of the

flexible AHE sensor is possible to avoid bulky magnets, that despite easy detection are not seamlessly integrated into ultraportable applications.

5.3 Lamination of flexible AHE sensors in magnetic membranes for soft actuators

Soft robotics, and in particular magnetic soft actuators, might be a technological area that could benefit from the use of flexible magnetic field sensors for having actuation feedback mechanisms. Soft actuators benefit from the high flexibility of their mechanisms to create

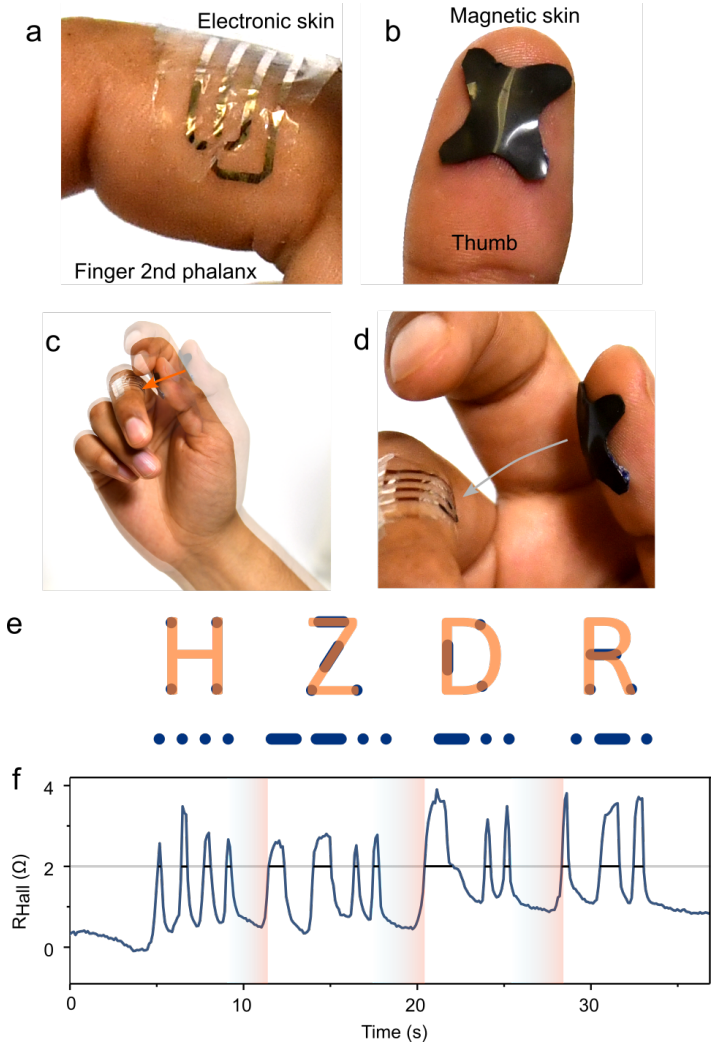

Figure 5.7: AHE sensors for on-skin flexible Morse communicator. a) A highly conformal AHE sensor is placed on the skin of the phalanx of the middle finger. b) The sensor interacts with a flexible permanent magnet placed on the thumb fingertip. c) By intermittently tapping the thumb against the pointing finger, d) the mutable distance between the complaint magnet and the sensor can be registered. e) As an example, the message "HZDR" is f) tapped using this device. Depending on the time expended above a defined threshold level, long and short pulses can be interpreted as the long and short taps that are used for Morse communication.

safer, versatile, and biomimetic mechanism systems. Despite huge advances to create versatile soft machines, examples showing the integration of ultrathin flexible magnetic field sensors were scarce. This is related to the challenges of having reliable sensing responses during the actuation of these systems. Using AHE flexible sensors based on the anisotropic Hall effect (AHE) with high flexibility, sensitivity, and selectivity it is possible to have a seamless integration of a sensory system in magnetic soft actuators. This section contains examples of using the sensors in magnetic actuators as guidance for folding and lifting.

The findings presented in Sections 5.3.1, 5.3.2 have been published in the following article [10]. The results highlighted in this manuscript summarize my contributions to the reported research, with additional data from the paper needed to understand the motivation behind this study. The preparation of the Labview controls and actuator with laminated sensors were conducted by Dr. M. Ha and Dr. G.S. Cañón Bermúdez, the framework to estimate the actuation angles was proposed by Dr. B.A. Evans.

5.3.1 Tetherless folding of magnetic origami foils

Origami structures despite having a long tradition of development are still relevant for the engineering and design of functional structures [150]. From self-deployable structures, through shape morphing systems, to robotics, origami-inspired systems have been studied [151, 152]. A paper foil can be folded into an infinite number of shapes, so it can be transformed into a functional structure by following a specific folding sequence. Origami-like soft systems that are programmatically folded without human manipulation have been demonstrated by using in-material programming through the local magnetization of magnetic foils and membranes [114]. Assembling from 2-D to 3-D layouts has been realized to create rotating walkers and arthropod-like configurations [114, 153]. Despite these advances, there was a lack of a flexible magnetic onboard feedback system that assessed the folding of origami-like magnetic soft actuators without hindering their actuation capabilities. Here, the use of flexible AHE sensors laminated into magnetic shape memory polymer is shown.

The magnetic origami foils were created by embedding NdFeB microparticles into a SMP DiAPLEX [129]. The use of SMP allows for the manipulation of the softness of the material to be manipulated by heating, making it possible to have a transient soft actuator that can bend with weak stimuli and hold the actuation state. By adding magnetic particles, the foils can be manipulated via magnetic fields, allowing for untethered actuation. To achieve

remote actuation, a heating mechanism that was compatible with the system was required. Photothermal heating using a high-intensity visible light lamp was selected (see Section 3.4.2). The employed DiaPLEX SMP has a glass transition temperature of 50 °C, where the Young's modulus of the system drops from the GPa to the MPa ranges. IR temperature image mapping showed that magnetic composite SMP foils had an enhanced photothermal effect due to the high absorption of the magnetic powders (Figure 5.8). Samples heated in one of the corners using the high-intensity lamp for 45 s showed a maximum temperature of 71 °C and 47 °C for the powder-containing and simple SMP, respectively. As shown in Figure 5.8d, the temperature saturation was achieved after 20 s, and it took a similar timeframe to cool down to room temperature. Based on this, we confirmed the suitability to go beyond the transition temperature of DiaPLEX without creating permanent damage to the polymer by excessive heating.

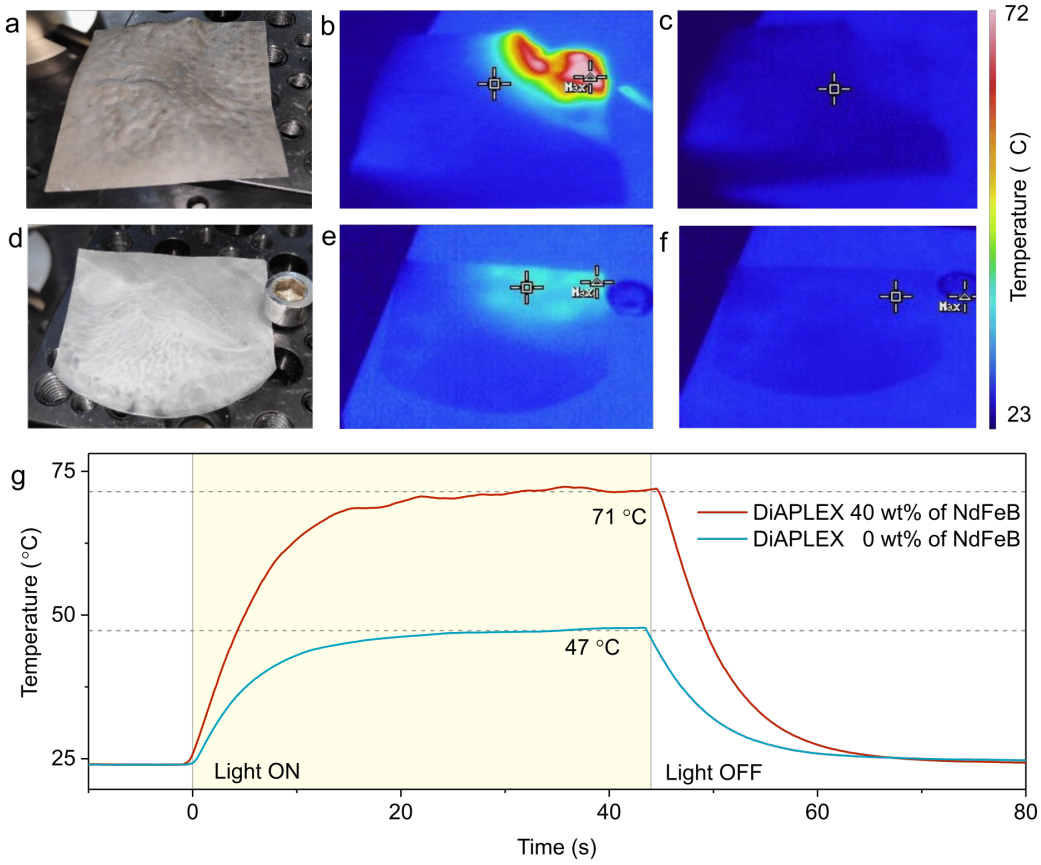

Figure 5.8: Photoabsorption of magnetically actuated membrane with shape memory properties. a) A foil membrane containing a load of 40 wt% NdFeB particles in DiAPLEX. b) The membrane is illuminated with a visible light source (2800 lm) to activate the local photoabsorption heating of the particles. The temperature registered using an IR camera demonstrated the heating of the sample up to 71 °C. c) After turning off the lamp, the polymer cools down back to room temperature. d) A similar experiment using a DiAPLEX foil without particles embedded was performed, e) the local illumination of the corner raised the temperature up to 57 °C, f) and cooled down to room temperature 10 s after turning off the lamp. g) Shows the temperature profile of the irradiated area during and after the illumination experiment (Adapted from [10], used under CC BY 4.0).

As for the actuation via magnetic fields, the use of an electromagnet allowed for the facile

electronic control of the intensity of magnetic fields applied to the magnetic origami foils (Figure 5.9). By measuring the radial *r* and OOP *z* components of the electromagnet field (ITS-MS-3025) driven at 0.32 A), a profile of the actuation field was obtained. The field shows a maximum intensity of 35 mT at the center of the electromagnet, and a gradient field is created around the actuation area (Figure 5.9e). For actuation, a section of the magnetic origami foils was fixed on the upper face of the electromagnet and a free section was left for actuation. Depending on the geometrical, composition, and magnetization properties of the actuator, a predicted bending angle can be estimated from the magnetostatic interaction and torques produced in the system. Equation 5.1 describes the expected bending angle of the magnetic origami actuator as:

$$\phi = 6B\, L_E\, L_M \frac{M_{NdFeB}\, f_v\, (1 - f_v)}{E_D\, a^2}, \tag{5.1}$$

where M_{NdFeB} corresponds to the magnetization of the NdFeB fillers, f_v to the volume fraction in the polymer, E_D to the Young's modulus of the polymer. a refers to the thickness of the foil and L_E and L_M correspond to the free section subject to bending and the non-strained free section, respectively. Using these design parameters we identified a suitable configuration for obtaining 180° folds. We found three general cases (Figure 5.9f) that consisted of i) samples that were easily folded to 180° but the content of particles was so high that the SMP where lost, ii) samples that were easily folded still having full shape recovery and iii) samples that did not actuate fully. Case i) was observed after using local illumination of the tip of the actuator with the electromagnet activated, the sensor folded but after removing the field and heating again, the initial flat layout was not recovered. Case ii) presents the desired behavior for origami-like folds because it is able to fold to 180° and still show the shape recovery characteristics. Case iii) occurred for low concentration of magnetic fillers making difficult the actuation of the origami foils. Having a comprehensive sweep of concentrations and foil thicknesses (Figure 5.9g), it was possible to identify a suitable concentration of 40 wt% and 60 µm thickness to achieve full actuation with remanence of the SMP properties that corresponded with the expected actuation angles predicted by the equation 5.1 (Figure 5.9h).

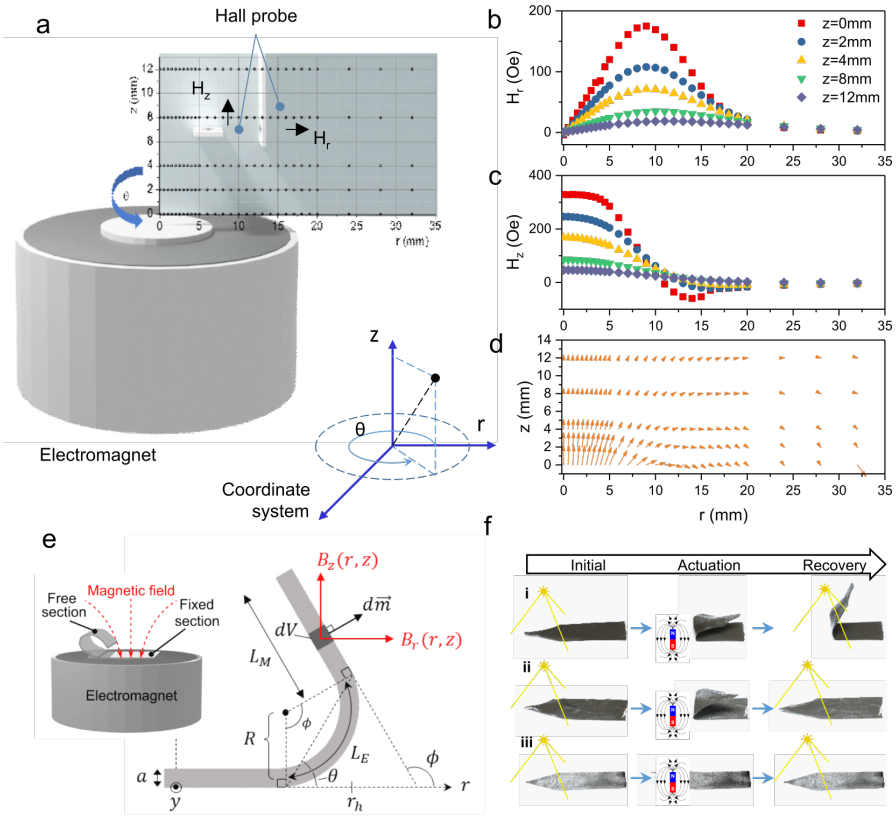

Figure 5.9: Origami-like folding of SMP-based magnetic membranes. a) An electromagnet was used to drive the origami-like folding of the actuators. The field profile of the electromagnet was characterized using a Hall probe in the b) radial and c) OOP directions. Due to the radial symmetry of the electromagnet, d) the full profile of the field was characterized after measuring a single plane with origin in the center of the top face of the electromagnet. e) A membrane placed on top of the electromagnet with a free section is actuated according to the description in Eq. 5.1. f) After local illumination of the free section and actuation with magnetic fields, we found three cases depending on the magnetic filler loading into the shape memory polymer: i) sample was fully actuated but lost most of it SMP properties (80 wt%), ii) the magnetic content was enough for absorption, actuation and recovery of the SMP properties (40 wt%), and iii) where the particle loading was low and folding of the sample was not possible (20 wt%). For the full actuation of origami-like structure, the case ii) was preferred (Adapted from [10], used under CC BY 4.0).

5.3.2 Assesing the folding of magnetic origami foils using flexible AHE sensors

After realizing functional actuating magnetic origami foils, we continued to place flexible AHE sensors [Ta (1 nm)/Co (2 nm)/Pt (1 nm)] for checking their actuation state. Figure 5.10, shows the magnetic skin measuring the fields during the assembly of a boat-like (or onigiri-like) layout. The sensor system consists of an array of 4 sensors placed into the top, right, left, and center of the magnetic origami foil. Each of the sensors is addressed individually, giving the possibility to track the out-of-plane contributions of the magnetic field during the folding sequence. Figure 5.10c shows a schematic representation of the magnetic field vectors when a section of the origami is being folded. Depending on the location of the sensor with respect to the center of the electromagnet, the magnetic field intensity will show a profile with a local maximum at 25° (Figure 5.10d). Based on this behavior it was possible to use

the sensing AHE array to track the sequence that was used to fold the onigiri-like shape. Knowing the order of sequence allows more efficient opening of the layout, trying to open back in the wrong order will result in the robot hindering itself during disassembly (Figure 5.10f). As an example, it is shown the signal of the sensors when sequence 1 was followed. First, the magnetic field is turned on. This is observed in all of the sensors by increasing the produced Hall voltage. Then the panel on top is activated by locally heating this area and completing the folding at 17 s. Similarly, the left flap is illuminated to heat this area and promote its actuation which is completed at 36 s. After unfolding the structure (70 s) the signals go back close to the initial state at 0 s. Being able to recover the initial state, also permits the folding of the structure in similar layouts using a different sequence and eventually in new different shapes in the spirit of pluripotent origami structures.

5.3.3 Tuning the dynamic range of AHE sensors for feedback control of chained-Fe soft actuators

For some applications of soft actuators, it might be desirable to compromise in sensitivity to have a larger dynamic range. Magnetic soft actuators could present different actuation ranges that depend on the fillers and the mechanical properties of the polymer matrix. As an example of this case, Figure 5.11 shows the use of AHE [Co (4 nm)/Pt (1 nm)] sensors to detect the significative fields needed to actuate the lifting motion of a composite of chained Fe microparticles in Irogran. The sensor showed linear sensitivity up to 700 mT (Figure 5.11b) which is compatible with the field needed to actuate the system. To assess the lifting angle of the magnetic soft actuator, we proposed a differential measurement. By checking the Hall voltage input of a fixed sensor (sensor 1) compared with the output of a mobile sensor (sensor 2) it was possible to link this difference to the lifting angle (Figure 5.11c).

A calibration was done by placing the lifter with a laminated sensor in a homogeneous horizontal field at different intensities (Figure 5.11d). By increasing the intensity of the field, the lifting of the angle increases up to 83° (Figure 5.11e-g). This characterization allowed setting a feedback control implementation by controlling the applied field of the coils by comparing the voltage difference with the voltage expected for a user-defined angle (Figure 5.11h). This enables one of the first demonstrations of closed-loop control of magnetic soft actuators owing to the lamination of flexible AHE sensors. This is verified by the use of a load attached to the lifter (Figure 5.11i-k). After changing the load, the closed loop

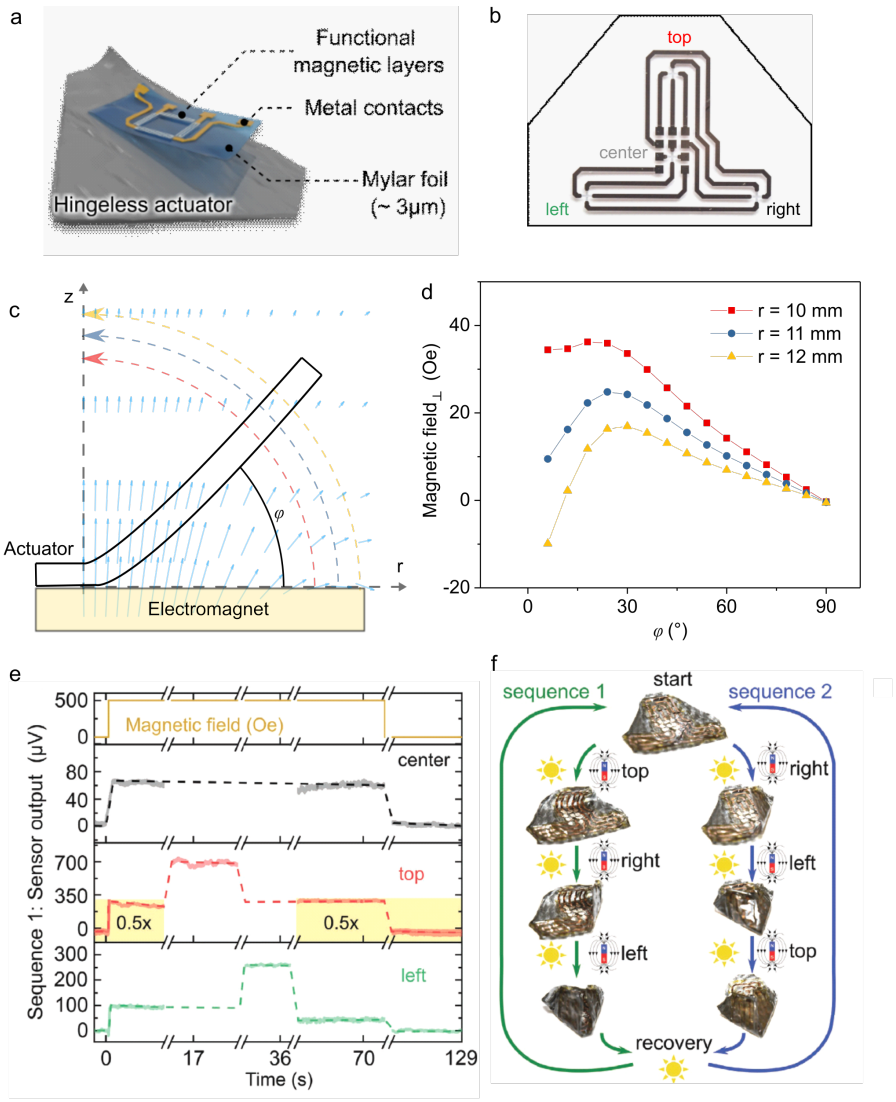

Figure 5.10: Flexible magnetic field sensors assessing the folding of magnetic actuators. a) Shows a schematic representation of the magnetic origami actuator with a laminated magnetically sensitive electronic skin. b) Array of flexible AHE magnetic field sensors used for detecting the OOP magnetic field contributions experienced by the actuator during the folding process. It consists of 3 free sensors and 1 reference sensor in the middle of the array. c) When the actuator is folded via the electromagnet described in Figure 5.9, the sensor will experience different field components during the operation. d) In particular, the AHE sensors, sensitive to OOP fields, will sense different strengths of field components with respect to the actuation angle. Understanding this behavior, e) we were able to demonstrate the tracking of the signal sensed during the folding process of a magnetic membrane into an onigiri-like layout. f) Depending on the assembly sequence employed, the magnetically sensitive skin integrated into the actuators can give us the register of their motion that can lead to an efficient recovery of the initial shape (Adapted from [10], used under CC BY 4.0).

feedback system allows for recovery of the set point angle value during the manipulation of the attached weight (Figure 5.11l).

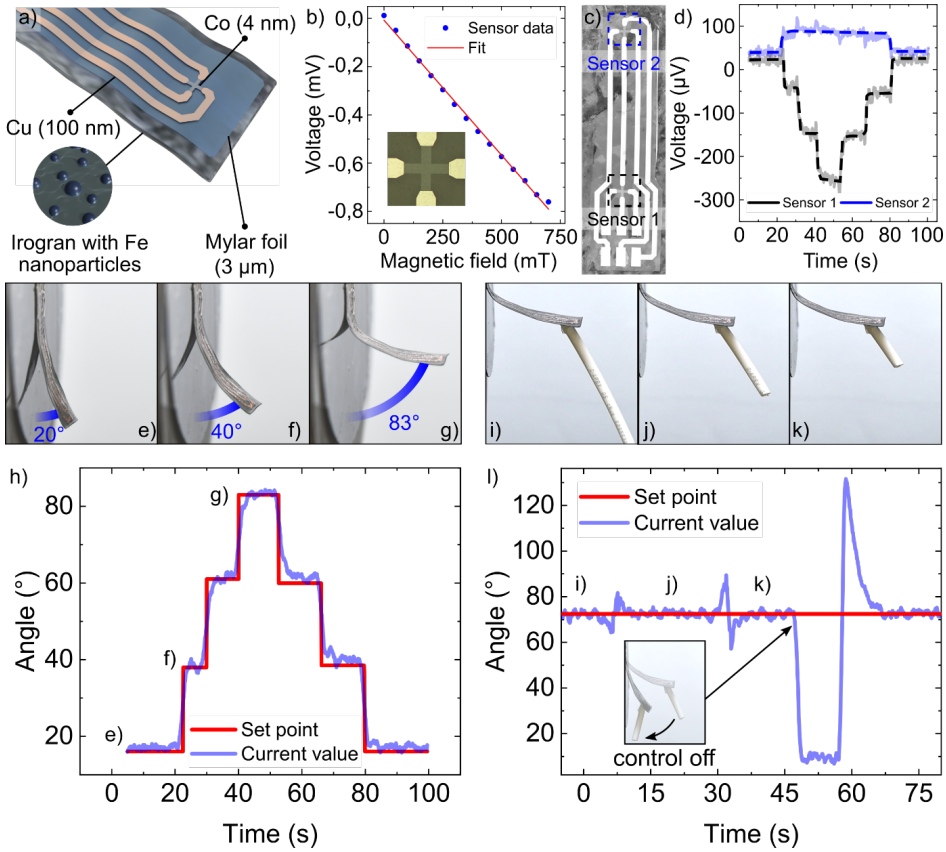

Figure 5.11: Feedback-controlled magnetic lifter using flexible AHE sensors. a) Magnetic lifter consisting of chained Fe particles embedded in Irogran matrix, with a laminated magnetosensitive skin. b) The sensor shows a linear response above 500 mT which is required for the full actuation of the magnetic lifter. c) Micrograph of the sensing platform showing the two sensors employed for the manipulation of the feedback control of the lifter, one is used as a reference, and the second measures the OOP components of the actuating field. d) Output voltage of sensors 1 and 2 as a function of time in response to increasing and decreasing magnetic field steps. Each step corresponds to an increase or decrease of 100 mT. e-g) Shows the sensor incrementally changing the angle with the applied magnetic field from 0 to 300 mT. h) Using a control unit to set a defined angle (red), the lifter bends to the commanded angle (blue) effectively setting the desired actuation. This approach is useful for feedback control of the actuation angle independently from i-k) the load carried by the actuator. l) The presented example shows a lifter carrying varying weights while being commanded to bend to a specific angle. The real angle value changes temporarily during the manipulation of the weight but the feedback system rapidly returns the actuator to the commanded value (Adapted from [10], used under CC BY 4.0).

5.4 Non-linear dynamics of magnetic soft actuators

Due to their mechanical properties, soft actuators are expected to provide safe interaction and collaborative platforms with humans [117]. Such collaborative mechanisms can work as an "exomusculature" to assist with rehabilitation and fine motricity tasks [154]. For example, our motions are typically below 100 Hz and our typical response reflex time is in the range of 100 ms [155]. These complex tasks would need to consider speed, safety, and social compatibility with the users [101]. In Section 5.3, I provided examples of how a soft machine might be integrated with flexible electronics to produce proprioception feedback and awareness of the environment. Despite magnetic actuators can provide a

useful platform for programming the actuation inside the material, a feedback system can confirm the success of the command. This becomes especially relevant when soft actuators are actuated at high speeds. High-speed actuation can create non-linear behavior on soft robots due to their low mechanical impedance [156]. While conventional rigid machines can operate at several thousand revolutions and linear actuation per second [157], magnetic soft actuators have so far achieved only a few hundred motion cycles per second [113, 158–160]. Typically, the dynamic regime in soft actuators is restricted to a deterministic one, and few examples appear that use resonant actuation regimes, and some report to avoid non-linear regimes [161–164]. Here, I describe the appearance of non-linear and even chaotic behavior of magnetic soft actuators driven at high speeds. This highlights the need for a feedback system to detect when a deterministic input starts to create a non-deterministic actuation response. We study the different regimes that appear after actuating magnetic flexible membranes at incremental speeds and magnetic fields and eventually come out with the possible use cases where a non-deterministic and even chaotic actuation might be useful.

The findings presented in Section 5.4.1 are under preparation for publication. The results highlighted in this manuscript summarize my contributions to the work, with additional data from the paper under preparation needed for the comprehension of the motivation behind this study. Data and analysis from Figure 5.13 were obtained by M. Navarro López and Dr. O. V. Pylypovskyi, respectively.

5.4.1 Dynamic actuation regimes of fast-moving magnetic soft actuators

Figure 5.12 present a magnetic soft actuator that displays different motion regimes. The actuator consists of a magnetic flexible membrane of NdFeB microparticles embedded in PDMS polymer. The membranes are fabricated by spin coating resulting in 80-µm-thick samples that are cut in a bow tie shape with lateral dimensions of 13 mm $\times$ 8 mm with a neck section of 2 mm. After applying a 2.3 T magnetic field to the samples in the out-of-plane direction, they become permanently magnetized and ready to actuate upon the application of magnetic fields (Section 3.4.1). To achieve fast actuation of the magnetic actuators, a pair of coils is employed to generate AMF. The fields are applied horizontally (parallel to the ground level) along the plane of the lying flat actuator (Figure 5.12a). This creates alternating lifting motion of each of the arms of the bow tie geometry that follow the frequency of the alternating magnetic field (Figure 5.12b). This expected behavior persists among different low frequencies f_l and relatively low fields $\mu_0 H_l$. The magnetostatic interaction and torques in

this regime are slowly varying giving a linear output of the actuation with the applied magnetic field. Interestingly, by increasing the intensity $\mu_0 H_c$ and frequency f_l of the magnetic field a non-linear and eventually chaotic regime of motion appears (Figure 5.12c). This chaotic behavior is characterized by a non-deterministic motion of the arm of the actuator that is continuously changing its motion pattern. Figures 5.12d,e, show the image of a fluorescent marker on the tip of the actuator recorded during half of the period of the applied magnetic field. This allows us to visually track the dynamics of the actuator, for example, the linear regime is observed by a clear arc formed by the fluorescent marker during this deterministic actuation. In contrast, the path of the fluorescent marker in a chaotic regime shows random trajectories (Figure 5.12d). Using tracking software of high-speed video recording, it was possible to register the position of the fluorescent marker during several actuation periods and use it for a complete analysis of the dynamic regimes of the actuators.

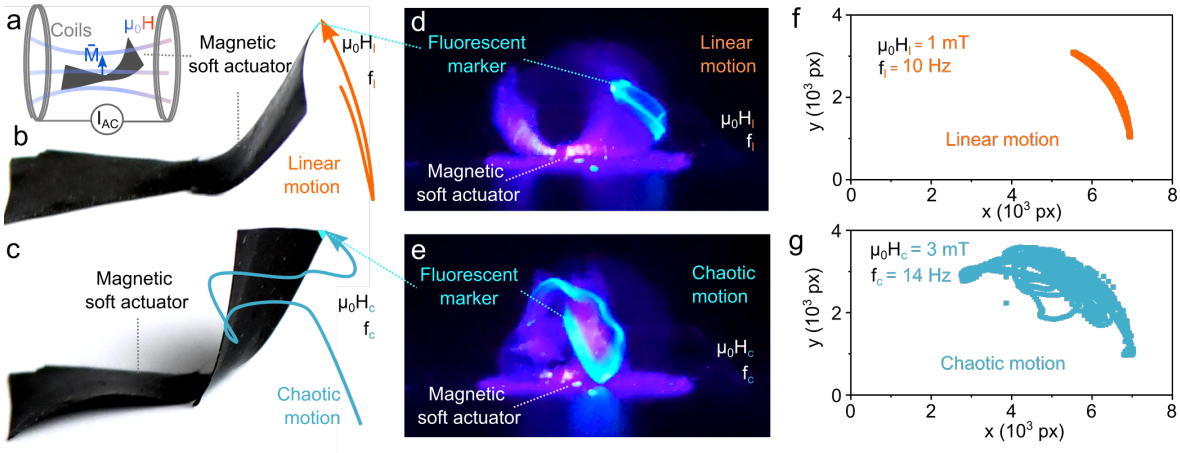

Figure 5.12: Chaotic dynamics in magnetic soft actuators. a) A mechanically soft magnetic membrane will respond to the field produced by an external magnetic field. The employed sources can contain AMF that move the robot according to the frequency and intensity of the magnetic field. b) This expected behavior is considered linear motion since it linearly responds to the applied field and the related frequency. c) The regime of linear motion does not extend for all the spectra, especially for high frequency and high field stimulation, the magnetic actuators can enter to an unpredictable nonlinear chaotic motion. d) The motion of a fluorescent marker at the tip of the robot evidence the linear motion pattern and e) the chaotic motion during long exposure captures. f) By video analysis of the coordinates of the marker during actuation, a complete register of the motion during several stimuli cycles was measured for linear and g) chaotic motion.

A comprehensive analysis of the effect of field intensity and frequency of the soft actuator is shown in Figure 5.13. We designated three main cases that consist of: deterministic linear motion, non-linear deterministic motion, and non-linear chaotic motion. Each motion regime was identified based on the analysis of the x and y position traces of the fluorescent marker placed on the tip of the actuator arm (Figure 5.13a-c). a) The linear case shows the expected oscillations that coincide with the applied magnetic field frequency. The linear denomination refers to the one-to-one correspondence of the field with the position of the marker, and the deterministic feature refers to the programmatically repeated actuation. b)

In the non-linear, yet deterministic regime, additional features were observed that repeated consistently but with a different period compared to the applied AC magnetic field. We termed it "cross-clapping" behavior where one of the arms holds the second arm during actuation, and then reverses the holding arm during the next actuation period (you can imagine folding and unfolding sleeves of a shirt while alternating the sleeve that stays on top). c) Non-linear chaotic regime was observed by non-repeating motion patterns that were not consistent with the applied magnetic fields. This regime was characteristic during actuation at high-intensity, high-frequency AC magnetic fields (Figure 5.13d). This behavior can have multiple factors contributing to it. It may begin with low impedance and inertial flexions that occur during high-speed and high-acceleration actuation, followed by self-interaction of the actuator arms, as well as magnetostatic and Van der Waals interactions between the arms of the PDMS-based magnetic actuator. This increasing number of interactions during strong high-speed actuation, added to a large number of possible mechanical configurations of soft actuators, increases the possibility to observe chaotic dynamics. These results demonstrate that magnetic soft actuators exhibit a variety of dynamic regimes.

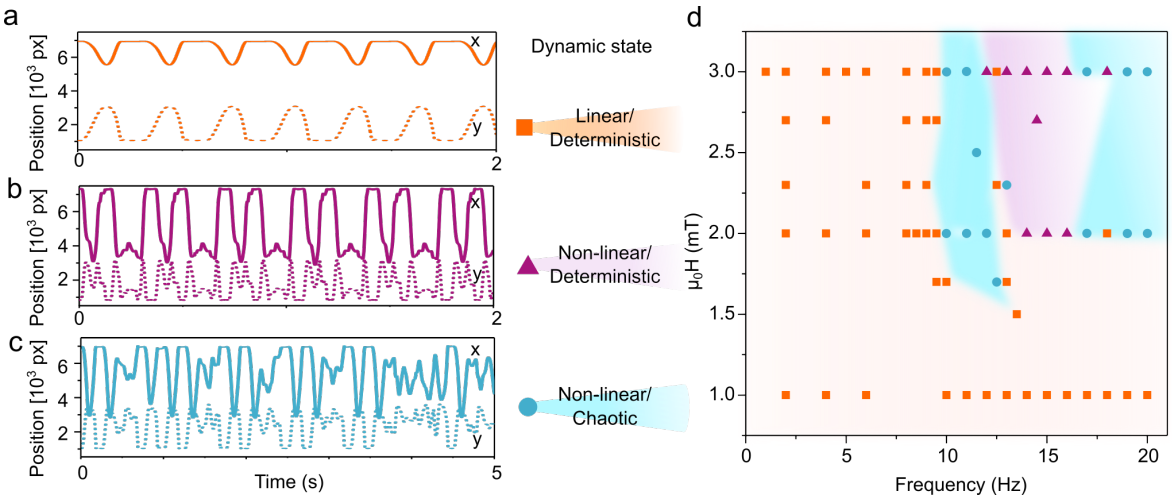

Figure 5.13: Analysis of the dynamic modes in magnetic soft actuators. The tracking in time of the soft actuators reveals a) the predictable and one-to-one actuation of linear motion, b) the non-linear but still deterministic signature of a more complex cross-clapping mode, and c) the unpredictable non-linear chaotic pattern observed in time. d) Diagram containing the classification of the dynamic modes of the magnetic membrane actuator at various frequencies and magnetic fields illustrating the prevalence of chaotic regions above 10 Hz and 2 mT impulses.

Our current framework for the design of machines prioritizes the generation of well-controlled programmatically actuated outputs [165]. The spirit of robotics, including soft robotics, is to assist humans to perform repetitive tasks that can be easily programmed based on given conditions [166]. Feedback systems, as those shown in the previous Sections 5.3.2 and 5.3.3, illustrate how a feedback system can be used to have predictability and well control of the actuation of soft systems to increase their reliability and efficiency. However,

the negative connotation associated with unpredictable behavior can be re-evaluated, and think about how random motion might be useful and in which scenarios.

Chaotic motion is present in many dynamic systems with an increasing number of degrees of freedom [167]. A double pendulum system generates motion regimes with chaotic characteristics (Figure 5.14a,b) [168]. Random and unpredictable motion is also present in the motion characteristics of living organisms. E.g. a possible prey might be more successful in escaping from a hunter if it follows a non-deterministic unpredictable path during the chasing [169]. Our interactions strongly depend on the initial conditions of our surroundings. For example, the human blinking period is not strictly set. Despite we need to blink at least every 20 s to keep our eyes hydrated, other parameters condition the trigger of the blinking reflex creating a difficult-to-predict blinking pattern [170]. A proper equilibrium between structured, unpredictable, and creative events is even beneficial to our mental health [171]. Collaborative soft machines integrating magnetic soft actuators with tunable dynamic modes might be interesting to create both, controlled and random unpredictable motion [102, 172]. Here, I will focus on showing how the chaotic regime of the robots might have useful applications.

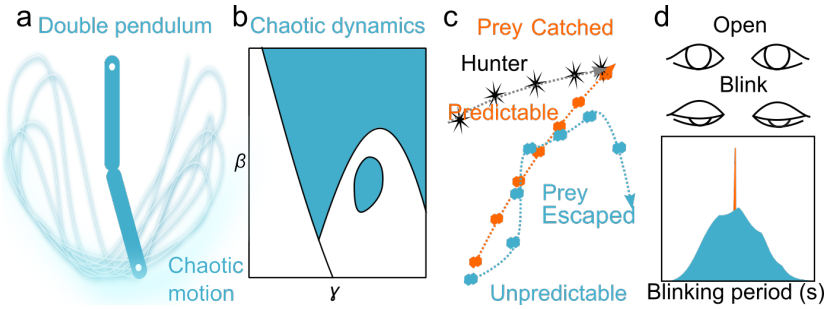

Figure 5.14: Non-linear behavior in common examples. a) A double pendulum containing 2 DOF is a prototypical example, that chaotic motion can arise easily with the number of degrees of freedom in a system. b) While there are certain conditions where linear dynamics are observed, the chaotic dynamics regions of a double pendulum for specified initial conditions can be very broad. c) Unpredictable behavior in living organisms is useful in survival-like conditions, where the chances to escape increase by moving through an unpredictable path. d) Our own triggers for motion are influenced by subtle and unexpected changes in the environment. Our blinking rate is not fixed, it can have a relatively broad distribution depending on the internal and environmental tasks performed.

Figure 5.15 shows a biomimetic application that imitates the trigger of the human blinking rate by using the random actuation of the soft actuator. In this case, the actuator acts as an optomechanical chopper that blocks the light path of a laser aligned with a photodetector. The body of the robot absorbs the laser light giving the possibility to control the intensity of the signal detected by the photodiode when the laser is blocked during actuation. Non-deterministic signal pulses were generated as a result of the random blocking of the light path by a soft actuator driven at 5 mT, 59.1 Hz (Figure 5.15b). With a simple data averaging

and threshold level (0.91) classification, it was possible to create a semi-random stream of high and low signals (Figure 5.15c).

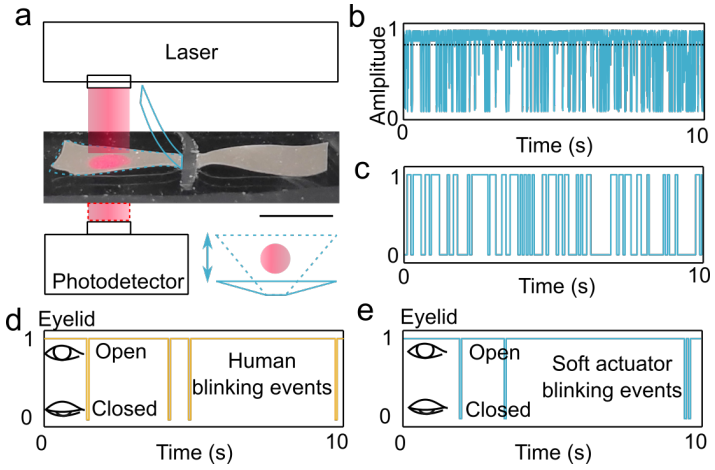

Figure 5.15: Optomechanical approach to generate random signals with magnetic soft actuators. a) A laser module is aligned towards a photodetector window. A magnetic soft actuator is placed in the path of the laser to act as an optomechanical chopper that temporarily blocks the laser path during its motion. If the arm blocks the light, the voltage of the photodetector drops down; otherwise light can reach the photodetector, creating a high voltage level. b) The normalized amplitude of the signal modulated by the chaotic motion of a robot running in a chaotic regime (59.1 Hz, 5 mT). c) Binarized signal after applying a moving average and defining a threshold level of 0.91. This approach can be used to d) imitate the human blinking non-deterministic pattern, e) by appropriately selecting the threshold level during the binarization process, the signal can trigger a fictional blinking event that probabilistically will have a similar blinking rate that humans but also their non-predictable pattern.

This type of binarized signal might be useful to create a mimicking of human blinking events (Figure 5.15d). Assigning "low" signal levels as closed eyelids and "high" levels as open eyelids we register the events of a human blinking. Depending on the assigned threshold level to change the classification of a signal, it is possible to change the relative frequency of events that trigger "low" signal levels. Assigning a threshold of 0.02, the signal showed 4 blinking events randomly spaced over a period of 10 s. In contrast to a deterministic machine that would use in the simplest case a fixed blinking period of 2.5 s to the more complex algorithms that might use a pseudorandom number sequence, our system is already capable of mechanically accounting for the non-deterministic behavior that is more similar to the human behavior.

As a second example, here is explained the use of unpredictable motion for useful modulations. We may notice that an audio recording can be duplicated many times, but a live performance by an artist will be distinct and unique each time. In a similar way, a robot modulating the transmission of voice audio signal can change the perception of the sound by adding randomly placed volume, tone, or pace modulations (Figure 5.16a-c). Using the setup described in Figure 5.15a optically transmitting a computer-generated audio file repeating

nine times the message "Hello world!", we showed the random modulation of the message creating nine different versions of the same message (Figure 5.16d). This example illustrates the potential for incorporating non-deterministic motion to create socially appealing and distinct experiences for soft robots interacting with humans.

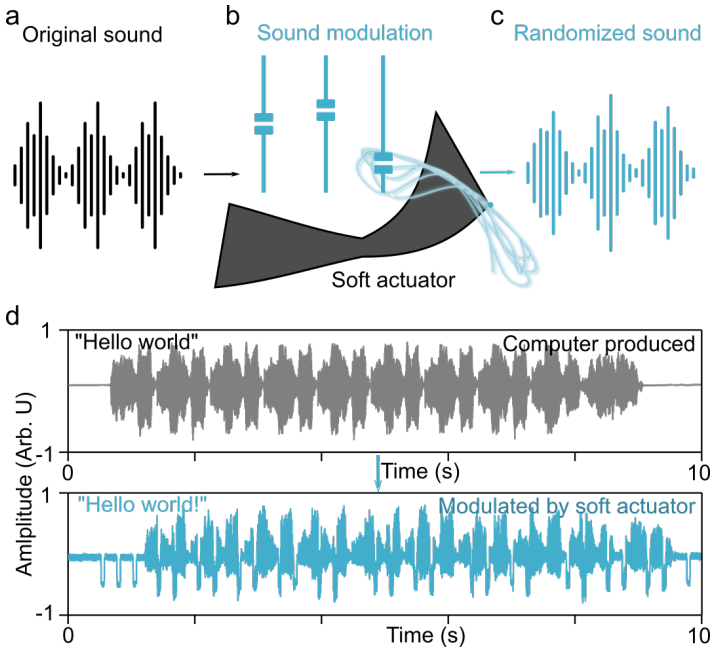

Figure 5.16: Random sound modulation using the chaotic motion of magnetic soft actuators. a) An audio file produced by a digital voice generator and transmitted through the laser module described in Figure 5.15, b) can be modulated using the soft actuator c) to create a randomized version of the message by changing the volume, pitch, or tone. d) A graph containing the as-produced signal saying "Hello world" 10 times is displayed (top), the amplitude of the signal, is changed during the motion of the soft actuator in a chaotic regime generating 9 different versions of the same message that slightly differ from each other.

6 Unconventional formats for magnetic field sensors

Magnetoelectronic systems are present in the most advanced technology trends, from smartphones and electromobility to robotics [173, 174]. Novel micromagnetic phenomena are already pushing the possibilities of devices proposing spinorbitronic, magnetic tunnel, or domain walls for sensors, logic, memories, and power devices [175–177]. But novel form factors outside silicon are still rarely addressed. New formats of magnetoelectronic devices and sensors, in particular, might open several implementation possibilities outside the printed circuit board (PCB). Here, I will shortly discuss how magnetic field sensors with unconventional material properties might offer new implementation possibilities.

The findings presented in Section 6.1, 6.2, and 6.3 are published in the following article [178] and are under preparation for publication, respectively. The results highlighted in this manuscript summarize the capabilities of novel form factors for magnetic field sensors. The contribution to the development of self-healable and transparent sensors from Dr. R. Xu and F. Cheng is greatly appreciated. I would also like to acknowledge the fabrication of 3D-printed metallic structures carried by Dr. Anna Martin Vilardell and Dr. L. Stepien.

6.1 Printed magnetic field sensors with self-healing properties

In Chapters 4 and 5, is discussed how magnetic field sensors implemented in flexible and even stretchable formats have been shown as useful interfaces and feedback systems. I also showed that these systems can be reliably measured even during prolonged and

active deformations using the appropriate readout mechanisms. However, it is expected that continuous use may damage them in the long term and might create failures of the sensors and the need for substitution. Especially for systems used on a day-to-day basis, the possibilities of sensor damage might increase rapidly. For the sustainable and cost-effective implementation of magnetic field sensors that may suffer from quick wear a solution is needed that diminishes the substitution rate of the sensor systems.

Here, it is shown the use of a self-healing polymer sensing composite to enable easy repair of printed sensors that have cracks at the μm-scale (6.1a) or have been even torn apart (Figure 6.1b). The composite consists of Py microparticles embedded in a PBS/PDMS self-healable matrix (Section 3.1.8) [179]. The smart combination of the self-healing capabilities of the matrix combined with the magnetic interaction of polymers creates the possibility to have a magnetically induced repairing mechanism. As printed sensors were conducive and had a MR response of 0.9% owing to the AMR effect of the Py fillers. After inducing a μm-scale crack, the sensor fails and a high resistance level is observed. Using an AMF (<130 mT, 50 Hz) induces the temporary alignment, attraction, and further oscillation of the particles that reestablish the percolation of the conductive network of MR fillers in the polymer. The repaired sensor still shows the expected MR response that is increased from 0.9% to 1% (Figure 6.1c) with a high sensitivity of 35.7 Ω T^{-1}, low noise 19 Ω $Hz^{-1/2}$ at 1.8 Hz, and high resolution of ρ_{max} = 36 nT (Equation 3.6). The AMF-mediated healing can be used by command after several repetitions of the device failure (Figure 6.1d) and recover (even enhancing) the sensing capabilities of the as-printed sensors.

This demonstrated non-manual remote repairing with AMF of the sensors with 100% performance recovery at ambient conditions without heat treatments. Beyond the fact that printed magnetic field sensors were taken to the nT detection levels for the first time, the increase in reliability places this technology as an attractive approach to take flexible magnetic field sensors closer to day-to-day use viability. Additionally, we were able to validate the technology's ability to sense and heal even in environmentally tough conditions like underwater exposure, relevant for sensors on textiles and flexible substrates. Self-healing, as an unconventional feature for magnetic field sensors, provided the possibility to create more sensitive, and more reliable printed systems.

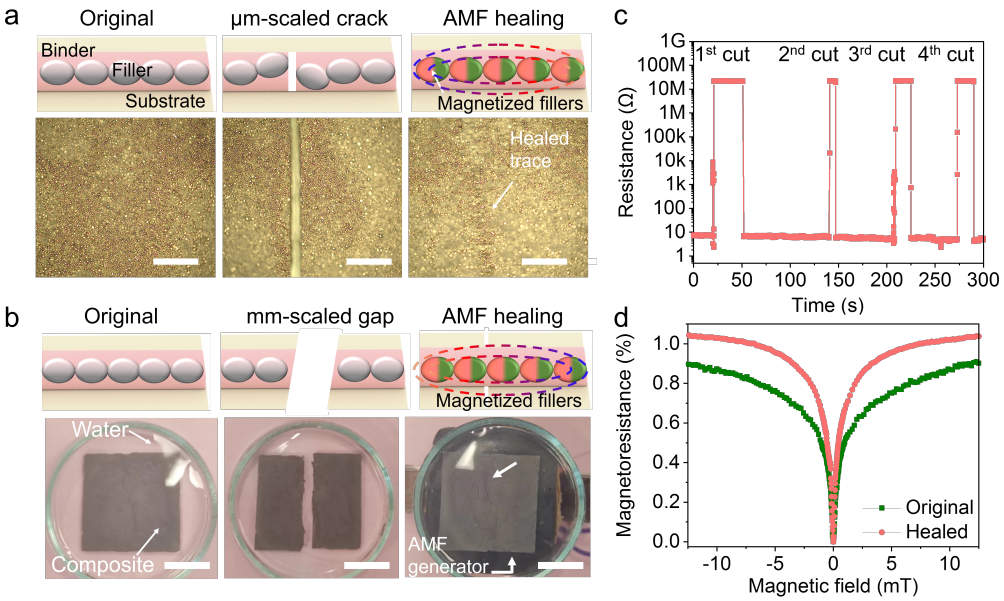

Figure 6.1: Self-healable magnetic field sensors. Py fillers inside of a self-healable matrix based on PBS and PDMS were prepared. a) Sensors with micrometer scale cracks can be repaired by using AMF. b) This mechanism can be extended to samples separated by some millimeters, where the magnetic fillers drive the full motion of each of the sections when the AMF is applied. c) Resistance of sensors that were repeatedly cut with a scalpel and healed by the AMF. d) Magnetoresistance characteristics of the sample show even an increase in the sensing performance compared to the as-prepared sensors before repairing (Adapted from [178], used under CC BY 4.0).

6.2 Transparent magnetic field sensors

Mechanically imperceptible electronics enable seamless integration into flexible formats [97]. In a similar way, visually imperceptible sensors allow for integration without affecting the object's appearance. As systems move toward multifunctional materials with visual feedback, transparency becomes even more critical. Using nano-sized fillers with a high aspect ratio is a possible strategy to achieve optically transparent conductive composites [180].

Using electrochemically grown Py nanowires via AAO templates, it was possible to dispense transparent magnetic field sensors that showed 1.2% and 3.4% of magnetoresistance change in the parallel and perpendicular direction, respectively (Figure 6.2a). The sensors can be prepared to achieve transmission levels up to 85% making it possible to print sensors into transparent substrates like glass (Figure 6.2b). Similar to the capacitive touchscreens that allow interaction with our flat screens, magnetic interfaces might be suited to interact with holographic-like interfaces that show objects in the 3D space. Benefiting from the magnetic and visual transparency of a sensor printed into a glass substrate, we create a Pepper's ghost optical effect for interactive holographic-like visuals [181]. Figure 6.2c contains a sequence of an animation of a cat running where the magnification of the visualization is controlled

by the proximity of a permanent magnet. Using a similar strategy but printing the sensors into a truncated pyramid PET structure, allows for observing the animation from different angles as if placed in three-dimensional space (Figure 6.2d). The rotation of the object was controlled through the interaction between the visually imperceptible integrated sensor and the permanent magnet.

Interaction through magnetic fields in three-dimensional visuals might find interesting applications for education, design, gaming, and promotional systems. Our touchscreen displays rely on transparent conductors for intuitive interaction with objects on a flat screen. In the same way, transparent magnetic interfaces could boost the development of touchless visuals. Holographic interfaces can create more realistic digital experiences and the low interference of magnetic fields with such visuals can enable higher integration capabilities. The unconventional feature of visual transparency in magnetic field sensors opens up possibilities for creating more realistic digital experiences, which are possible through their visual imperceptibility.

6.3 3D printed magnetic field sensors

We are currently repurposing the concept of printing. Nowadays we print more than books. Now we are printing batteries, circuits, displays, and magnets [182–187]. We are printing tools, prothesis, organs, and food [188–191]. From 2D to 3D objects, the additive manufacturing of objects opens exciting possibilities that fit perfectly in any science fiction book. 3D printed formats already profit from the functionality embedded in the shape of the printed part [192]. Embedding electronic capabilities during the additive manufacturing process allows for building intelligent parts that can measure and report their state during operation [193]. Removing the need for assembly operations might provide access to print-and-play intelligent systems.

Here, I show our current developments of 3D printed magnetic field sensors that profit from the geometry, the magnetic, and the sensing capabilities of the as-printed structure. For assessing magnetic fields on a 3D printed object, we employed the skin effect that is dominant in the change of impedance of a sample conducting AC. The effect is known to be larger in materials with larger magnetic susceptibility, so we employed Invar 36 (Ni36/Fe64 alloy) known for its high mechanical stability after printing. By printing the alloy using powder

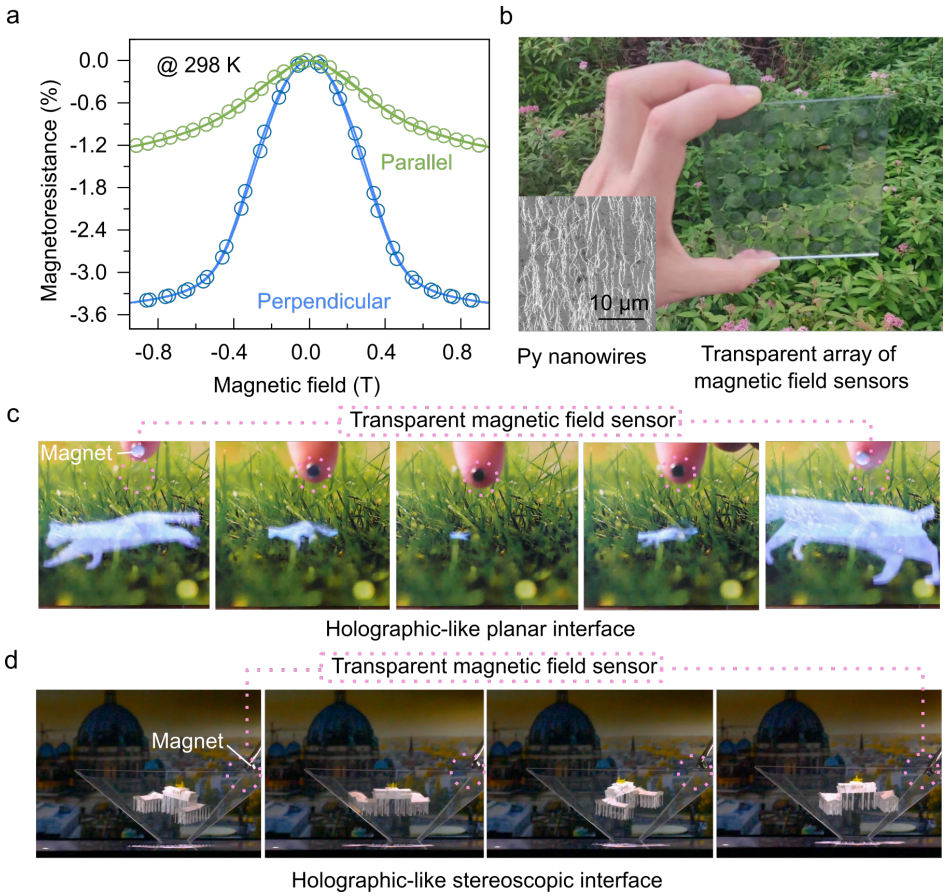

Figure 6.2: Transparent magnetic field sensors. a) Magnetoresistance response of transparent magnetic field sensors based on Py nanowires. b) The nanowires are aligned (inset) to achieve good percolation networks that are conductive and optically transparent sensors that can be used for transparent touchless interfaces. The transparent magnetic field sensors are demonstrated to interact with holographic-like interfaces that respond to the proximity of a permanent magnet. c) Contains the animation of a cat running while the user changes the zoom parameters by the proximity of the magnet. d) Shows a three-dimensional projection of a building that is rotated by command of a sensor printed over the transparent projector screens.

bed laser fusion, it is possible to obtain highly dense (99.95% with respect to bulk alloy) structures with a low coefficient of thermal expansion. The impedance change with magnetic fields has been shown dependent on the dimensions of the tested 3D structure. As an example, a simple cylinder structure with different thicknesses (0.5 mm and 1 mm), will show a maximum MI effect of 50% and 120%, respectively. The characterization is done using a Hall bar structure type for further magnetotransport characterizations.

The aim of this type of structure would be embedding sensing, mechanical and geometrical capabilities in a single print. Figure 6.4 shows two examples of application scenarios of 3D printed structures of Invar 36. A spring-like structure will be able to bend upon the application of torques via magnetic fields. The bending angle of such a structure would depend on the intensity of the applied magnetic field that might be applied with an electromagnet (Figure 6.4a). While the structure is able to bend, the changes in the magnetoimpedance signal allow

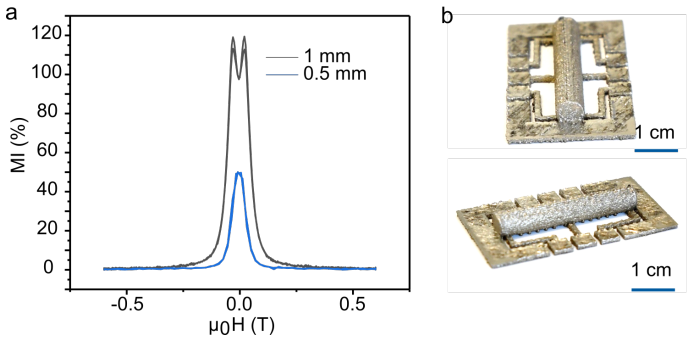

Figure 6.3: 3D printed magnetic field sensors. a) Magnetoimpedance characterization of b) 3D printed cylinders with different radii. The sensors showed changes of 120% in the impedance measured at 8000 Hz.

checking the current actuation state of the printed part (Figure 6.4b). The magnetoimpedance signal registers the 20 oscillations of the structure when moving up and down. By integrating a laser module into such a structure, it is demonstrated a 3D-printed electromagnetic sweeper that can report its own actuation state (Figure 6.4c). These intelligent parts can be designed already as functional devices that can scan barcodes automatically and can work as a prototype of a laser lithography sweeper or a micromanipulator for alignment in an optical table. A smart combination of the magnetostatic interactions, the appropriate geometry, and the sensing capabilities could lead to smarter 3D-printed objects.

In a second application scenario, one could think of day-to-day users that design interactive devices and games. Creating a curved structure is a design strategy to create a gradient of magnetostatic interactions (Figure 6.4d). If there is a fixed plane on top that separates the magnetic printed object from a permanent magnet, the interactions will be stronger closer to the tip of the curved structure. In that way, it is possible to use these magnetostatic interactions and the differential intensity of the magnetic field due to the position of a permanent magnet. Figure 6.4e shows the signal of magnetically attached spherical magnets moving toward the area of maximum interaction. A high-level signal is observed when the magnet approaches and gets fixed to the top of the curved area. By embedding this structure in customized 3D-printed parts is possible to create fine motricity tools and interactive games that benefit from the feedback from permanent magnets and that can measure the events that are happening during the user activity. These examples demonstrate the possibility of combining the magnetostatic interactions, the appropriate geometry, and the sensing capabilities for smarter 3D-printed magnetosensitive objects.

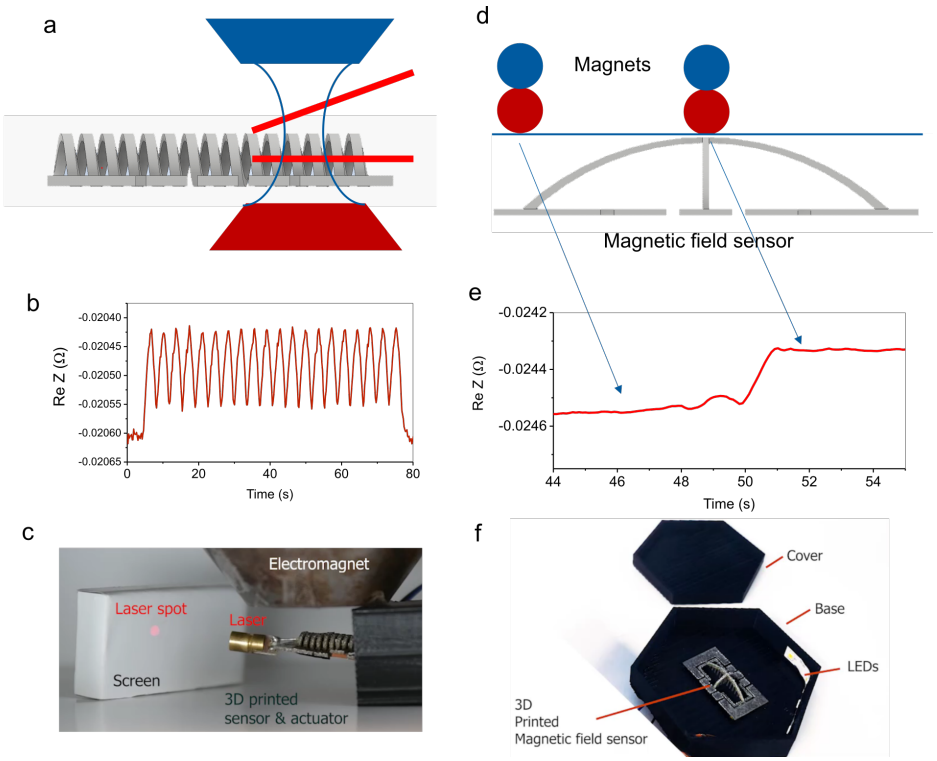

Figure 6.4: Demonstrative applications of 3D printed sensors. a) A 3D-printed Invar 36 spring can be deformed using magnetic fields produced by electromagnetic coils. b) The object can be connected to assess its own actuation state from the measurement of the applied magnetic field employed for deformation. Benefiting from the deformable geometry, their interaction with magnetic fields, and sensing capabilities, the printed structure can work as an electromagnetic sweeper. c) Shows the integration with a laser module that changes and registers the target position of the laser spot. d)Second example showing a 3D printed fine motricity game. The sensing structure contains an arc geometry that effectively changes the distance with respect to a magnet that is in a plane above the 3D-printed sensor. e) The sensing structure is able to determine the proximity of the permanent magnet to the center of the arc by revising the signal level. f) A photograph showing the sensor embedded in a 3D printed case that completes the interface for easy manipulation of the user with the object.

7 Conclusion and Further Work

Along this work, I have addressed some of the recurrent challenges shown by systems constituted by magnetoresponsive composites. For printed sensors, these were related to the narrow dynamic range, susceptibility to damage, and involved fabrication of their magnetosensitive fillers. The developments shown have demonstrated the extension of detectable fields in at least three orders of magnitude, demonstrated the possibility of fabricating magnetoresistive inks based on broadly available Bi materials, and increased the reliability of printed sensors by contributing to the development of magnetically induced healing driven by AMF. In addition, novel formats for magnetically sensitive sensors were proposed like stretchable sensors compatible with skin deformations, transparent sensors that are visually imperceptible and prospectively used for holographic-like interfaces, and 3D printed magnetic field sensors that profit from the shape, the magnetic interactions and their sensing capabilities with aiming for fully additive manufacturing of intelligent systems.

I also addressed one of the most recurrent challenges in flexible electronics, which is related to the instability of the signal during the deformation of the sensor. In this manuscript, a method to obtain a strong strain contribution decoupling in AHE sensors was demonstrated. Using the switching current ZOH strategy, it was possible to reliably measure magnetic fields with sensors that are placed into mechanically active surfaces like human skin or soft actuators. Similarly, a method to reliably measure MR sensors in strain conditions was developed during the doctoral research and submitted for a patent application [143]. These developments might have direct contributions to the widespread implementation of flexible magnetic field sensors in day-to-day applications.

Here, it was also shown the implementation of highly integrated magnetic soft actuators able to track their orientation in space, register their assembly sequences, and feedback control of their lifting actuation. This was possible through the smart combination of ultrathin magnetic field sensors with magnetic composites dedicated to tetherless magnetic actuation. I expect that the proposal of novel soft mechatronic systems actuated via magnetic fields might expand the possible application scenarios of highly conformable flexible and stretchable magnetic field sensors, similar to the case of rigid sensors being implemented thoroughly in current mechatronic systems.

7.1 Outlook

Although the responses to magnetic fields were emphasized in this manuscript, it is important to know that composites based on magnetosensitive particles have a richer set of interactions that can be used for multifunctional sensors. Apart from the studied magnetotransport and magnetic actuation effects, other effects like photoabsorption, thermal, induction, piezoelectric, or multiferroic, effects can be used to measure a wide variety of physical parameters. Even measuring day-to-day physical variable parameters like temperature, is still not fully developed as printed sensors. Absolute and differential temperature measurements are ubiquitous for the operation and conditioning of electronic systems, such and other types of sensors are still in progress to be validated in different conditions. With a more comprehensive set of printable electronic materials, the vision of a CMYK-model-like printer for electronics might eventually become possible. Letting my conjectures go rather far beyond that what has been proven [194], a *universal sensing ink* where several environmental physical parameters can be easily extracted might start to sound possible with the continuous development of multifunctional electronic printable materials.

The commercialization of magnetically sensitive functional inks and pastes is slowly becoming a reality. With the first requests of samples and pastes to the Innovation Lab "Flexisens", and the establishment of the initial cooperations with industrial partners interested in developing and applying printed magnetic fields and other sensors; it is becoming clear that there is a current need that is potentially larger in the future for alternative fabrication methods for electronics. Characteristics like self-healing, transparent, biodegradable, and biocompatible in multifunctional composites and pastes will become increasingly important towards concepts of sustainability, waste reduction, and circular economy. Alternative substrates like paper,

wood, and other biomaterials will also need to be suited to integrate with these types of technologies in order to create commercial products that are environmentally friendly and still fully functional devices.

On the other hand, magnetic soft robotics might take longer to develop but their effects could be potentially more disruptive. Living organisms are in practice transparent to magnetic fields, and cases like safe and programmable low-invasive interventions might be recurrent through magnetically controlled soft systems. These can be placed from the inside to the outside of the body to work as auxiliary mechanisms in motor tasks. By integrating sensitive electronic skins into soft robots, as those shown in this work, the development of automatized soft machines gets closer. The next big challenge is to integrate flexible control or processing units that will close the complete feedback loop inside the robotic system. The power of actuation in magnetic robots is typically delegated to external magnets and coils, the electronics and control might use the motion or induction power to feed the electronic units to have full autonomy of the system. While the individual components are already there, a full implementation is still to be demonstrated of *fully flexible* untethered actuation and wireless control of magnetic soft robots.

Magnetic actuation permits fast actuation where non-linearities of soft actuators become more evident. Magnetic actuators across several scales can be fabricated and analyzed in different ambient, vacuum, humidity, and temperature conditions. Such possibilities are highly attractive for testing a variety of multi-physics models that will help us to understand the dependence of such variables in these versatile models. Similar to the examples shown here, where chaotic motion was beneficial to perform complex tasks like biomimicking and unique media generation patterns; chaotic motion might be evaluated for cryptography, efficient random walk exploration, and propulsion through complex terrains of soft machines. It is expected that such demonstrations will slowly but firmly validate the advantages of soft actuators when uncertainty levels are high. A system with fully embodied intelligence would be able to improvise motion patterns to avoid obstacles, communicate, and even respond in socially demanding conditions.

I expect that the advancements presented in this work serve as an example of showing that magnetically actuated flexible devices have great potential to develop in niche applications in the short term and also have a possible widespread future in the medium term and days ahead. We should expect a step-by-step implementation of these technologies in auxiliary devices before they represent the core of future technologies. The demonstrated examples

showing peripheral interfaces might be a good starting point for such implementations. Integrating thin and flexible magnetic field sensors into common objects can transform virtually any surface into a magnetic interface. By creating discrete sensors distributed in target spaces, several tasks at home or at office spaces can be automatized. Given the flexibility in implementation, the characteristics of the presented sensors fit very well in concepts of user innovation, where users themselves apply this technology in a case-by-case scenario [195]. For this vision, an appropriate framework for data acquisition and software design has to be developed and standardized for the users to be able to develop solutions by themselves based on these technologies. Such type of pathway is inspired by the roadmap of previous technologies like 3D printing [196]. I expect that these validations motivate scientists, industrial partners, and people, in general, to decrease the barrier to entry into this technology space, and enable the mix and match of magnetically responsive platforms with other functional materials.

Bibliography

1. Henshilwood, C. S. *et al.* A 100,000-year-old ochre-processing workshop at Blombos Cave, South Africa. *Science* **334,** 219–222 (Oct. 2011).
2. Ocko, S. A. *et al.* Solar-powered ventilation of African termite mounds. *Journal of Experimental Biology* **220,** 3260–3269 (Sept. 2017).
3. Onuaguluchi, O., Panesar, D. K. & Sain, M. Properties of nanofibre reinforced cement composites. *Construction and Building Materials* **63,** 119–124 (July 2014).
4. Choi, S., Han, S. I., Kim, D., Hyeon, T. & Kim, D.-H. High-performance stretchable conductive nanocomposites: materials, processes, and device applications. *Chemical Society Reviews* **48,** 1566–1595 (Mar. 2019).
5. Mahmood, J. *et al.* Organic Ferromagnetism: Trapping Spins in the Glassy State of an Organic Network Structure. *Chem* **4,** 2357–2369. issn: 2451-9294 (Oct. 2018).
6. Miller, J. S. Organic Magnets - A History. *Advanced Materials* **14,** 1105–1110 (2002).
7. Mahmood, J. & Baek, J. B. Room-Temperature Organic Ferromagnetism. *Chem* **5,** 1012–1014 (May 2019).
8. Mendes-Felipe, C., Garcia, A., Salazar, D., Vilas-Vilela, J. L. & Lanceros-Mendez, S. Photocurable magnetic materials with tailored functional properties. *Composites Part C: Open Access* **5,** 100143 (July 2021).
9. Ha, M. *et al.* Printable and Stretchable Giant Magnetoresistive Sensors for Highly Compliant and Skin-Conformal Electronics. *Advanced Materials* **33,** 2005521 (Mar. 2021).

10. Ha, M. *et al.* Reconfigurable Magnetic Origami Actuators with On-Board Sensing for Guided Assembly. *Advanced Materials* **33,** 2008751. https://doi.org/10.1002/adma.202008751 (2021).

11. Almansouri, A. S. *et al.* An Imperceptible Magnetic Skin. *Advanced Materials Technologies* **4,** 1900493 (Oct. 2019).

12. Zhou, Y. *et al.* Giant magnetoelastic effect in soft systems for bioelectronics. *Nature Materials* **20,** 1670–1676 (2021).

13. Yang, X. *et al.* An agglutinate magnetic spray transforms inanimate objects into millirobots for biomedical applications. *Science robotics* **5,** eabc8191 (2020).

14. Wu, S., Hu, W., Ze, Q., Sitti, M. & Zhao, R. Multifunctional magnetic soft composites: a review. *Multifunctional Materials* **3,** 042003 (Dec. 2020).

15. Zhao, X. *et al.* Soft fibers with magnetoelasticity for wearable electronics. *Nature Communications 2021 12:1* **12,** 1–11. issn: 2041-1723. https://www.nature.com/articles/s41467-021-27066-1 (Nov. 2021).

16. Karnaushenko, D. *et al.* High-Performance Magnetic Sensorics for Printable and Flexible Electronics. *Advanced Materials* **27,** 880–885 (Feb. 2015).

17. Cañón Bermúdez, G. S. & Makarov, D. Magnetosensitive E-Skins for Interactive Devices. *Advanced Functional Materials* **31,** 2007788 (Sept. 2021).

18. Chung, H.-J., Parsons, A. M. & Zheng, L. Magnetically Controlled Soft Robotics Utilizing Elastomers and Gels in Actuation: A Review. *Advanced Intelligent Systems* **3,** 2000186 (Mar. 2021).

19. Dugdale, J. S. *The Electrical Properties of Metals and Alloys* (Courier Dover Publications, 2016).

20. Mott, N. F. The Mechanical Properties of Metals. *Proceedings of the Physical Society. Section B* **64,** 729–741 (Sept. 1951).

21. Ciwen, H., Jinsheng, Z. & Jianyong, L. Ultra-long wire reciprocated-WEDM with dual tensile reels winded. *Procedia CIRP* **68,** 115–119 (2018).

22. Xu, S. *et al.* Non-Hookean large elastic deformation in bulk crystalline metals. *Nature Communications* **13,** 5307. issn: 2041-1723. https://www.nature.com/articles/s41467-022-32930-9 (Sept. 2022).

23. Kim, D. C., Shim, H. J., Lee, W., Koo, J. H. & Kim, D.-H. Material-Based Approaches for the Fabrication of Stretchable Electronics. *Advanced Materials* **32,** 1902743 (Apr. 2020).

24. Luo, Y. *et al.* Technology Roadmap for Flexible Sensors. *ACS Nano* **13,** 44 (Mar. 2023).

25. Gao, W., Ota, H., Kiriya, D., Takei, K. & Javey, A. Flexible Electronics toward Wearable Sensing. *Accounts of Chemical Research* **52,** 523–533 (Mar. 2019).

26. Wu, W. Stretchable electronics: functional materials, fabrication strategies and applications. *Science and Technology of Advanced Materials* **20,** 187–224 (Dec. 2019).

27. Wu, W. & Wang, Z. L. Piezotronics and piezo-phototronics for adaptive electronics and optoelectronics. *Nature Reviews Materials 2016 1:7* **1,** 1–17. issn: 2058-8437. https://www.nature.com/articles/natrevmats201631 (May 2016).

28. Wang, L. *et al.* Flexoelectronics of centrosymmetric semiconductors. *Nature Nanotechnology 2020 15:8* **15,** 661–667 (June 2020).

29. Melchert, D. S. *et al.* Flexible conductive composites with programmed electrical anisotropy using acoustophoresis. *Advanced Materials Technologies* **4,** 1900586 (2019).

30. Lim, J. A. *et al.* Inkjet-printed single-droplet organic transistors based on semiconductor nanowires embedded in insulating polymers. *Advanced Functional Materials* **20,** 3292–3297 (2010).

31. Wang, X., Li, J., Song, H., Huang, H. & Gou, J. Highly stretchable and wearable strain sensor based on printable carbon nanotube layers/polydimethylsiloxane composites with adjustable sensitivity. *ACS applied materials & interfaces* **10,** 7371–7380 (2018).

32. Cho, S. *et al.* Fully elastic conductive films from viscoelastic composites. *ACS applied materials & interfaces* **9,** 44096–44105 (2017).

33. Namsheer, K. & Rout, C. S. Conducting polymers: a comprehensive review on recent advances in synthesis, properties and applications. *RSC Advances* **11,** 5659–5697 (Feb. 2021).

34. Koo, M. *et al.* Bendable inorganic thin-film battery for fully flexible electronic systems. *Nano letters* **12,** 4810–4816 (2012).

35. Dickey, M. D. Stretchable and soft electronics using liquid metals. *Advanced materials* **29,** 1606425 (2017).

36. Ouyang, J. Application of intrinsically conducting polymers in flexible electronics. *SmartMat* **2,** 263–285 (2021).

37. Lee, C.-J. *et al.* Crack-induced Ag nanowire networks for transparent, stretchable, and highly sensitive strain sensors. *Scientific Reports* **7,** 7959 (2017).

38. Che, Q. *et al.* Ag nanowire-based stretchable electrodes and wearable sensor arrays. *ACS Applied Nano Materials* **4,** 12726–12736 (2021).

39. Huang, S., Liu, Y., Guo, C. F. & Ren, Z. A highly stretchable and fatigue-free transparent electrode based on an in-plane buckled Au nanotrough network. *Advanced Electronic Materials* **3,** 1600534 (2017).

40. Li, H. *et al.* A self-powered porous ZnS/PVDF-HFP mechanoluminescent composite film that converts human movement into eye-readable light. *Nanoscale* **10,** 5489–5495 (2018).

41. Zhang, T. *et al.* Continuous carbon nanotube composite fibers for flexible aqueous lithium-ion batteries. *Sustainable Materials and Technologies* **20,** e00096 (2019).

42. Liu, K. *et al.* A self-supported graphene/carbon nanotube hollow fiber for integrated energy conversion and storage. *Nano-micro letters* **12,** 1–11 (2020).

43. Lee, J. *et al.* Ultrasensitive strain sensor based on separation of overlapped carbon nanotubes. *Small* **15,** 1805120 (2019).

44. Minev, I. R. *et al.* Electronic dura mater for long-term multimodal neural interfaces. *Science* **347,** 159–163 (2015).

45. Yang, G. *et al.* Non-invasive flexible and stretchable wearable sensors with nano-based enhancement for chronic disease care. *IEEE reviews in biomedical engineering* **12,** 34–71 (2018).

46. Roldughin, V. I. & Vysotskii, V. V. Percolation properties of metal-filled polymer films, structure and mechanisms of conductivity. *Progress in Organic Coatings* **39,** 81–100. issn: 0300-9440 (Nov. 2000).

47. Hu, Y., Wang, Q., Zhao, J., Xie, S. & Jiang, H. A novel porous media permeability model based on fractal theory and ideal particle pore-space geometry assumption. *Energies* **13,** 510 (2020).

48. Hórvölgyi, Z., Mate, M. & Zrinyi, M. On the universal growth of two-dimensional aggregates of hydrophobed glass beads formed at the (aqueous solution of electrolyte)—air interfaces. *Colloids and Surfaces A: Physicochemical and Engineering Aspects* **84,** 207–216 (1994).

49. Wang, Y. *et al.* Fractal dimensions and mixing structures of soot particles during atmospheric processing. *Environmental Science & Technology Letters* **4,** 487–493 (2017).

50. Zhang, M. Q. *et al.* Fractal approach to the critical filler volume fraction of an electrically conductive polymer composite. *Journal of materials science* **30,** 4226–4232 (1995).

51. Park, J. S., Kim, T. & Kim, W. S. Conductive cellulose composites with low percolation threshold for 3D printed electronics. *Scientific reports* **7,** 3246 (2017).

52. Chauhan, A., Asylbekov, E., Kespe, S. & Nirschl, H. Influence of carbon binder domain on the performance of lithium-ion batteries: Impact of size and fractal dimension. *Electrochemical Science Advances* **3,** e2100151 (2023).

53. Coupette, F. *et al.* Percolation of rigid fractal carbon black aggregates. *The Journal of Chemical Physics* **155,** 124902 (2021).

54. Das, N. C., Chaki, T. K. & Khastgir, D. Effect of axial stretching on electrical resistivity of short carbon fibre and carbon black filled conductive rubber composites. *Polymer International* **51,** 156–163 (2002).

55. White, S. I. *et al.* Electrical percolation behavior in silver nanowire–polystyrene composites: simulation and experiment. *Advanced Functional Materials* **20,** 2709–2716 (2010).

56. Zuo, Y.-T. & Liu, H.-J. Fractal approach to mechanical and electrical properties of graphene/sic composites. *Facta Universitatis, Series: Mechanical Engineering* **19,** 271–284 (2021).

57. Thomson, W. XIX. On the electro-dynamic qualities of metals:—Effects of magnetization on the electric conductivity of nickel and of iron. *Proceedings of the Royal Society of London,* 546–550 (1857).

58. Kapitza, P. The change of electrical conductivity strong magnetic fields. Part II.—The analysis and the interpretation of the experimental results. *Proceedings of the Royal Society of London. Series A, Containing Papers of a Mathematical and Physical Character* **123,** 342–372 (1929).

59. Yang, F. *et al.* Large magnetoresistance of electrodeposited single-crystal bismuth thin films. *Science* **284,** 1335–1337 (1999).

60. Zhao, C.-J., Ding, L., HuangFu, J.-S., Zhang, J.-Y. & Yu, G.-H. Research progress in anisotropic magnetoresistance. *Rare Metals* **32,** 213–224 (2013).

61. Ali, M. N. *et al.* Large, non-saturating magnetoresistance in WTe2. *Nature 2014 514:7521* **514,** 205–208. issn: 1476-4687. https://www.nature.com/articles/nature13763 (Sept. 2014).

62. Shekhar, C. *et al.* Extremely large magnetoresistance and ultrahigh mobility in the topological Weyl semimetal candidate NbP. *Nature Physics 2014 11:8* **11,** 645–649. issn: 1745-2481. https://www.nature.com/articles/nphys3372 (June 2015).

63. Binasch, G., Grünberg, P., Saurenbach, F. & Zinn, W. Enhanced magnetoresistance in layered magnetic structures with antiferromagnetic interlayer exchange. *Physical Review B* **39,** 4828–4830 (Mar. 1989).

64. Baibich, M. *et al.* Giant magnetoresistance of (001)Fe/(001)Cr magnetic superlattices. *Physical review letters* **61,** 2472–2475 (Nov. 1988).

65. Bakonyi, I. & Péter, L. Electrodeposited multilayer films with giant magnetoresistance (GMR): Progress and problems. *Progress in Materials Science* **55,** 107–245 (Mar. 2010).

66. Parkin, S. S. P. Giant Magnetoresistance in Magnetic Nanostructures. *Annual Review of Materials Science* **25,** 357–388 (Aug. 1995).

67. Hall, E. H. *et al.* On a new action of the magnet on electric currents. *American Journal of Mathematics* **2,** 287–292 (1879).

68. Popović, R. S. Hall-effect devices. *Sensors and Actuators* **17,** 39–53. issn: 0250-6874 (May 1989).

69. Nagaosa, N., Sinova, J., Onoda, S., MacDonald, A. H. & Ong, N. P. Anomalous hall effect. *Reviews of modern physics* **82,** 1539 (2010).

70. Meyer, J. *et al.* Giant magnetoresistance effects in gel-like matrices. *Smart Materials and Structures* **22,** 025032 (Jan. 2013).

71. Cox, B., Davis, D. & Crews, N. Creating magnetic field sensors from GMR nanowire networks. *Sensors and Actuators A: Physical* **203,** 335–340. issn: 0924-4247 (Dec. 2013).

72. Mietta, J. L., Tamborenea, P. I. & Martin Negri, R. Anisotropic magnetoresistivity in structured elastomer composites: modelling and experiments. *Soft Matter* **12,** 6430–6441 (July 2016).

73. Pereira, N. *et al.* Magnetic proximity sensor based on magnetoelectric composites and printed coils. *Materials* **13,** 1729 (2020).

74. Chlaihawi, A. A. *et al.* A screen printed and flexible piezoelectric-based AC magnetic field sensor. *Sensors and Actuators A: Physical* **268,** 1–8 (2017).

75. Karnaushenko, D., Makarov, D., Yan, C., Streubel, R. & Schmidt, O. G. Printable giant magnetoresistive devices. *Advanced Materials* **24,** 4518–4522. issn: 09359648 (Aug. 2012).

76. Mietta, J. J. *et al.* Anisotropic Magnetoresistance and Piezoresistivity in Structured Fe 3 O 4-Silver Particles in PDMS Elastomers at Room Temperature (2012).

77. Makarov, D., Karnaushenko, D. & Schmidt, O. G. Printable magnetoelectronics. https://oar.tib.eu/jspui/handle/123456789/4337 (2013).

78. Guo, J. *et al.* Magnetite-polypyrrole metacomposites: Dielectric properties and magnetoresistance behavior. *Journal of Physical Chemistry C* **117,** 10191–10202 (May 2013).

79. Ding, L. *et al.* Magnetism-Responsive Anisotropic Film with Self-Sensing and Multifunctional Shape Manipulation. *ACS Applied Materials & Interfaces,* acsami.1c01721 (Mar. 2021).

80. Gu, H. *et al.* Large negative giant magnetoresistance at room temperature and electrical transport in cobalt ferrite-polyaniline nanocomposites. *Polymer* **143,** 324–330 (2018).

81. Andò, B., Baglio, S., Crispino, R. & Marletta, V. Polymeric Transducers: An Inkjet Printed B-Field Sensor with Resistive Readout Strategy. *Sensors 2019, Vol. 19, Page 5318* **19,** 5318 (Dec. 2019).

82. Dai, W. *et al.* Flexible Magnetoelectrical Devices with Intrinsic Magnetism and Electrical Conductivity. *Advanced Electronic Materials* **5,** 1900111 (June 2019).

83. Gupta, P. *et al.* Large Scale Exchange Coupled Metallic Multilayers by Roll-to-Roll (R2R) Process for Advanced Printed Magnetoelectronics. *Advanced Materials Technologies* **7,** 2200190 (Nov. 2022).

84. Karnaushenko, D. *et al.* High-Performance Magnetic Sensorics for Printable and Flexible Electronics. *Advanced Materials* **27,** 880–885 (Feb. 2015).

85. Li, J. *et al.* AC/DC dual-mode magnetoelectric sensor with high magnetic field resolution and broad operating bandwidth. *AIP Advances* **11,** 045015 (2021).

86. Zakaria, Z. *et al.* Advancements in transmitters and sensors for biological tissue imaging in magnetic induction tomography. *Sensors* **12,** 7126–7156 (2012).

87. Abegunde, O. O., Akinlabi, E. T., Oladijo, O. P., Akinlabi, S. & Ude, A. U. Overview of thin film deposition techniques. *AIMS Materials Science* **6,** 174–199 (2019).

88. Chen, J. & Zhang, Z. A flexible anisotropic magnetoresistance sensor for magnetic field detection. *Journal of Materials Science: Materials in Electronics* **34,** 73 (2023).

89. Chen, Y. *et al.* Highly flexible anisotropic magnetoresistance sensor for wearable electronics. *Review of Scientific Instruments* **94,** 045005 (2023).

90. Su, D. *et al.* Ultra-Flexible Giant Magnetoresistance Biosensors for Lab-on-a-Needle Biosensing. *Advanced Materials Interfaces,* 2201417 (2023).

91. Li, H. *et al.* Stretchable spin valve with stable magnetic field sensitivity by ribbon-patterned periodic wrinkles. *Acs Nano* **10,** 4403–4409 (2016).

92. Guo, Q. *et al.* Strain-controlled giant magnetoresistance of a spin valve grown on a flexible substrate. *RSC advances* **6,** 88090–88095 (2016).

93. Monch, I. J. *et al.* Flexible hall sensorics for flux-based control of magnetic levitation. *IEEE Transactions on Magnetics* **51.** issn: 00189464 (Nov. 2015).

94. Granell, P. N. *et al.* Highly compliant planar Hall effect sensor with sub 200nT sensitivity. *npj Flexible Electronics 2019 3:1* **3,** 1–6. issn: 2397-4621. https://www.nature.com/articles/s41528-018-0046-9 (Feb. 2019).

95. Melzer, M., Makarov, D. & Schmidt, O. G. A review on stretchable magnetic field sensorics. *Journal of Physics D: Applied Physics* **53,** 083002 (Dec. 2019).

96. Cañón Bermúdez, G. S., Fuchs, H., Bischoff, L., Fassbender, J. & Makarov, D. Electronic-skin compasses for geomagnetic field-driven artificial magnetoreception and interactive electronics. *Nature Electronics* **1,** 589–595 (Nov. 2018).

97. Melzer, M. *et al.* Imperceptible magnetoelectronics. *Nature Communications* **6,** 1–8. issn: 20411723. www.nature.com/naturecommunications (Jan. 2015).

98. Cañón Bermúdez, G. S. *et al.* Magnetosensitive e-skins with directional perception for augmented reality. *Science Advances* **4,** eaao2623 (2018).

99. Melzer, M. *et al.* Wearable magnetic field sensors for flexible electronics. *Wiley Online Library* **27,** 1274–1280. https://onlinelibrary.wiley.com/doi/abs/10.1002/adma.201405027 (Feb. 2015).

100. Makushko, P. *et al.* Flexible magnetoreceptor with tunable intrinsic logic for on-skin touchless human-machine interfaces. *Wiley Online Library* **31.** https://onlinelibrary.wiley.com/doi/abs/10.1002/adfm.202101089 (June 2021).

101. Rus, D. & Tolley, M. T. Design, fabrication and control of soft robots. *Nature* **521,** 467–475. issn: 0028-0836. http://www.nature.com/articles/nature14543 (May 2015).

102. Breazeal, C. & Scassellati, B. Robots that imitate humans. *Trends in cognitive sciences* **6,** 481–487 (2002).

103. Barosz, P., Gołda, G. & Kampa, A. Efficiency analysis of manufacturing line with industrial robots and human operators. *Applied Sciences* **10,** 2862 (2020).

104. Oomen, T. in *Encyclopedia of Systems and Control* 267–276 (Springer, 2021).

105. Ogli, I. M. R. & Ogli, T. A. I. A Role of Mechanical Engineering in Mechatronics. *JournalNX,* 824–828 (2021).

106. He, B., Xu, F. & Zhang, P. Kinematics approach to energy efficiency for non-holonomic underactuated robotics in sustainable manufacturing. *The International Journal of Advanced Manufacturing Technology,* 1–16 (2022).

107. Xu, C., Yang, Z. & Lum, G. Z. Small-scale magnetic actuators with optimal six degrees-of-freedom. *Advanced Materials* **33,** 2100170 (2021).

108. Rychlik, M. *et al.* Calibration procedure and biomechanical validation of an universal six degree-of-freedom robotic system for hip joint testing. *Journal of Orthopaedic Surgery and Research* **18,** 164 (2023).

109. Li, M., Pal, A., Aghakhani, A., Pena-Francesch, A. & Sitti, M. Soft actuators for real-world applications. *Nature Reviews Materials* **7,** 235–249 (2022).

110. Nakajima, K., Hauser, H., Li, T. & Pfeifer, R. Information processing via physical soft body. *Scientific Reports 2015 5:1* **5,** 1–11 (May 2015).

111. McDonald, K., Rendos, A., Woodman, S., Brown, K. A. & Ranzani, T. Magnetorheological fluid-based flow control for soft robots. *Advanced Intelligent Systems* **2,** 2000139 (2020).

112. Wang, X. *et al.* Untethered and ultrafast soft-bodied robots. *Communications Materials 2020 1:1* **1,** 1–10 (Sept. 2020).

113. Hu, W., Lum, G. Z., Mastrangeli, M. & Sitti, M. Small-scale soft-bodied robot with multimodal locomotion. *Nature* **554,** 81–85. issn: 0028-0836. http://www.nature.com/articles/nature25443 (Feb. 2018).

114. Deng, H. *et al.* Laser reprogramming magnetic anisotropy in soft composites for reconfigurable 3D shaping. *Nature communications* **11,** 6325 (2020).

115. Amend, J. R., Brown, E., Rodenberg, N., Jaeger, H. M. & Lipson, H. A positive pressure universal gripper based on the jamming of granular material. *IEEE transactions on robotics* **28,** 341–350 (2012).

116. Linghu, C. *et al.* Universal SMP gripper with massive and selective capabilities for multiscaled, arbitrarily shaped objects. *Science Advances* **6,** eaay5120 (2020).

117. Liu, W. *et al.* Touchless interactive teaching of soft robots through flexible bimodal sensory interfaces. *Nature Communications* **13,** 5030 (2022).

118. Davarzani, S., Ahmadi-Pajouh, M. A. & Ghafarirad, H. Design of sensing system for experimental modeling of soft actuator applied for finger rehabilitation. *Robotica* **40,** 2091–2111 (2022).

119. Zhang, Z., Wang, X., Wang, S., Meng, D. & Liang, B. Design and modeling of a parallel-pipe-crawling pneumatic soft robot. *IEEE access* **7,** 134301–134317 (2019).

120. Yang, Y., Liu, Y. & Shen, Y. Plasmonic-Assisted Graphene Oxide Films with Enhanced Photothermal Actuation for Soft Robots. *Advanced Functional Materials* **30,** 1910172 (2020).

121. Li, W.-B., Zhang, W.-M., Zou, H.-X., Peng, Z.-K. & Meng, G. A fast rolling soft robot driven by dielectric elastomer. *IEEE/ASME Transactions on Mechatronics* **23,** 1630–1640 (2018).

122. Xu, R. *et al. Untethered Soft Robots with Bioinspired Bone-and-Flesh Constructs for Fast Deterministic Actuation* in *2019 20th International Conference on Solid-State Sensors, Actuators and Microsystems & Eurosensors XXXIII (TRANSDUCERS & EUROSENSORS XXXIII)* (IEEE, June 2019), 80–83.

123. Alapan, Y., Karacakol, A. C., Guzelhan, S. N., Isik, I. & Sitti, M. Reprogrammable shape morphing of magnetic soft machines. *Science advances* **6,** eabc6414 (2020).

124. Kim, Y. & Zhao, X. Magnetic soft materials and robots. *Chemical reviews* **122,** 5317–5364 (2022).

125. Della Santina, C. *et al.* Controlling soft robots: balancing feedback and feedforward elements. *IEEE Robotics & Automation Magazine* **24,** 75–83 (2017).

126. Oliveros-Mata, E. S. *et al.* Dispenser Printed Bismuth-Based Magnetic Field Sensors with Non-Saturating Large Magnetoresistance for Touchless Interactive Surfaces. *Advanced Materials Technologies* **7,** 2200227. https://doi.org/10.1002/admt.202200227 (2022).

127. Kosub, T., Kopte, M., Radu, F., Schmidt, O. G. & Makarov, D. All-electric access to the magnetic-field-invariant magnetization of antiferromagnets. *Physical Review Letters* **115,** 097201 (2015).

128. Polley, A., Ramaswamy, S. M. & Haroun, B. S. Residual offset in silicon Hall-effect sensor: Analytical formula, stress effects, and implications for octagonal Hall plate geometry. *IEEE Sensors Journal* **20,** 11283–11291 (2020).

129. Liu, J. A.-C., Evans, B. A. & Tracy, J. B. Photothermally reconfigurable shape memory magnetic cilia. *Advanced Materials Technologies* **5,** 2000147 (2020).

130. Li, H. *et al.* A highly stretchable strain sensor with both an ultralow detection limit and an ultrawide sensing range. *Journal of Materials Chemistry A* **9,** 1795–1802 (2021).

131. Su, P.-G. & Chang, C.-F. Fabrication and electrical and humidity-sensing properties of a flexible and stretchable textile humidity sensor. *Journal of the Taiwan Institute of Chemical Engineers* **87,** 36–43 (2018).

132. Peng, W. & Wu, H. Flexible and stretchable photonic sensors based on modulation of light transmission. *Advanced Optical Materials* **7,** 1900329 (2019).

133. Melzer, M., Kopylov, A., Makarov, D. & Schmidt, O. G. STRETCHABILITY AND SELF-HEALING OF WRINKLED GMR MULTILAYERS ON ELASTOMERIC MEMBRANES. **3,** 1340005. www.worldscientific.com (2013).

134. Oliveros Mata, E. S. *et al.* Printable anisotropic magnetoresistance sensors for highly compliant electronics. *Applied Physics A: Materials Science and Processing* **127.** https://doi.org/10.1007/s00339-021-04411-1 (Apr. 2021).

135. Karnaushenko, D., Makarov, D., Yan, C., Streubel, R. & Schmidt, O. G. Printable Giant Magnetoresistive Devices. *Advanced Materials* **24,** 4518–4522 (Aug. 2012).

136. Gallagher, A. J. *et al.* Dynamic Tensile Properties of Human Skin.

137. Choi, S. *et al.* Highly conductive, stretchable and biocompatible Ag–Au core–sheath nanowire composite for wearable and implantable bioelectronics. *Nature nanotechnology* **13,** 1048–1056 (2018).

138. You, I., Kong, M. & Jeong, U. Block copolymer elastomers for stretchable electronics. *Accounts of Chemical Research* **52,** 63–72 (2018).

139. Marmur, A., Della Volpe, C., Siboni, S., Amirfazli, A. & Drelich, J. W. Contact angles and wettability: towards common and accurate terminology. *Surface Innovations* **5,** 3–8 (2017).

140. Alghunaim, A., Kirdponpattara, S. & Newby, B.-m. Z. Techniques for determining contact angle and wettability of powders. *Powder Technology* **287,** 201–215 (2016).

141. Yin, L. *et al.* Magnetocrystalline anisotropy in permalloy revisited. *Physical review letters* **97,** 067203 (2006).

142. Organization, W. H. *et al. Static fields* (World Health Organization, 2006).

143. Zabila, Y., Makarov, D. & Oliveros-Mata, E. S. *Verfahren und Sensorsystem (Submitted)* DE 10 2023 105 724.3. 2023.

144. Wang, N. *et al.* Origin of linear magnetoresistance in polycrystalline Bi films. *Journal of Applied Physics* **127,** 025105. issn: 0021-8979. http://aip.scitation.org/doi/10.1063/1.5127570 (Jan. 2020).

145. Ramırez Muñoz, D. *et al.* Temperature compensation of Wheatstone bridge magnetoresistive sensors based on generalized impedance converter with input reference current. *Review of scientific instruments* **77,** 105102 (2006).

146. Zhang, Y. Q., Sun, N. Y., Che, W. R., Shan, R. & Zhu, Z. G. Anomalous Hall effect in epitaxial permalloy thin films. *Journal of Applied Physics* **6,** 25214. https://doi.org/10.1063/1.4942489 (2016).

147. Hwee Wong, G. D. *et al.* Strain-Mediated Spin-Orbit Torque Enhancement in Pt/Co on Flexible Substrate. *ACS Nano* **15,** 8319–8327. issn: 1936086X. https://pubs.acs.org/doi/abs/10.1021/acsnano.0c09404 (May 2021).

148. Steiner, R., Maier, C., Mayer, M., Bellekom, S. & Baltes, H. Influence of mechanical stress on the offset voltage of Hall devices operated with spinning current method. *Journal of microelectromechanical systems* **8,** 466–472 (1999).

149. Kosub, T. & Makarov, D. *Apparatus for characterizing the electrical resistance of a measurement object* US Patent 11,156,574. Oct. 2021.

150. Meloni, M. *et al.* Engineering origami: a comprehensive review of recent applications, design methods, and tools. *Advanced Science* **8,** 2000636 (2021).

151. Kidambi, N. & Wang, K. Dynamics of Kresling origami deployment. *Physical Review E* **101,** 063003 (2020).

152. Li, J., Godaba, H., Zhang, Z., Foo, C. & Zhu, J. A soft active origami robot. *Extreme Mechanics Letters* **24,** 30–37 (2018).

153. Yi, S. *et al.* High-throughput fabrication of soft magneto-origami machines. *Nature Communications* **13,** 4177 (2022).

154. Scharff, R. B. *et al. Towards behavior design of a 3D-printed soft robotic hand* in *Soft Robotics: Trends, Applications and Challenges: Proceedings of the Soft Robotics Week, April 25-30, 2016, Livorno, Italy* (2017), 23–29.

155. Matthews, P. B. The human stretch reflex and the motor cortex. *Trends in Neurosciences* **14,** 87–91 (Mar. 1991).

156. Tang, Y. *et al.* Leveraging elastic instabilities for amplified performance: Spine-inspired high-speed and high-force soft robots. *Science Advances* **6** (May 2020).

157. Gao, X. *et al.* Piezoelectric actuators and motors: materials, designs, and applications. *Advanced Materials Technologies* **5,** 1900716 (2020).

158. Wang, X. *et al.* Untethered and ultrafast soft-bodied robots. *Communications Materials* **1,** 67. issn: 2662-4443. https://www.nature.com/articles/s43246-020-00067-1 (Sept. 2020).

159. Ren, Z., Wang, T., Hu, W. & Sitti, M. *A Magnetically-Actuated Untethered Jellyfish-Inspired Soft Milliswimmer* in *Robotics: Science and Systems XV* (Robotics: Science and Systems Foundation, June 2019).

160. Kim, Y., Yuk, H., Zhao, R., Chester, S. A. & Zhao, X. Printing ferromagnetic domains for untethered fast-transforming soft materials. *Nature* **558,** 274–279. issn: 14764687 (June 2018).

161. Chen, Y. *et al.* Controlled flight of a microrobot powered by soft artificial muscles. *Nature* **575,** 324–329 (Nov. 2019).

162. Wu, Y. *et al.* Insect-scale fast moving and ultrarobust soft robot. *Science Robotics* **4** (July 2019).

163. Mao, G. *et al.* Ultrafast small-scale soft electromagnetic robots. *Nature Communications* **13,** 4456. issn: 2041-1723. https://www.nature.com/articles/s41467-022-32123-4 (Aug. 2022).

164. Han, J., Lang, J. H. & Bulovic, V. An Ultrathin Flexible Loudspeaker Based on a Piezoelectric Microdome Array. *IEEE Transactions on Industrial Electronics* **70,** 985–994 (Jan. 2023).

165. Tao, G., Chen, S. & Joshi, S. M. An adaptive actuator failure compensation controller using output feedback. *IEEE Transactions on Automatic Control* **47,** 506–511 (2002).

166. Sorokin, A., Berenson, D., Srinivasa, S. S. & Hebert, M. *People helping robots helping people: Crowdsourcing for grasping novel objects* in *2010 IEEE/RSJ International Conference on Intelligent Robots and Systems* (2010), 2117–2122.

167. Musielak, D., Musielak, Z. & Benner, J. Chaos and routes to chaos in coupled Duffing oscillators with multiple degrees of freedom. *Chaos, Solitons & Fractals* **24,** 907–922 (2005).

168. Marszal, M., Jankowski, K., Perlikowski, P. & Kapitaniak, T. Bifurcations of oscillatory and rotational solutions of double pendulum with parametric vertical excitation. *Mathematical Problems in Engineering* **2014.** issn: 15635147 (2014).

169. May, M. Aerial defense tactics of flying insects. *American scientist* **79,** 316–328 (1991).

170. Hoppe, D., Helfmann, S. & Rothkopf, C. A. Humans quickly learn to blink strategically in response to environmental task demands. *Proceedings of the National Academy of Sciences of the United States of America* **115,** 2246–2251 (Feb. 2018).

171. Zakaria, C., Balan, R. & Lee, Y. StressMon: Scalable detection of perceived stress and depression using passive sensing of changes in work routines and group interactions. *Proceedings of the ACM on Human-Computer Interaction* **3,** 1–29 (2019).

172. Shih, B. *et al.* Electronic skins and machine learning for intelligent soft robots. *Science Robotics* **5,** eaaz9239 (2020).

173. He, Q. L., Hughes, T. L., Armitage, N. P., Tokura, Y. & Wang, K. L. Topological spintronics and magnetoelectronics. *Nature materials* **21,** 15–23 (2022).

174. Krings, A. & Monissen, C. *Review and trends in electric traction motors for battery electric and hybrid vehicles* in *2020 International Conference on Electrical Machines (ICEM)* **1** (2020), 1807–1813.

175. Barla, P., Joshi, V. K. & Bhat, S. Spintronic devices: a promising alternative to CMOS devices. *Journal of Computational Electronics* **20,** 805–837 (2021).

176. Alamdar, M. *et al.* Domain wall-magnetic tunnel junction spin–orbit torque devices and circuits for in-memory computing. *Applied Physics Letters* **118,** 112401 (2021).

177. Makarov, D. *et al.* New dimension in magnetism and superconductivity: 3D and curvilinear nanoarchitectures. *Advanced Materials* **34,** 2101758 (2022).

178. Xu, R. *et al.* Self-healable printed magnetic field sensors using alternating magnetic fields. *Nature Communications* **13,** 6587. https://www.nature.com/articles/s41467-022-34235-3 (2022).

179. Tang, M. *et al.* Autonomous self-healing, self-adhesive, highly conductive composites based on a silver-filled polyborosiloxane/polydimethylsiloxane double-network elastomer. *Journal of Materials Chemistry A* **7,** 27278–27288 (2019).

180. Ding, Y., Cui, Y., Liu, X., Liu, G. & Shan, F. Welded silver nanowire networks as high-performance transparent conductive electrodes: Welding techniques and device applications. *Applied Materials Today* **20,** 100634 (2020).

181. Chehlarova, T. & Chehlarova, K. *Managing pepper's ghost illusion using intelligent methods* in *2020 IEEE 10th International Conference on Intelligent Systems (IS)* (2020), 415–420.

182. Ladd, C., So, J.-H., Muth, J. & Dickey, M. D. 3D printing of free standing liquid metal microstructures. *Advanced Materials* **25,** 5081–5085 (2013).

183. Stepien, L. *et al.* Investigation of the thermoelectric power factor of KOH-treated PEDOT: PSS dispersions for printing applications. *Energy Harvesting and Systems* **3,** 101–111 (2016).

184. Costa, C., Gonçalves, R. & Lanceros-Méndez, S. Recent advances and future challenges in printed batteries. *Energy Storage Materials* **28,** 216–234 (2020).

185. Khan, Y. *et al.* A New Frontier of Printed Electronics: Flexible Hybrid Electronics. *Advanced Materials* **32,** 1905279. issn: 0935-9648. https://onlinelibrary.wiley.com/doi/10.1002/adma.201905279 (Apr. 2020).

186. Hu, Z. *et al.* Inkjet printed uniform quantum dots as color conversion layers for full-color OLED displays. *Nanoscale* **12,** 2103–2110 (2020).

187. Chaudhary, V., Mantri, S., Ramanujan, R. & Banerjee, R. Additive manufacturing of magnetic materials. *Progress in Materials Science* **114,** 100688 (2020).

188. Moritoki, Y. *et al.* 3D-printed micro-tweezers with a compliant mechanism designed using topology optimization. *Micromachines* **12,** 579 (2021).

189. Park, G.-S., Kim, S.-K., Heo, S.-J., Koak, J.-Y. & Seo, D.-G. Effects of printing parameters on the fit of implant-supported 3D printing resin prosthetics. *Materials* **12,** 2533 (2019).

190. Rybicki, F. J. Medical 3D printing and the physician-artist. *The Lancet* **391,** 651–652 (2018).

191. Wen, Y., Chao, C., Che, Q. T., Kim, H. W. & Park, H. J. Development of plant-based meat analogs using 3D printing: Status and opportunities. *Trends in Food Science & Technology* (2022).

192. Li, S. *et al.* Additive manufacturing-driven design optimization: Building direction and structural topology. *Additive Manufacturing* **36,** 101406 (2020).

193. Lee, J., Kim, H.-C., Choi, J.-W. & Lee, I. H. A review on 3D printed smart devices for 4D printing. *International Journal of Precision Engineering and Manufacturing-Green Technology* **4,** 373–383 (2017).

194. Wheeler, J. A. & Feynman, R. P. Interaction with the absorber as the mechanism of radiation. *Reviews of Modern Physics* **17,** 157–181. issn: 00346861 (1945).

195. Von Hippel, E. *Democratizing innovation* (the MIT Press, 2006).

196. Bourell, D. L., Rosen, D. W. & Leu, M. C. The roadmap for additive manufacturing and its impact. *3D Printing and Additive Manufacturing* **1,** 6–9 (2014).

List of Figures

1.1 Ancient toolkit for processing ochre pigments 1
1.2 Functional mixtures and compounds 2
1.3 Applications of magnetic composites 3
1.4 Diagram that illustrates the studied technologies in this work 5

2.1 Solution processable deformable electronics 9
2.2 Solution processable magnetic field sensors 13
2.3 Magnetic soft actuators 18

3.1 Fabrication process of printed MR sensors 22
3.2 Dispenser printing of Bi-based LMR magnetic field sensors 23
3.3 Printing of transparent magnetic field sensors. 25
3.4 Fabrication of ultrathin flexible AHE sensors 28
3.5 Fabrication of magnetic actuators using PDMS matrix 33
3.6 Fabrication of magnetic actuators using SMP matrix 34

4.1 Size distribution of flakes obtained from thin film deposition 40
4.2 Comparison of binder interacting with MR thin films 41
4.3 Comparison of binder-flake interaction test 42
4.4 AMR response of Py thin films and printed sensors 43
4.5 Noise analysis for the estimation of the resolution of printed AMR sensors . 45
4.6 GMR response of a $(Py/Cu)_{30}$ multilayer thin film and a printed GMR sensor 46
4.7 Bending performance of printed AMR and GMR sensors 47
4.8 GMR response of printed sensors during stretching 48

4.9 Printed GMR sensor laminated on-skin employed for a touchless HMI interface 49
4.10 Sensing performance of printed LMR sensors 52
4.11 Large non-saturating magnetoresistance in bismuth printed sensors 54
4.12 Encapsulation of printed Bi sensors 55
4.13 Performance of printed LMR sensors during static bending tests 55
4.14 Performance of printed LMR sensors during cyclic bending tests 57
4.15 Thermal treatment of printed LMR sensors 58
4.16 Thermoforming of printed LMR sensors 58
4.17 Electronics design of magnetically interactive printed panels 60
4.18 Printed magnetically interactive panels for interactive posters 61
4.19 Printed magnetically interactive panels for safety applications 62

5.1 Flexible ultrathin AHE sensors 66
5.2 Performance of flexible AHE sensors 66
5.3 Offset reduction in Hall effect sensors 67
5.4 Comparison of conventional Hall and ZOH in bent samples 68
5.5 Comparison of the signal of the AHE sensor during a cyclic bending test . . 69
5.6 Mechanical stress decoupling in on-skin laminated sensors 71
5.7 AHE sensors for on-skin flexible Morse communicator 72
5.8 Photoabsorption of magnetically actuated membrane 74
5.9 Origami-like folding of SMP-based magnetic membranes 76
5.10 Flexible magnetic field sensors assessing the folding of magnetic actuators 78
5.11 Feedback-controlled magnetic lifter using flexible AHE sensors 79
5.12 Chaotic dynamics in magnetic soft actuators 81
5.13 Analysis of the dynamic modes in magnetic soft actuators 82
5.14 Non-linear behavior in common examples 83
5.15 Soft optomechanical generation of random signals with magnetic soft actuators 84
5.16 Random sound modulation using magnetic soft actuators 85

6.1 Self-healable magnetic field sensors 88
6.2 Transparent magnetic field sensors 90
6.3 3D printed magnetic field sensors 91
6.4 Demonstrative applications of 3D printed sensors 92

A.1 Research highlights 116

A Publication list

[1] Minjeong Ha, Gilbert Santiago Cañón Bermúdez, Tobias Kosub, Ingolf Mönch, Yevhen Zabila, **Eduardo Sergio Oliveros Mata**, Rico Illing, Yakun Wang, Jürgen Fassbender, Denys Makarov. Printable and Stretchable Giant Magnetoresistive Sensors for Highly Compliant and Skin-Conformal Electronics. *Advanced Materials* **33**, 2005521 (2021).

[2] Oleksii M Volkov, Florian Kronast, Claas Abert, *Eduardo Sergio Oliveros Mata*, Tobias Kosub, Pavlo Makushko, Denise Erb, Oleksandr V Pylypovskyi, Mohamad-Assaad Mawass, Denis Sheka, Shengqiang Zhou, Jürgen Fassbender, Denys Makarov. Domain-Wall Damping in Ultrathin Nanostripes with Dzyaloshinskii-Moriya Interaction. *Physical Review Applied* **15**, 034038 (2021).

[3] **Eduardo Sergio Oliveros Mata**, Gilbert Santiago Cañón Bermúdez, Minjeong Ha, Tobias Kosub, Yevhen Zabila, Jürgen Fassbender, Denys Makarov. Printable anisotropic magnetoresistance sensors for highly compliant electronics. *Applied Physics A* **127**, 1 (2021).

[4] Pavlo Makushko, **Eduardo Sergio Oliveros Mata**, Gilbert Santiago Cañón Bermúdez, Mariam Hassan, Sara Laureti, Christian Rinaldi, Federico Fagiani, Gianni Barucca, Nataliia Schmidt, Yevhen Zabila, Tobias Kosub, Rico Illing, Oleksii Volkov, Igor Vladymyrskyi, Jürgen Fassbender, Manfred Albrecht, Gaspare Varvaro, Denys Makarov. Flexible magnetoreceptor with tunable intrinsic logic for on-skin touchless human-machine interfaces. *Advanced Functional Materials* **31**, 2101089 (2021).

[5] Minjeong Ha, Gilbert Santiago Cañón Bermúdez, Jessica A-C Liu, **Eduardo Sergio Oliveros Mata**, Benjamin A Evans, Joseph B Tracy, Denys Makarov. Reconfigurable Magnetic Origami Actuators with On-Board Sensing for Guided Assembly. *Advanced Materials* **33**, 2008751 (2021).

[6] **Eduardo Sergio Oliveros-Mata**, Clemens Voigt, Gilbert Santiago Cañón Bermúdez, Yevhen Zabila, Nestor Miguel Valdez-Garduño, Marco Fritsch, Sindy Mosch, Mihails Kusnezoff, Jürgen Fassbender, Mykola Vinnichenko, Denys Makarov. Dispenser Printed Bismuth-Based Magnetic Field Sensors with Non-Saturating Large Magnetoresistance for Touchless Interactive Surfaces. *Advanced Materials Technologies* **7**, 2200227 (2022).

[7] Rui Xu, Gilbert Santiago Cañón Bermúdez, Oleksandr V Pylypovskyi, Oleksii M Volkov, **Eduardo Sergio Oliveros Mata**, Yevhen Zabila, Rico Illing, Pavlo Makushko, Pavel Milkin, Leonid Ionov, Jürgen Fassbender, Denys Makarov. Self-healable printed magnetic field sensors using alternating magnetic fields. *Nature Communications* **13**, 6587 (2022).

[8] Víctor Rubio-Giménez, Giel Arnauts, Mingchao Wang, **Eduardo Sergio Oliveros Mata**, Xing Huang, Tianshu Lan, Max L Tietze, Dmitry E Kravchenko, Jorid Smets, Nathalie Wauteraerts, Azat Khadiev, Dmitri V Novikov, Denys Makarov, Renhao Dong, Rob Ameloot. Chemical Vapor Deposition and High-Resolution Patterning of a Highly Conductive Two-Dimensional Coordination Polymer Film. *Journal of the American Chemical Society*, (2022).

[9] Diana Isabel Sandoval Bojórquez, Zeljko Janicijevic, Brenda Palestina Romero, **Eduardo Sergio Oliveros Mata**, Markus Laube, Anja Feldmann, Alexandra Kegler, Laura Drewitz, Ciarán Fowley, Jens Pietzsch, Juergen Fassbender, Torsten Tonn, Michael Bachmann, Larysa Baraban. Impedimetric Nanobiosensor for the Detection of SARS-CoV-2 Antigens and Antibodies. *ACS sensors* **8**, 576 (2023).

Figure A.1: Research highlights as cover and back-cover pages. (Adapted from [9, 10, 100, 126], used under CC BY).

B Scientific conferences

[1] Eduardo Sergio Oliveros Mata, et al. Printable Magnetoresistive Sensors for On-Skin Interactive Electronics (Talk). *MRS Spring Meeting and Exhibit*. Seattle, United States (online), 2021.

[2] Eduardo Sergio Oliveros Mata, et al. Stretchable Printed Giant Magnetoresistive Sensors for On-Skin Interactive Electronics (Talk). *MRS Fall Meeting and Exhibit*. Boston, United States (online), 2021.

[3] Eduardo Sergio Oliveros Mata, et al. Supervised folding of origami soft actuators enabled by magnetic e-skins (Talk). *MRS Fall Meeting and Exhibit*. Boston, United States (online), 2021.

[4] Eduardo Sergio Oliveros Mata, et al. Stretchable Printed Magnetic Sensors Based on Giant Magnetoresistive Microflakes for On-Skin Electronic Interfaces (Talk). *Joint MMM-Intermag Conference*. New Orleans, United States (online), 2022.

[5] Eduardo Sergio Oliveros Mata, et al. Magnetic Electronic Skins For Self-Supervised Origami Soft Actuators (Talk). *IEEE 12th International Conference Nanomaterials: Applications & Properties*. Krakow, Poland, 2022.

[6] Eduardo Sergio Oliveros Mata, et al. Printed Magnetic Field Sensors: From Wearable Devices to Interactive Surfaces (Talk). *IEEE 12th International Conference Nanomaterials: Applications & Properties*. Krakow, Poland, 2022.

[7] Eduardo Sergio Oliveros Mata, et al. Detecting Magnetic Fields with Printed Magnetoresistive Sensors on Rigid and Flexible Substrates (Talk). *67th Annual Conference on Magnetism and Magnetic Materials* Minneapolis, United States (online), 2022.

[8] Eduardo Sergio Oliveros Mata, et al. Magnetically Sensitive Electronic Skins for Supervised Folding of Origami Actuators (Talk). *67th Annual Conference on Magnetism and Magnetic Materials* Minneapolis, United States (online), 2022.

[9] Eduardo Sergio Oliveros Mata, et al. Printed magnetic field sensors based on bismuth showing large non-saturating magnetoresistance (Talk). *DPG spring conference of the Condensed Matter Section*. Dresden, Germany, 2023.

[10] Eduardo Sergio Oliveros Mata, et al. Supervised folding of magnetic origami actuators using highly compliant magnetic field sensors (Poster). *DPG spring conference of the Condensed Matter Section*. Dresden, Germany, 2023.

C Patent applications

[1] Yevhen Zabila, Denys Makarov, **Eduardo Sergio Oliveros-Mata**. Verfahren und Sensorsystem (Submitted) DE 10 2023 105 724.3. 2023

[2] Rui Xu, Denys Makarov, **Eduardo Sergio Oliveros Mata**. A method for fabricating printed magnetic field sensors based on magnetic powder (Submitted to Stabsabteilung Technologietransfer und Innovation, HZDR) EM1512. 2022